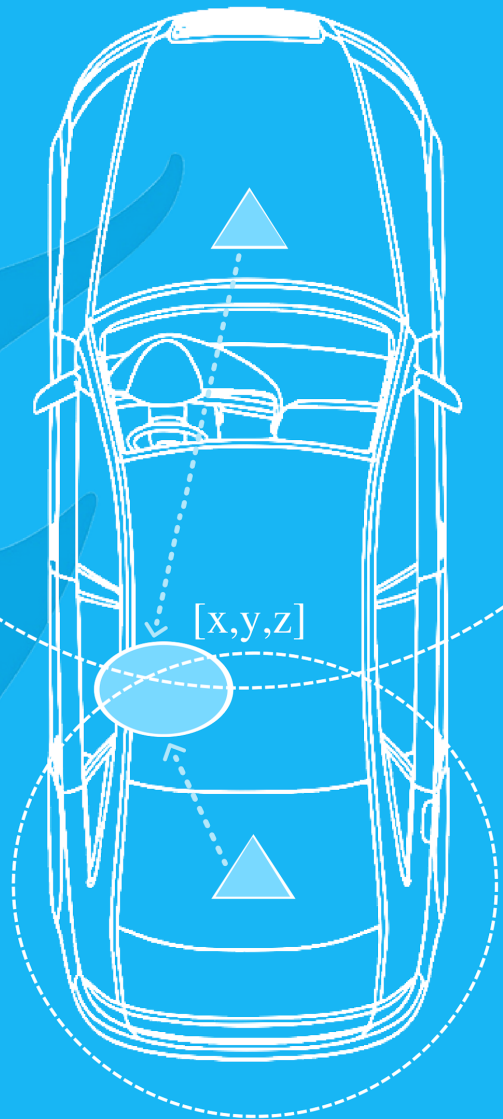


# MULTIPLE-PEOPLE DETECTION AND LOCALIZATION WITH MULTISTATIC UWB RADAR IN MULTIPATH ENVIRONMENTS FOR THE AUTOMOTIVE INDUSTRY

ELISABET RUFAS TALAMÀS





# **MASTER THESIS**

**MULTIPLE-PEOPLE DETECTION AND LOCALIZATION WITH  
MULTISTATIC UWB RADAR IN MULTIPATH ENVIRONMENTS  
FOR THE AUTOMOTIVE INDUSTRY**

by

**Elisabet RUFAS TALAMÀS**

5367891

Faculty of Electrical engineering, Mathematics and Computer Science (EEMCS),  
TU Delft, Delft, Netherlands

To be defended publicly on Monday August 29<sup>th</sup>, 2022 at 13:00

This Master Thesis has been realised under the supervision of  
TU Delft

Francesco Fioranelli

Alexander Yarovoy

NXP

Klaas Brink

Raf Roovers

by

Elisabet Rufas



# ACKNOWLEDGEMENTS

As most things in life, what you can see before you, never truly represents the full extent of things. There is a whole bigger chunk of the iceberg lying beneath the surface. And this thesis is no exception. Behind every decision, result and paragraph, there was a group of people who encouraged me and were generous enough to invest some of their time in discussions, advice and support. I would very much like to express my most sincere gratitude to all of them.

Firstly, I want to thank my daily supervisor Francesco Fioranelli. An incredibly hard-working person and a genuinely supportive supervisor. He quickly taught me how to navigate the thesis in the most efficient way. From him I have learnt some of the many qualities that a researcher should have, namely to value my work and to sharpen my critical thinking. He gave me all the tools to make it possible, and for all that, I am very grateful.

I also want to thank Professor Yarovoy. For his encouragement and for his advice. For fostering a supporting environment in MS3, where everyone is always willing to help. We have all grown as researchers under his guidance, and I am thankful for the opportunity to have nurtured from it as well.

To my daily supervisors at NXP, Klaas and Raf. Thank you for welcoming me to the NXP family. You have managed to make it easy to combine working both for NXP and for TU Delft at the same time, always providing the necessary perspective. You really did go the extra mile to ensure we could cover everything that needed to be done for this project, from lending me the equipment, the tools, and a car to investing your time and energy in helping it succeed. Your genuine interest really made all the difference.

To the rest of the NXP team, I want to thank Oswald for all his bright ideas and support in building the hardware. To Tim, who was kind and patient to walk me through his work so I could more efficiently start mine. To Stefan for his technical guidance, for never skipping a meeting and for always having useful suggestions.

And of course, I want to thank all those who held my hand during this year. Whose care and love I could feel even from the distance.

Firstly, to my parents, grandparents and family. For never, not one second, doubting me when I most doubted myself. For giving me all I ever needed and more. *Gràcies*.

To my sister. Always. To Pau, who stood by me through it all. To Marta and Dolors, who make life all that more fun. To Júlia and Noelle, for a friendship that lasts a lifetime. To Ángeles, there is no Delft without you.

To the *Pelacables*, who make me wish I could relive 4 years of telecom in UPC. To Mar and Miki, who proved *Ravenclaws* and *Hufflepuffs* are the best of matches. To the *K161* team. Ciccio, Farkas, Geo, Joel, Nic and Rosa, for being my home away from home. And to the newly funded *Breakdown club*, without whom I could never have laughed about the mess we all were towards the end. It's been fun.

I have worked and stressed over this thesis, and meanwhile, you have managed to keep me sane, and reminded me to be patient, hopeful and happy. And for that, I thank you more than anything.

I read something once, and maybe this is the place to use it:

***"If Only You Knew How Little I Really Know About The Things That Matter."  
- André Aciman***

If only you knew that 'The Things that Matter' are, most of the time, you. All of you. You are my lifeline.

*Elisabet Rufas Talamàs  
Delft, August 2022*

# ABSTRACT

In the Roadmap of 2025, EURO NCAP has announced that it will reward car manufacturers that include Child Presence Detection (CPD) technologies in their vehicles starting from 2022. Additionally, seat belt detectors are currently based on pressure sensors which can be falsely triggered with large objects placed on the seats. By basing the detection of people on human vital signs presence instead, these errors can be avoided. Therefore, in recent years, there has been an increasing need to find a solution for multiple people detection and localization in vehicles for both CPD and seat-belt reminder systems in the automotive industry.

With Ultra Wide-Band (UWB) radar, non-invasive human detection is possible through the identification of vital signs characteristics in the radar data. This work aims to improve existing literature by developing a network of UWB radars to perform multiple people detection and localization.

Specifically, an algorithm for de-centralized vital signs detection is proposed, based on the analysis of a novel model for radar signatures of vital signs. Additionally, a centralized association block is developed to fuse the detections from all radars using machine learning-based cost-matrix computation. The performance of the proposed processing pipeline is tested experimentally with a multistatic radar network. A simulation framework is developed for radar data generation to evaluate the results obtained in the experiments, and to propose variations on the evaluated radar topologies.

It can be concluded that the detection and localization of humans in the environment is possible with the proposed framework, with localization RMSE of 16cm for single and double target scenarios. The distribution of multiple focus points and the introduction of bistatic radars enhances the detection, and thus localization, w.r.t. current methods based on monostatic radars and MIMO radars.



# LIST OF FIGURES

1.1	Block diagram of methodology blocks . . . . .	10
2.1	Blocks for the proposed processing pipeline for detection and localisation of humans with multistatic UWB radar network, where the main contributions of this work are the detection and data association algorithms. The output of the detection algorithm is a detection matrix containing the range and breathing frequency of the identified humans. After the fusion of detections in the association algorithm, the output is an estimation of the position of the humans. . . . .	14
2.2	CIRs data matrix structure . . . . .	15
2.3	IQ Demodulator and Low-Pass-Filter schematic . . . . .	16
2.4	Spectrogram comparison of a measured breathing motion (left) and a simulated breathing motion (right) . . . . .	18
2.5	Phase profile of a breathing measurement to showcase the difficulty of phase-extraction. . . . .	19
2.6	Proposed detection processing pipeline schematic. An FFT is applied on the slow-time in the CIR radar data matrix. A 2D-CFAR algorithm scans the range-frequency region of interest in the range-Doppler plot and the resulting detections are clustered and interpolated to extract range and breathing frequency information. The classification block classifies the possible detections identified and discards noise. . . . .	20
2.7	Raw CIR data of a breathing measurement (left), Filtered breathing measurement (right) . . . . .	21
2.8	Range-Doppler map with clusters . . . . .	22
2.9	Range-Doppler map with clusters (zoom) . . . . .	22
2.10	Range-Doppler map with clusters (zoom). The blue dots correspond to the identified range-frequency cells in which a human being is identified, while the yellow lines mark the edges of the identified clusters, and the yellow dots are placed in the weighted average positions for both range and breathing frequency identified. . . . .	22
2.11	Classifier diagram. The evaluated range bin is passed through the processing pipeline, capable of differentiating if the identified signal corresponds to a moving human, to noise, or to a static human from which vital signs can be extracted. . . . .	23
2.12	Correlation of breathing signal (left) being correctly classified as a breathing motion, and correlation of a noise signal (right), being correctly classified as noise. . . . .	24

2.13	Visual explanation of the appearances of ghost targets. If detected ranges from the green target are associated with detected ranges from the orange target from a different radar Rx, a new false target is generated where those range-combinations cross. In this case. The red circle is a ghost target. . .	26
2.14	3D grid with a schematic representation of the various $d_c$ vectors containing the ranges to the Tx-Rx combinations. <i>Note: This particular radar setup mirrors the proposed radar-network positioning defined later in Chapter 3</i>	28
3.1	Ranger4 UWB IC: NCJ29D5 [54] . . . . .	32
3.2	Dual Board setup. The Tx and Rx boards have been separated to increase Rx sensitivity. . . . .	33
3.3	Transceiver measurement of a breathing motion (left) and distributed monostatic board measurement of the same breathing motion (right). A sensitivity improvement can be appreciated as a result of the antenna separation.	34
3.4	Monostatic and Bistatic radar setup . . . . .	34
3.5	Anchor placement in car. 2 anchors, each consisting of a transmitter, a monostatic receiver and a bistatic receiver are placed inside the car in 2 different positions. One is the rear mirror of the car, and the second is the ceiling of the back-seats. . . . .	36
3.6	Clock and trigger distribution schematic . . . . .	37
3.7	Test with boards to properly observe range offset in the Rx boards w.r.t distance $L$ . . . . .	39
3.8	Geometry of an ellipsoid . . . . .	41
3.9	Schematic of multipath reflections, considering one transmitter, one receiver, one human in the scene (depicted in gray) and one reflecting target generating multipath (depicted in blue). . . . .	43
3.10	FFT of a breathing measurement in the identified range vs FFT of a Simulation using SNR value of 5dB . . . . .	45
4.1	Positioning of boards and sphere in Anechoic Chamber of TU Delft for initial ranging test . . . . .	48
4.2	CIR radar matrices obtained in measurements of a dihedral in anechoic chamber . . . . .	49
4.3	Ranging accuracy of each of the Rx boards after correcting the ranges with factor $L$ . . . . .	49
4.4	CIR radar data obtained with the human simulation in the defined ideal environment . . . . .	51
4.5	CIR radar data obtained with the human simulation in the defined ideal environment . . . . .	51
4.6	Top left: Simulated CIR data from monostatic Rx 1. Top right: Simulated CIR data from bistatic Rx 1. Bottom-left: Simulated CIR data from monostatic Rx 2. Bottom-right: Simulated CIR data from bistatic Rx 2 . . . . .	54
4.7	Top left: Simulated CIR data from monostatic Rx 1. Top right: Simulated CIR data from bistatic Rx 1. Bottom-left: Simulated CIR data from monostatic Rx 2. Bottom-right: Simulated CIR data from bistatic Rx 2 . . . . .	54

4.8	Top left: Simulated Range-Doppler data from monostatic Rx 1. Top right: Simulated Range-Doppler data from bistatic Rx 1. Bottom-left: Simulated Range-Doppler data from monostatic Rx 2. Bottom-right: Simulated Range-Doppler data from bistatic Rx 2. The blue dots are the identified range-frequency cells which may correspond to a human being, and the yellow dots are the result of averaging the detection clusters. . . . .	55
4.9	Final position Estimation of one simulated target in an environment that recreates the experimental measurements performed in TU Delft's anechoic chamber presented in Chapter 5. . . . .	56
4.10	Range Doppler plot and detections for Rx monostatic 1 (top-left), Rx bistatic 1 (top-right), Rx monostatic 2 (bottom-left), Rx bistatic 2 (bottom-right) with $P_{fa} = 1e-5$ . . . . .	58
4.11	Localization of targets with $P_{fa} = 1e-5$ . A decrease in localization accuracy is observed, and the inability to locate the second target is noted. . . . .	59
4.12	Range Doppler plot and detections for Rx monostatic 1 (top-left), Rx bistatic 1 (top-right), Rx monostatic 2 (bottom-left), Rx bistatic 2 (bottom-right) with $P_{fa} = 1e-2$ . . . . .	59
4.13	Localization of targets with $P_{fa} = 1e-2$ . . . . .	60
5.1	Block diagram of experimental validation of the setup . . . . .	63
5.2	Schematic of board and human-occupancy placement for measurements in the anechoic chamber . . . . .	65
5.3	(Left): Tx2 , Rx monostatic 2, Rx bistatic 1 in anechoic chamber. Omnidirectional antennas facing forward. (Right): Tx1 , Rx monostatic 1, Rx bistatic 2 in anechoic chamber. Omnidirectional antennas facing forward. . . . .	69
5.4	Localization of breathing person in position A (measurement 5) (X,Y) cut . . . . .	70
5.5	Localization of breathing person in position B (measurement 3) (X,Y) cut . . . . .	70
5.6	Localization of breathing people in position AB in anechoic chamber (X,Y) cut. Measurement 9 . . . . .	71
5.7	Schematic of board positions in car measurements, where A and B represent the evaluated positions for targets in the car. . . . .	74
5.8	(Left): Tx1 , Rx monostatic 1, Rx bistatic 2 in vehicle measurements placed in the back. Omnidirectional antennas facing downwards. (Right): Tx2 , Rx monostatic 2, Rx bistatic 1 in vehicle measurements placed in the front. Omnidirectional antennas facing forward. . . . .	77
5.9	Localization of breathing person in position A (X,Y) cut (measurement 27) . . . . .	77
5.10	Localization of breathing person in position B (X,Y) cut (measurement 34) . . . . .	78
5.11	Localization of breathing people in positions A and B (X,Y) cut (measurement 44) . . . . .	79
A.1	Block diagram of multistatic UWB network capturing system . . . . .	100

---

B.1	(Left) : Monostatic CIR radar data. Tx board operating at Code 0 and Rx board operating at Code 0.   (Right) : Bistatic CIR radar data. Tx board operating at Code 0 and Rx board operating at Code 0. However, Tx board operating at Code 5 was closer, thus interference lines appear due to sensitivity adjustment to incorrect echo. . . . .	102
B.2	Range-Slow Time Monostatic Rx 1 measurement . . . . .	104
B.3	Range-Slow Time Bistatic Rx 1 measurement . . . . .	104
B.4	Range-Slow Time Monostatic Rx 2 measurement . . . . .	104
B.5	Range-Slow Time Bistatic Rx 2 measurement . . . . .	104

# LIST OF TABLES

1.1	Vital Signs estimation technologies, with their advantages and disadvantages, describing if the technology allows for non-contact monitoring and presence detection. . . . .	4
1.2	Summary of main studies from the literature on vital signs with UWB radar . . . . .	6
1.3	Classification of different approaches to detect multiple people in a scenario using UWB radar . . . . .	7
1.4	Identified literature assumptions incompatible with our problem constraints . . . . .	8
2.1	Classification Pipeline output . . . . .	23
3.1	UWB Ranger4 parameters ([55]) . . . . .	32
3.2	Final definition of board design, anchor structure and multiplexing method . . . . .	38
4.1	Comparison between the real ranges to the reflective object and the measured ranges with the different radars after correction of range offset has been applied. . . . .	48
4.2	Human simulation used parameters. Note that the chest displacement and the chest size (ellipsoid model sizes) have realistic values from [2] . . . . .	50
4.3	Comparison between the obtained ranges to the simulated human and the defined ranges with the different radars . . . . .	52
4.4	Definition of the parameters related to the location/topology of the radar units for the simulated test . . . . .	53
4.5	Human simulation used parameters. Note that the chest displacement and the chest size (ellipsoid model sizes) have realistic values from [2] . . . . .	53
4.6	Detections matrix comparison to true target range and breathing frequency . . . . .	55
4.7	Important parameters for processing and how they affect the data . . . . .	57
5.1	Board configuration in measurements and simulation in ideal scenario in anechoic chamber . . . . .	64
5.2	Human simulation coordinates in anechoic chamber . . . . .	64
5.3	Human-occupancy distribution in anechoic chamber . . . . .	65
5.4	Parameter range values used for both the processing of the measurements and the simulations alike . . . . .	65
5.5	Ranges of values used for the simulations of humans in the anechoic chamber environment . . . . .	66
5.6	Result of Monte Carlo Simulations, where Scenario indicates the type of scenario simulated as seen on Table 5.3 and performance metrics are shown for each of them. . . . .	68

5.7	Board configuration for in-car measurements . . . . .	73
5.8	Human position coordinates in vehicle . . . . .	73
5.9	Human-occupancy distribution in vehicle . . . . .	74
5.10	Positions of simulated flat PEC planes used to emulate static objects such as walls or ceiling in which echos rebound and form multipath. . . . .	75
5.11	Results of Monte Carlo simulations where Scenario indicates the type of scenario simulated as seen on Table 5.9 and performance metrics are shown for each of them. . . . .	75
5.12	Board positioning for simulation of setup with increased spatial diversity w.r.t. simulations in vehicle performed so far. . . . .	82
5.13	Result of Monte Carlo Simulations for board re-positioning for added spatial diversity ('Sep'), vs results presented for non-separated boards in section 5.2 ('Prev'), both with double targets placed in occupancy areas A and B. . . . .	82
5.14	Board configuration for in-car measurements after lowering anchor 1 for increased PD . . . . .	83
5.15	Result of Monte Carlo Simulations for lowering boards in the back for increased PD ('Low'), vs results presented for boards placed in the ceiling as defined in section 5.2 ('Prev'), both with double targets placed in occupancy areas A and B. . . . .	83
C.1	Evaluation of the results performed in the anechoic chamber of TU Delft using the proposed processing pipeline. The people column refers to the positions of the targets placed in a the environment following the coordinates defined in Table 5.2. The values for the parameter 2D-CFAR $P_{fa}$ are noted. The evaluation metrics defined for the 2 processing blocks are evaluated. For detection, the number of detected humans in every measurement is noted, together with the number of false alarms and the range error for those targets detected. For association, the final number of targets located is written, together with the number of missed targets, ghost targets and localization RMSE for those targets which can be localized in the environment. The threshold for the Probability of Target has been set at 75%. . . . .	106
D.1	Evaluation of the results performed in NXP's test car using the proposed processing pipeline. The people column refers to the positions of the targets placed in a the environment following the coordinates defined in Table 5.8. The values for the parameter 2D-CFAR $P_{fa}$ are noted. The evaluation metrics defined for the 2 processing blocks are evaluated. For detection, the number of detected humans in every measurement is noted, together with the number of false alarms and the range error for those targets detected. For association, the final number of targets located is written, together with the number of missed targets, ghost targets and localization RMSE for those targets which can be localized in the environment. The threshold for the probability of target has been set at 75% . . . . .	108

# TABLE OF CONTENTS

<b>Foreword</b>	<b>iii</b>
<b>Abstract</b>	<b>v</b>
<b>List of Figures</b>	<b>vii</b>
<b>List of Tables</b>	<b>xi</b>
<b>1 Introduction and Literature Review</b>	<b>1</b>
1.1 Motivation for research and thesis purpose . . . . .	1
1.2 Wireless Vital Signs estimation technologies . . . . .	2
1.3 Literature review on UWB radar for vital signs and presence detection . . . . .	5
1.3.1 Vital-Sign Estimation using UWB radar . . . . .	5
1.3.2 Human Presence Detection using UWB radar . . . . .	6
1.3.3 Detection and vital-sign estimation of multiple people . . . . .	7
1.4 Identified gaps in the literature . . . . .	8
1.5 Novelty Contribution of the thesis . . . . .	9
1.6 Thesis Structure. . . . .	10
<b>2 Algorithms for multiple people detection and localization with multistatic UWB network</b>	<b>13</b>
2.1 Model definition for vital signs signature in UWB radar . . . . .	14
2.1.1 Radar data matrix structure . . . . .	14
2.1.2 Model of breathing radar measurement . . . . .	15
2.1.3 Model of breathing human verification . . . . .	17
2.1.4 Conclusions on Vital Signs Extraction . . . . .	18
2.2 Detection processing pipeline explanation . . . . .	19
2.2.1 Data filtering. . . . .	20
2.2.2 Identification of ranges at which humans are present . . . . .	20
2.2.3 Classifier to discard false detections . . . . .	23
2.2.4 Output of detector . . . . .	24
2.3 Data Association . . . . .	25
2.3.1 Association hypothesis. . . . .	25
2.3.2 Association algorithm . . . . .	27
2.3.3 Localization of associated targets . . . . .	29
2.3.4 Known limitations of the defined association algorithm . . . . .	29
2.4 Conclusions on the proposed algorithms for multiple people detection and localization . . . . .	30

<b>3</b>	<b>Multistatic radar network design and simulation</b>	<b>31</b>
3.1	Multistatic UWB network	31
3.1.1	Definition of the Hardware.	31
3.1.2	Dual-Board system.	32
3.1.3	Multistatic radar network: steps for setup construction and validation	33
3.1.4	Range calibration with the current setup.	38
3.1.5	Conclusions on construction of multistatic UWB radar network	39
3.2	Simulation of CIR data	40
3.2.1	Human modelling	40
3.2.2	Part 2: Static objects	42
3.2.3	Part 3: Modelling of multipath	43
3.2.4	Final expression for modeling CIR data with humans, static clutter, and multipath components	44
3.2.5	Simulation limitations	45
<b>4</b>	<b>Preliminary Validation in a Controlled Environment</b>	<b>47</b>
4.1	Validation of the CIR radar data obtained with the UWB radar network	47
4.1.1	Results for dihedral range validation in anechoic chamber.	48
4.1.2	Conclusions on range validation in anechoic chamber.	50
4.2	Validation of the simulated CIR radar data	50
4.2.1	Results for simulation range validation in ideal environment	50
4.2.2	Conclusions on range validation for the simulation	52
4.3	Validation of the algorithm performance with simulated CIR radar data in controlled setup.	52
4.3.1	Definition of simulation environment	52
4.3.2	Processing of the simulation	53
4.3.3	Conclusions on the processing of the simulation with the developed algorithm	56
4.4	The effect of the parameters	57
4.4.1	Duration	57
4.4.2	2D-CFAR $Pfa$	58
4.4.3	FFT Window Size.	60
4.5	Conclusions on the validation.	61
<b>5</b>	<b>Extensive Experimental Validation</b>	<b>63</b>
5.1	Measurement setup and CIR Simulation comparison in the anechoic chamber	64
5.1.1	Performance evaluation with Monte Carlo Simulations of CIR radar data	66
5.1.2	Conclusions on the analysis of the Monte Carlo simulation results.	68
5.1.3	Measurements in anechoic chamber.	68
5.1.4	Comparison between the experimental measurements and the simulations in the anechoic chamber	71

5.2	Measurement Setup and CIR Simulation Comparison In-Vehicle . . . . .	73
5.2.1	Performance Evaluation with Monte Carlo Simulations of CIR Radar Data in-vehicle. . . . .	75
5.2.2	Conclusions on the analysis of the Monte Carlo simulation results. . . . .	76
5.2.3	Measurements in vehicle. . . . .	76
5.2.4	Comparison between the experimental measurements and the sim- ulations in the vehicle . . . . .	79
5.3	Conclusions on experimental validation of the measurements and the ef- fect of multipath . . . . .	80
5.4	Repositioning of the boards via simulation . . . . .	81
5.4.1	Separation of the boards that form the anchors for increased spatial diversity . . . . .	81
5.4.2	Board lowering for increased probability of detection . . . . .	82
5.4.3	Conclusions on the proposal of new setups . . . . .	84
5.5	Comparing results to SOTA . . . . .	84
5.6	Conclusions of the experimental validation. . . . .	85
<b>6</b>	<b>Conclusions and Future Work</b>	<b>87</b>
6.1	Conclusions. . . . .	87
6.2	Future Work. . . . .	89
	<b>Bibliography</b>	<b>96</b>
	<b>Appendices</b>	<b>97</b>
<b>A</b>	<b>ROS capturing architecture block diagram</b>	<b>99</b>
<b>B</b>	<b>Multiplexing techniques investigated for the multistatic UWB network</b>	<b>101</b>
B.1	Code Division Multiple Access Implementation. . . . .	101
B.2	Time Division Multiple Access Implementation. . . . .	103
B.3	Frequency Division Multiple Access Implementation . . . . .	103
<b>C</b>	<b>Measurement processing results of Anechoic Chamber</b>	<b>105</b>
<b>D</b>	<b>Measurement processing results of In-vehicle experiments</b>	<b>107</b>



# GLOSSARY

- k*-NN** *k*-Nearest Neighbor. 27
- 2D-CFAR** 2D - Constant False Alarm Rate. 21
- CDMA** Code Division Multiple Access. 35
- CIR** Channel Impulse Response. 14
- CPD** Child Presence Detection. 2
- EEMD** Ensemble Empirical Mode Decomposition. 5
- FA** False Alarm. 66
- FDMA** Frequency Division Multiple Access. 36
- FFT** Fast Fourier Transform. 5, 21
- FMCW** Frequency Modulated Continuous Wave. 2
- GLRT** Generalized Likelihood Ratio Test. 5
- LoS** Line of Sight. 35
- MIMO** Multiple Input Multiple Output. 7
- MLAT** Multilateration. 27
- PD** Probability of Detection. 66
- PRI** Pulse Repetition Interval. 15
- RCS** Radar Cross Section. 8
- RMSE** Root Mean Square Error. 67
- ROS** Robot Operating System. 37
- Rx** Receiver. 13, 32
- SIMO** Single Input Multiple Output. 7

- SNR** Signal to Noise Ratio. [3](#)
- SOTA** State of The Art. [2](#)
- STFT** Short-Time Fourier Transform. [17](#)
- SVD** Signal Vector Decomposition. [5](#)
- TDMA** Time Division Multiple Access. [36](#)
- TDOA** Time Difference of Arrival. [14](#)
- Tx** Transmitter. [32](#)
- UWB** Ultra Wide Band. [2](#)
- VMD** Variational Mode Decomposition. [5](#)

# 1

## INTRODUCTION AND LITERATURE REVIEW

*In this chapter the research problem investigated in this thesis is presented, together with a literature review that summarizes the main points in the state of the art of radar-based vital signs estimation in cabin, both in terms of hardware and software/algorithm development. The main contribution of the thesis are then also described.*

### 1.1. MOTIVATION FOR RESEARCH AND THESIS PURPOSE

The ability to detect human vital signs such as respiration and heartbeat amongst others has many different use-cases. Particularly for the healthcare industry, being able to track vital signs presents a great advantage both in the monitoring and caring of patients, and also in other areas related to healthcare such as sleep pattern classification, including apnea detection [1, 2, 3] and particularly for baby apnea detection [4], or for monitoring older people from their homes [5] to detect critical events such as falls.

Current solutions such as wearable wristbands for IR-heartbeat monitoring, respiration belts for breathing frequency tracking or electrodes for electrocardiogram (ECG)s, require direct contact with the skin of the patients, thus limiting their mobility and facilitating the spread of contagious infections between patients and hospital staff members [6], as was recently the case with COVID-19. In some more extreme cases, such as patients in intensive care units and low-birth-weight newborn care units, even a simple skin defect initiated when electrodes detach from an unconscious patient may serve as a route of entry for serious infections [7]. Therefore, the use of contact technologies for patient care is not only dangerous in some situations, but may even be inapplicable in others, as is the case of newborns or burnt-victims, or for in-home elderly care.

Therefore, a wireless solution for vital signs estimation is necessary. This does not only solve the discomfort of wearing devices, but it also enables the use of wireless vital signs estimators for many other applications outside the area of healthcare, such as the localization of trapped victims after disasters [8], or for through-wall people detection [9].

In the recent years, a new application for vital signs estimation has emerged in the Automotive industry. In the Roadmap of 2025, EURO NCAP has announced that it will reward car-manufacturers who include Child Presence Detection (CPD) technologies in their vehicles [10] starting from 2022. This is due to the fact that even in normal weather conditions, around 16°C, the temperature inside of a vehicle can escalate to around 40°C in just about an hour if parked directly under the sun. Therefore, leaving a child unattended in a parked car, even for a few minutes, can lead to heat-stroke and death. Sadly, numerous cases of this occurrence are reported yearly in the whole world. Therefore, a solution capable of identifying if a child has been left unattended in a car could help preventing such accidents. By observing the presence or absence of vital signs in the vehicle, a CPD solution can be developed.

Moreover, currently seatbelt reminders are based on pressure sensors positioned under the seats. These can be falsely triggered when transporting large objects. With wireless vital signs estimation, false alarms due to non-human targets could be avoided, by basing the detection of people on vital-sign presence rather than weight sensing.

Therefore, particularly in the automotive industry for the use cases of CPD and people localization in cabin, a solution based on wireless vital signs estimation is necessary.

**The purpose of this thesis is to develop a system that is capable of detecting and accurately locating an unknown number humans inside a vehicle based on the concept of wireless vital signs estimation.**

In the next section, different technologies for wireless vital signs estimation are evaluated.

## 1.2. WIRELESS VITAL SIGNS ESTIMATION TECHNOLOGIES

In the recent years, advancements have been made in the State Of the Art (SOTA) in academia and industry for wireless vital-sign estimation. Some existing solutions presented have been compared.

Particularly radar has been investigated. Both Frequency Modulated Continuous Wave (FMCW) radar and pulse Ultra Wide-Band (UWB) radar offer solutions for remote vital signs extraction. FMCW radar radiates power continuously, but varies in time the frequency used for the modulation of the transmitted signal, allowing it to avoid the transmission of high peak power signals. The receiver can then observe the delayed change of frequency presented by the radar echos w.r.t the transmitted signal and accurately estimate the range and radial velocity of the targets which are under surveillance [11].

For pulsed-UWB radar, pulses modulated with a particular frequency are transmitted, and the range and velocity of the targets is extracted by measuring the delay of the received echos and the phase differences w.r.t the transmitted pulse.

Both FMCW radar and UWB radar operate at much larger bandwidths than other radar technologies, resulting in finer range resolution than conventional radars. This makes both technologies a suitable solution for the detection of humans, and particularly for the detection of small movements, as can be the displacement of the chest due to breathing, enabling the use-case of wireless human vital-sign extraction [12].

For UWB radar particularly, the frequency operation range is relatively low, of 6 to 8 GHz [13], thus making UWB radar capable of penetrating through some objects [14]. This protocol also requires low transmitted-pulse power, which enables UWB radar to coexist with other technologies present in the same environment without interfering with them. The evident downfall of the decrease in transmit power is that Signal to Noise Ratio (SNR) values decrease as well, making it susceptible to high noise levels.

A comparison between FMCW radar and UWB radar for vital-sign estimation was made in [15] and it was concluded that precisely because of the aforementioned advantages, UWB is the better fit.

On another note, WIFI [16, 17] can also be used for both vital signs estimation and for gesture detection. Moreover, this solution is cost effective, since it can even reuse off-the-shelf technologies such as smartphones. However, it is not capable of localization and it may interfere with existing technologies in the environment.

Cameras are similarly cost-effective and have been proven to accurately track breathing and heart-rates through the observation of people's faces[18]. However, they suffer from environmental dependence, given that they require a clear view of the person, and privacy issues might be raised.

A summary of the different vital-sign estimation techniques can be seen on Table 1.1, together with their advantages and disadvantages.

What can be concluded from this comparison is that UWB radar poses one of the most appropriate solutions for wireless vital signs detection. It is much more reliable in all environmental conditions and offers the possibility of localization.

In the next section, a review of the SOTA is presented, in which contributions made on the use of UWB radar for vital signs estimation are discussed.

Various literature gaps are identified for the research purpose of this thesis, and the novelty presented by the project is explained.

Technology	Description	Advantages	Disadvantages
FMCW radar [11]	Capable of detecting small movements associated to breathing	<ul style="list-style-type: none"> <li>• Non-invasive</li> <li>• Good range accuracy</li> </ul>	<ul style="list-style-type: none"> <li>• Expensive data processing</li> </ul>
UWB radar [13]	Capable of detecting small movements associated to breathing	<ul style="list-style-type: none"> <li>• Non-invasive</li> <li>• Cost-efficient</li> <li>• Localization</li> <li>• Transparent to existing technology</li> <li>• High penetration power</li> </ul>	<ul style="list-style-type: none"> <li>• Requires data processing</li> </ul>
WIFI [16, 17, 14]	Relies on observing changes in the TDOA of WIFI signal reflections	<ul style="list-style-type: none"> <li>• Non-invasive</li> <li>• Reuses infrastructure</li> </ul>	<ul style="list-style-type: none"> <li>• No localization</li> <li>• Electromagnetic interference</li> </ul>
Camera [18]	Automatic face tracking and skin-color tracking for heartbeat monitoring.	<ul style="list-style-type: none"> <li>• Reuses infrastructure</li> <li>• Transparent to existing technology</li> </ul>	<ul style="list-style-type: none"> <li>• Requires direct view on target</li> <li>• Depends on environmental conditions</li> </ul>

Table 1.1: Vital Signs estimation technologies, with their advantages and disadvantages, describing if the technology allows for non-contact monitoring and presence detection.

### 1.3. LITERATURE REVIEW ON UWB RADAR FOR VITAL SIGNS AND PRESENCE DETECTION

More than 100 papers on vital signs estimation, presence detection and localization using UWB radar technologies have been reviewed for this thesis work. Mainly, the literature focuses on both single person or multiple people vital signs estimation, on human localization in a closed environment, and on the usage of multiple radars for these purposes.

Summaries of these topics from the most significant papers are enclosed in the following sub-sections, followed by the gaps that have been identified in each topic and how this thesis plans to bridge the gaps in them.

#### 1.3.1. VITAL-SIGN ESTIMATION USING UWB RADAR

Abundant literature is available on the estimation of breathing frequency for a static breathing human scenario in which the presence of a person is assumed. UWB technology used for both respiration and heartbeat estimation shows promising results. Mainly, the literature relies on the assumption that a static human being is close to the radar and attempts to find an optimal solution to extract their vital signs information using processing techniques. By finding the range at which the human reflection is present, the fluctuations in amplitude and phase due to the breathing motion can be studied.

Firstly, noise-cancelling and clutter-removal techniques such as frequency filtering, Kalman filters [6] or Signal Vector Decomposition (SVD) can be applied to clean the signal as in [19, 20, 21]. In [22], the authors employ a variation of Ensemble Empirical Mode Decomposition (EEMD) algorithm to remove the noise. In [23], a new algorithm based on an adaptive weighting factor to update clutter map is proposed.

After removing clutter, the range where the human is present is identified. Some studies such as [6] consider the range bin which presents a maximum variance in time. Others such as [24] select the maximum range in a histogram of ranges with the maximum peak power for all values in time. In [25], the range is found by performing a Fast Fourier Transform (FFT) to obtain a range-Doppler plot and selecting the maximum energy peak after frequency filtering for a normal breathing range (0.1 - 0.8 Hz).

In order to identify the breathing frequency, many papers such as [26] or [6] compute the FFT in the slow-time and observe the maximum in the spectrum, corresponding to the frequency of the chest displacement due to breathing. In [25], Generalized Likelihood Ratio Test (GLRT) is employed to estimate the maximum breathing frequency. The heartbeat peak is much weaker, and might be masked by the breathing peak harmonics. A harmonic cancelling filter can be applied in order to correctly identify the heartbeat frequency. This technique however, fails when the heartbeat falls in the same range as a harmonic of the breathing signal. Other methods to identify the breathing frequency without relying on the resolution of the FFT are EEMD or Variational Mode Decomposition (VMD). In [1] and [27] decomposition methods are investigated. It is concluded that

EEMD is not suitable for noisy signals, and that the better option out of the two is VMD [28].

Moreover, these algorithms assume that the position of the radar is in front of the subject, perpendicular to its chest. In [29], the authors demonstrate the effectiveness of placing the radar on the back, for a better view of the heartbeat signal, thus proving that an interesting study could result from investigating different positions of the radar with respect to the subject. In [30] vital signs estimation is demonstrated by placing the radar on the bottom of the seat.

A summary of these techniques is presented in Table 1.2

Type of technique	Literature
Noise cancelling	[6] [19, 20, 21] [22] [23]
Range estimation	[6] [24] [25]
Breathing frequency	[26] [1] [27] [25] [28]
Radar in non-frontal position	[29] [30]

Table 1.2: Summary of main studies from the literature on vital signs with UWB radar

All of these solutions rely on the assumption that a human is already present in the environment. This is a fair assumption for healthcare applications, but it is not so in an automotive environment in which human presence cannot be predicted. In the following section, literature on human presence detection using UWB radar is reviewed.

### 1.3.2. HUMAN PRESENCE DETECTION USING UWB RADAR

It is possible to study the presence/absence of the breathing motion in the received radar data, even though it has been scarcely studied in the literature. In [25], the GLRT method is used on the FFT of the identified breathing signal to determine if it is a human breathing pattern or a noise sample. In [31], a processing chain was developed for vital signs estimation which included a consideration for the 'non-detection' of a human.

Moreover, the consideration must be made for the case in which the human is not standing still. Body movements such as swinging the arms, turning around, leaving/entering vehicle, will completely overshadow the breathing motion in the radar data. For example, in In [31], the application detects when the subject is moving by establishing a threshold in the variance of its signal auto-correlation.

It must also be taken into consideration that more than one person might be present in the car environment. In the following section, the available literature on multiple-people presence detection and vital signs estimation is discussed.

### 1.3.3. DETECTION AND VITAL-SIGN ESTIMATION OF MULTIPLE PEOPLE

The solutions presented for multiple-people detection are based on the differentiation of the range and frequency at which the different vital signs appear, or on the angular differentiation of multiple people in the same range. For this, all solutions use UWB radars which rely on multiple antennas.

In [32, 33, 34], the authors evaluate the different ranges (known a priori) at which different static human breathing signals can be identified. Similarly in [35], the authors perform an FFT in the slow-time and apply a band-pass filter tuned to the possible breathing frequencies to identify at which ranges the humans are present, given that the exact number of people is known. However, this method can easily lead to false alarms in closed environments where the multipath effect might create high-energy echos.

There might be other scenarios in which the signal corresponding to the multiple targets is detected at the same range. In [36], the authors use Multiple Input Multiple Output (MIMO) radar to perform beamforming and obtain angular resolution on the evaluated area. Differently, in [37, 38], the VMD algorithm is studied to separate the 2 independent vital-signals that are found on the same range bin. However, this approach assumes that both vital signs will appear at the same energy level, and that they will be differentiated in frequency.

In [39] the authors are able to clusterize 3 static people through an NP-AP algorithm after sparse enhancement using Single Input Multiple Output (SIMO) radar. However, this heavily relies on the space-frequency differentiation of the signals. A similar approach is taken by Koda et al. in [40], in which a 79GHz FMCW MIMO radar is used.

Finally, in [41], the multiple-people estimation problem is tackled by machine learning. A single mono-static radar placed on the rear mirror in the front of the car illuminated the scene, in which up to 5 passengers are placed in the car. The authors pick the most representative features of the radar data and processes them in decision trees with ensemble learning.

In Table 1.3, a summary of the different approaches to detect multiple people is presented.

Known ranges	Same range	Processing	Literature
Yes	No	-	[32, 33, 34]
No	No	Filtering and FFT	[35]
No	Yes	MIMO beamforming	[36]
No	Yes	VMD for signal separation	[37, 38]
No	No	Range-frequency clustering	[39], [40]
No	No	Deep Learning	[41]

Table 1.3: Classification of different approaches to detect multiple people in a scenario using UWB radar

The downfall of most of these algorithms is that they rely on prior knowledge of the ranging of the person, assume that a certain number of people is present, or use MIMO radar for angular estimation of targets at the same range.

In the automotive scenario, there might be more than one person present, and it is likely that the people will appear at very close ranges, if not at the same range, depending on their position. Some of the proposed signal-separation techniques can be applied in order to mitigate this effect but it is likely that the echos from different people will not have the same energy, depending on the person's Radar Cross Section (RCS) and the position of the radar. This would make it hard to detect multiple people.

For this reason, in a closed environment such as the car, illuminating the scene from a single point, especially when more than one person is present, would make it hard to detect and localize different humans.

Therefore, it is proposed to use a network of UWB radars. Illuminating the scene from various points could allow better detection and localization in these environments. By fusing the detections obtained by the multiple multistatic sensors, the overall system can become more reliable and provide increased detection probability [42].

#### 1.4. IDENTIFIED GAPS IN THE LITERATURE

It can be seen how most of the literature relies on a series of assumptions that are not compatible with our system constraints, namely the fact that the number of people and their positions inside the car is not known, and that the car itself is a multipath-dense environment which makes localization challenging. These constraints are relevant for the research problem investigated in collaboration with NXP.

A summary of the incompatibility of the literature assumptions with the defined constraints has been made on Table 1.4.

Literature Assumption	System Constraint
Number of people is known	Number of people is unknown
People remain static	People can move
Person location w.r.t. the radar is known	Location is arbitrary
MIMO radars are used for human separation	Complex multipath environment
One radar can detect and separate multiple people	Targets might be occluded by others

Table 1.4: Identified literature assumptions incompatible with our problem constraints

As can be seen, one of the greatest challenges in radar-based remote applications is to estimate the number and position of stationary people in a closed environment [43]. Solutions in the literature rely on the a priori knowledge of the number of people in the environment or the position of the people. Moreover, the hardware used, even if it allows for angular information, only illuminates the scene from a single point of view, and has only been tested in low-multipath environments.

## 1.5. NOVELTY CONTRIBUTION OF THE THESIS

In order to bridge the gaps identified to find a solution to our problem, several contributions are proposed in this thesis. They have been summarized below as:

- The design and construction of a multistatic radar network using UWB radars. A proposal is made to exploit a network of strategically-placed multistatic radars to observe the inside of the vehicle from multiple focus points. By illuminating the subjects from various angles at the same time, the probability of detection of low-RCS targets and of multiple targets is expected to increase. The use of multiple radars will also allow for localization in a 3D space.
- A novel algorithm to process the data from the network will be presented. This algorithm will both present a solution to detect vital signs based on the improvement of existing literature, and to fuse the information of all radars in the network in order to perform multiple-target localization. The output will be the position estimates of the localized people in our environment.
- A framework for simulating the radar data from the multistatic network. This will allow the validation of multiple network topologies that cannot be verified experimentally, and a statistical study of the results presented. Simulated data from the network showed good agreement with the experimental data.

Furthermore, the results of this thesis are being written up for a journal paper to be submitted to IEEE Sensors.

In the following section, a summary of the thesis structure is given.

## 1.6. THESIS STRUCTURE

The development of this thesis has been distributed in 5 distinct parts. A schematic block diagram of the different parts can be seen on Figure 1.1

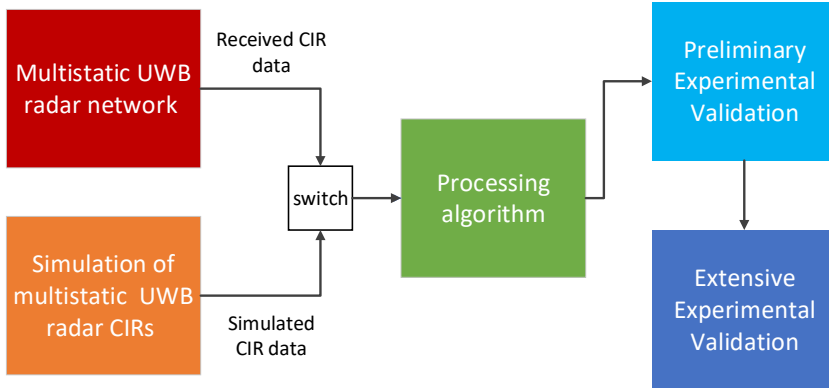


Figure 1.1: Block diagram of methodology blocks

Firstly, in Chapter 2, a full processing pipeline is developed on MATLAB capable of processing the data captured by a multistatic radar network. At each radar node, vital-signs are detected and, in a later stage, the detections from the sensors are centrally associated using machine learning-based data fusion. The different fusing hypothesis are evaluated, discarding false alarms and overcoming missed detections. The final output is the localization of multiple people on the defined environment. This algorithm considers the identified constraints for our environment, presents a novel model for human breathing observed by the radar and defines an improved approach for detection and localization while tackling complex sensor fusion in multipath-dense environments with an unknown number of targets.

Secondly, in Chapter 3, the necessary hardware equipment will be designed and constructed in order to test the solution. This will be done using NXP's UWB IC: Ranger 4. Moreover, given the complexity of using the prototype setup for batch-measurements, a novel simulation is developed to model the complex CIR data received by the multistatic radar network. This simulation will consider multiple targets and multipath reflections with highly reflective static objects.

Thirdly, the developed solution will be validated in Chapter 4 by testing both the hardware and simulations, together with the algorithm. It is concluded that the proposed radar network is capable of accurately detecting targets with improved ranging accuracy w.r.t. SOTA techniques, and the importance of some key-parameters in the detection stage is evaluated.

In Chapter 5, extensive experimental results are validated. Firstly, the results obtained with the experimental measurements taken in TU Delft's anechoic chamber are compared to those obtained by the generation of radar data using the proposed simulation framework in a Monte Carlo fashion. The performance metrics defined are evaluated. Secondly, the same test is repeated for measurements in a vehicle in NXP's facilities in the High Tech Campus. Given the obtained results, different network topologies are proposed and evaluated through simulations to overcome the pitfalls identified.

Finally, conclusions for this thesis are drawn and future work is proposed in Chapter 6.



# 2

## ALGORITHMS FOR MULTIPLE PEOPLE DETECTION AND LOCALIZATION WITH MULTISTATIC UWB NETWORK

*The proposed algorithm consists of two main blocks: the detection block and the association block.*

*In this Chapter, after an explanation of the signal model for vital signs signature in UWB radar, the detection block is explained. A model for a human breathing radar signature is developed, based on which a detection pipeline is presented, capable of identifying the ranges at which humans are present and their estimated breathing frequencies in a decentralized way. That is, the information from each of the receivers (Rx) is independently evaluated and a detection matrix is provided for each of the Rx in the network.*

*Secondly, the association block is presented. The resulting detections from the individual Rx are associated using machine learning based data fusion in order to properly locate targets in the environment while discarding ghost targets. This block can thus provide a final estimate of the position of the targets after combining the information of all Rx. For this centralized algorithm, the assumption is made that the positions of the radars are known.*

*An overview of this process can be observed in Figure 2.1*

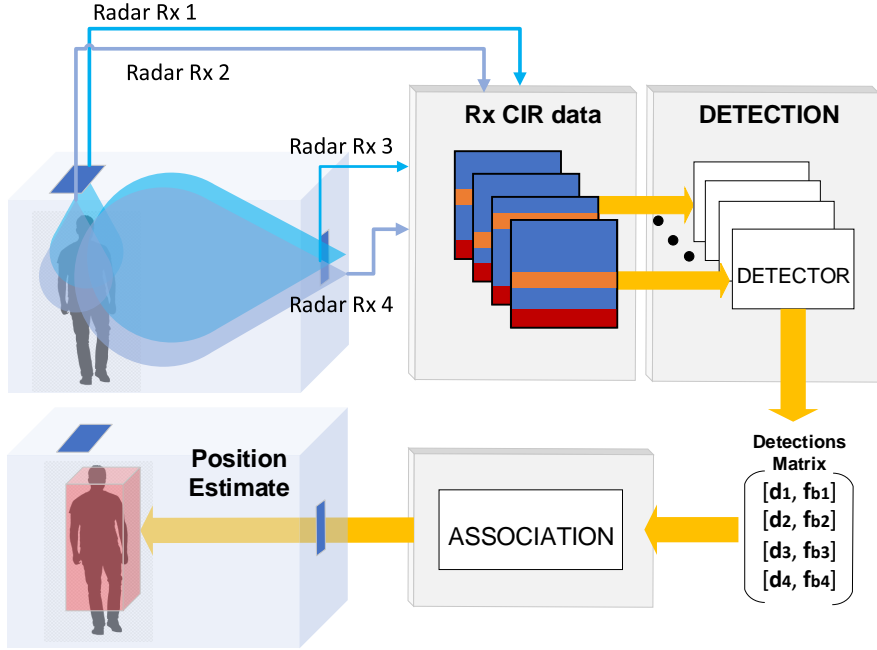


Figure 2.1: Blocks for the proposed processing pipeline for detection and localisation of humans with multi-static UWB radar network, where the main contributions of this work are the detection and data association algorithms. The output of the detection algorithm is a detection matrix containing the range and breathing frequency of the identified humans. After the fusion of detections in the association algorithm, the output is an estimation of the position of the humans.

## 2.1. MODEL DEFINITION FOR VITAL SIGNS SIGNATURE IN UWB RADAR

Before delving into the explanation of the development of the detection block, a brief explanation of the radar data matrix is given, followed by a study on how the breathing motion is characterized in a radar measurement and which properties can be used for its extraction. A model is developed to account for a periodic breathing movement of a human as seen by a radar. Later, the model is compared with experimental data.

### 2.1.1. RADAR DATA MATRIX STRUCTURE

Measurements are recorded in  $X(m, n)$  matrix which defines the Channel Impulse Response (CIR) where  $m$  is the number of taps in the fast-time (range) and  $n$  is the number of pulses transmitted over time (Slow-time). After one pulse is sent, the received echos are sampled with  $f_s$  sampling frequency. The delay with which echos arrive at the Rx can be expressed as the Time Difference of Arrival (TDOA)  $\tau$ , which can directly be related to

the round-trip distance travelled by the signal with  $R = c\tau$ . Therefore, the resolution in range can be defined as  $\Delta R = \frac{c}{f_s}$ .

The resolution in time is therefore determined by the Pulse Repetition Interval (PRI), or the time span between the transmission of pulses, in which the radar 'listens' for the received echos. This value can be changed in the order of milliseconds - microseconds, and will affect the maximum unambiguous range as  $R_{max} = cPRI$ . In Figure 2.2, a schematic view of the CIRs data matrix can be seen.

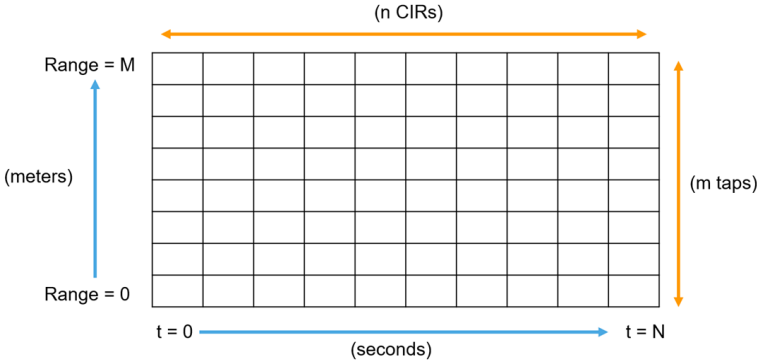


Figure 2.2: CIRs data matrix structure

For a static human in our environment, the detection will appear as a constant-range high-energy echo corresponding to the human body, modulated in phase and amplitude by the displacement of the human chest with breathing. Therefore, by extracting the frequency information of the appropriate range bin, the breathing frequency can be estimated.

### 2.1.2. MODEL OF BREATHING RADAR MEASUREMENT

The received radar signature  $x_h(\tau, t)$  from a human being at a certain distance  $d(t)$  can be characterized as the convolution of a transmitted pulse  $s(\tau)$  with the channel model of the human chest  $h(\tau, t)$  as similarly defined in [44]. However, what most literature fails to consider is the fact that this model can be characterized as a fluctuating amplitude  $\alpha(t)$  corresponding to the target RCS and a deterministic delay  $\tau_d(t) = \frac{2*d(t)}{c}$ . This can be seen in Equation 2.1, where  $p(\frac{\tau}{T_p})$  corresponds to the transmitted pulse envelope,  $f_c$  is the frequency and  $A$  is the pulse amplitude.

$$\begin{aligned}
 s(\tau) &= Ap\left(\frac{\tau}{T_p}\right) \cos(2\pi f_c \tau) \\
 h(\tau, t) &= \alpha(t) \delta(\tau - \tau_d(t)) \\
 x_h(\tau, t) &= s(\tau) * h(\tau, t) \\
 &= A\alpha(t) p\left(\frac{\tau - \tau_d(t)}{T_p}\right) \cos(2\pi f_c (\tau - \tau_d(t)))
 \end{aligned} \tag{2.1}$$

Due to the periodic movement of the human chest with respect to the UWB antennas, the time-varying distance  $d(t)$  can be modelled as a central distance  $D_b$  and a smaller periodic distance variation  $m_b$  corresponding to the chest displacement in meters as the human's chest expands and contracts.  $f_b$  corresponds to the breathing frequency of the person. This can be seen in Equation 2.2.

$$d(t) = D_b + m_b \sin(2\pi f_b t) \quad (2.2)$$

The amplitude of the channel model  $\alpha(t)$  corresponds to the fluctuation in human RCS as the person exhales and inhales. In the literature, this is usually considered to be a simple static amplitude observed in the same range bin. However, When the person inhales, the RCS of the human will have a maximum value as the chest expands, and correspond to a minimum value in  $d(t)$ . When the person exhales, the chest will move away from the radar presenting a maximum in  $d(t)$  and a minimum in  $\alpha(t)$ . This relationship can be seen in Equation 2.3,

$$\alpha(t) = \Gamma - \beta \sin(2\pi f_b t) \quad (2.3)$$

where  $\Gamma$  is the standing human RCS and  $\beta$  models the amplitude of RCS change due to breathing.

When the signal  $x_h(\tau, t)$  is processed by the IQ receiver, the signal is down-mixed in phase and quadrature and low-pass-filtered as can be seen in the Figure 2.3. The resulting operation and the final down-mixed signal  $y_h(\tau, t)$  can be obtained from Equation 2.4.

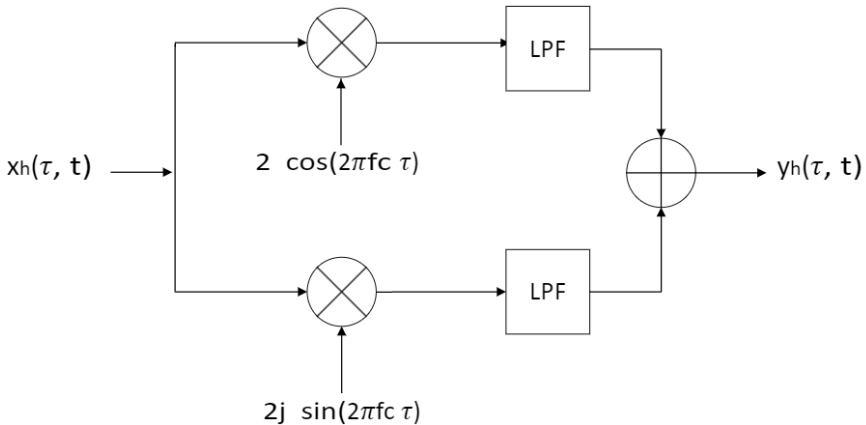


Figure 2.3: IQ Demodulator and Low-Pass-Filter schematic

$$\begin{aligned} y_h(\tau, t) &= \text{LPF} \left( x_h(\tau, t) 2[\cos(2\pi f_c \tau) + j \sin(2\pi f_c \tau)] \right) \\ &= \text{LPF} \left( 2A\alpha(t) p\left(\frac{\tau - \tau_d(t)}{T_p}\right) \cos(2\pi f_c(\tau - \tau_d(t))) [\cos(2\pi f_c \tau) + j \sin(2\pi f_c \tau)] \right) \end{aligned}$$

The I branch result of the demodulator can be calculated applying

$$\begin{aligned} \cos(A) \cos(B) &= \frac{1}{2} [\cos(A+B) + \cos(A-B)], \text{ obtaining} \\ &= A\alpha(t) p\left(\frac{\tau - \tau_d(t)}{T_p}\right) \text{LPF} (\cos(4\pi f_c \tau - 2\pi f_c \tau_d(t)) + \cos(-2\pi f_c \tau_d(t))) \\ &= A\alpha(t) p\left(\frac{\tau - \tau_d(t)}{T_p}\right) \cos(-2\pi f_c \tau_d(t)) \end{aligned}$$

Parallely, the Q branch result of the demodulator can be calculated knowing

$$\begin{aligned} \sin(A) \cos(B) &= \frac{1}{2} [\sin(A+B) + \sin(A-B)], \text{ obtaining} \\ &= Aj\alpha(t) p\left(\frac{\tau - \tau_d(t)}{T_p}\right) \text{LPF} (\sin(4\pi f_c \tau - 2\pi f_c \tau_d(t)) + \sin(+2\pi f_c \tau_d(t))) \\ &= Aj\alpha(t) p\left(\frac{\tau - \tau_d(t)}{T_p}\right) \sin(2\pi f_c \tau_d(t)). \end{aligned}$$

Thus adding the results from the IQ branches, the result is,

$$\begin{aligned} y_h(\tau, t) &= A\alpha(t) p\left(\frac{\tau - \tau_d(t)}{T_p}\right) [\cos(2\pi f_c \tau_d(t)) + j \sin(2\pi f_c \tau_d(t))] \\ y_h(\tau, t) &= A\alpha(t) p\left(\frac{\tau - \tau_d(t)}{T_p}\right) \exp(j2\pi f_c \tau_d(t)) \end{aligned} \tag{2.4}$$

Therefore, the Doppler shift introduced by the breathing can be extracted looking at the phase  $\phi(t) = 2\pi f_c \tau_d(t)$

$$f_d(t) = \frac{1}{2\pi} \frac{\delta\phi(t)}{\delta t} = \frac{\delta\left(2\pi f_c \frac{2d(t)}{c}\right)}{\delta t} = \frac{4\pi}{\lambda} m_b \cos(2\pi f_b t) \tag{2.5}$$

It can be observed how the Doppler frequency will oscillate in time with the breathing frequency.

### 2.1.3. MODEL OF BREATHING HUMAN VERIFICATION

In order to verify this model, a comparison is made between a simulation of a breathing measurement, and a breathing measurement captured with a monostatic receiver.

For the comparison, a spectrogram of the signal is computed to observe the frequency and phase content of the  $y_h(\tau, t)$  signal as they change over time due to the breathing motion. For this, a Short-Time Fourier Transform (STFT) is computed over small time windows of the signal, revealing the Fourier spectrum on each short segment. Given the

fact that a human breathing cycle is about 1.5 - 6 seconds, to compute the spectrogram, a time window of 0.2 seconds is used, with an overlap of 50%. This should allow the sampling of various points in the breathing cycle. The spectrogram of a breathing motion is plotted in Figures 2.4 for both a breathing measurement at the range bin  $d(t)$  of interest (left), and a simulated measurement with similar breathing frequency  $f_b = 0.36\text{Hz}$  and chest displacement  $m_b = 5\text{mm}$  (right). The periodic shift in frequency can be observed through time, together with a shift in amplitude, as has been described in the derived model.

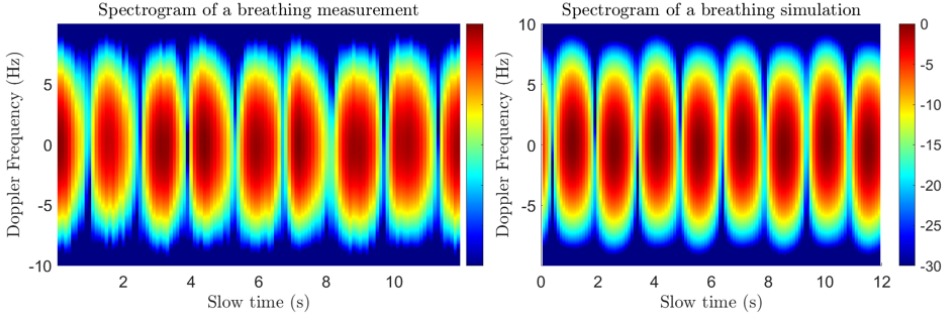


Figure 2.4: Spectrogram comparison of a measured breathing motion (left) and a simulated breathing motion (right)

The periodic Doppler frequency changes associated to breathing as described in Equation 2.5 can be observed in a slight displacement in the Doppler frequency over time. The maximum Doppler frequency, in this case, 0.2Hz, will be associated to the maximum chest movement parameter  $m_b$  as defined in Equation 2.6

$$f_{dmax} = \max \frac{2d(t)f_c}{c} = \frac{2 \max d(t)f_c}{c} = \frac{2m_b}{\lambda} \quad (2.6)$$

Note that there is no ground-truth for this experiment. The purpose of the comparison is to make a qualitative assessment of the model that returns virtually similar results in reasonably defined ranges. The comparison meets this purpose and, therefore, this model is considered to accurately represent the properties of the breathing motion as seen from the radar and its properties are used to define the detector of vital signs.

#### 2.1.4. CONCLUSIONS ON VITAL SIGNS EXTRACTION

After this initial study of the structure of the breathing data, a detector can be built to identify vital signs versus other movements or noise. The main features that can be used to extract breathing frequency are the phase  $\phi(t)$  and the amplitude  $\alpha(t)$  as was defined in Equation 2.4.

By extracting the phase of the signal, the oscillation due to breathing can be observed as the fluctuation of Doppler Frequency over time (see Equation 2.5). The phase can be

extracted by performing

$$\phi(t) = \arctan\left(\frac{Q(t)}{I(t)}\right) \quad (2.7)$$

However, due to the range of this function, the phase is limited to  $[-\pi, \pi]$ , causing continuity errors. An example of such problems can be seen in Figure 2.5.

2

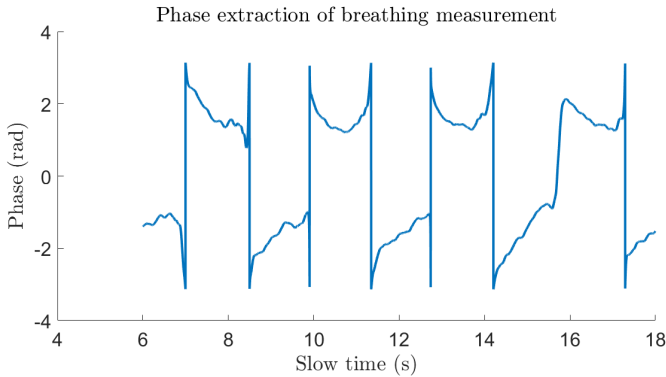


Figure 2.5: Phase profile of a breathing measurement to showcase the difficulty of phase-extraction.

The differentiate and cross multiply algorithm was tested to correct this in [1], but it was concluded that in noisy environments, this algorithm does not perform properly and phase cannot be easily extracted. Therefore, for this thesis, the periodical amplitude shift defined in Equation 2.4 will be used instead to extract the breathing frequency information.

## 2.2. DETECTION PROCESSING PIPELINE EXPLANATION

The the key function of the detector is to identify shifts in the signal corresponding to vital signs as defined in Equation 2.4, and to differentiate in between these and other body movements, and noise. When the human moves (stands up, swings arms, tilts,...) vital signs cannot easily be extracted due to the presence of other movements besides breathing. Therefore, the problem of vital signs detection (usually treated as a binary classification problem between a static breathing person and noise), should actually account for a third class consisting on body-movement.

A detection algorithm for the CIR data matrices is presented, the function of which is to determine the number of humans detected by a particular radar Rx, their position w.r.t. the Rx and the breathing frequencies. A schematic summary of the detection algorithm is presented in Figure 2.6.

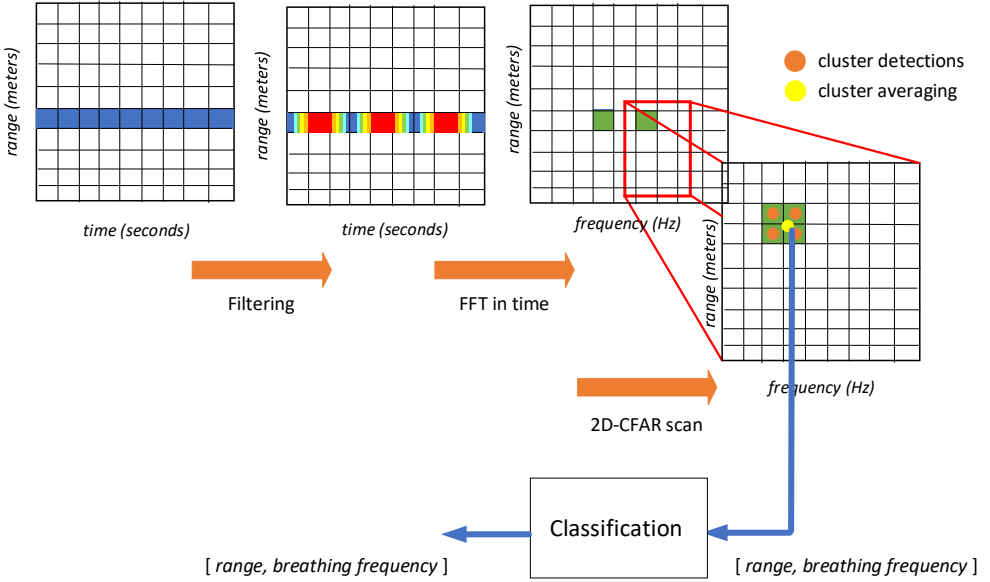


Figure 2.6: Proposed detection processing pipeline schematic. An FFT is applied on the slow-time in the CIR radar data matrix. A 2D-CFAR algorithm scans the range-frequency region of interest in the range-Doppler plot and the resulting detections are clustered and interpolated to extract range and breathing frequency information. The classification block classifies the possible detections identified and discards noise.

### 2.2.1. DATA FILTERING

Firstly, the CIR data is filtered to extract high-frequency and DC components. From the literature, we know that the human frequency range is about  $[0.1 - 0.8]$ Hz [25]. We apply a Butterworth band-pass filter of 2nd order with cutoff frequencies 0.1 Hz and 0.8 Hz along the full duration of the slow-time samples (30 seconds) to get rid of both the DC level found at 0 Hz known as static clutter, and the high-frequency components associated to noise. In Figure 2.7 a comparison is made between a received CIR radar data matrix and a filtered data matrix in which the breathing of a static human was experimentally measured. The amplitude shift in time can be clearly observed after filtering.

### 2.2.2. IDENTIFICATION OF RANGES AT WHICH HUMANS ARE PRESENT

Once the static-clutter component and the high-frequency noise have been removed, the range bins in which a possible vital-sign are present can be identified. In the literature (for example [26, 6]), usually the signal in the range-bin with highest energy is transformed into the Fourier domain to see if it shows peaks in the possible breathing range. However, this method would fail in the presence of multiple people or high-energy echos appearing at further ranges than the actual human.

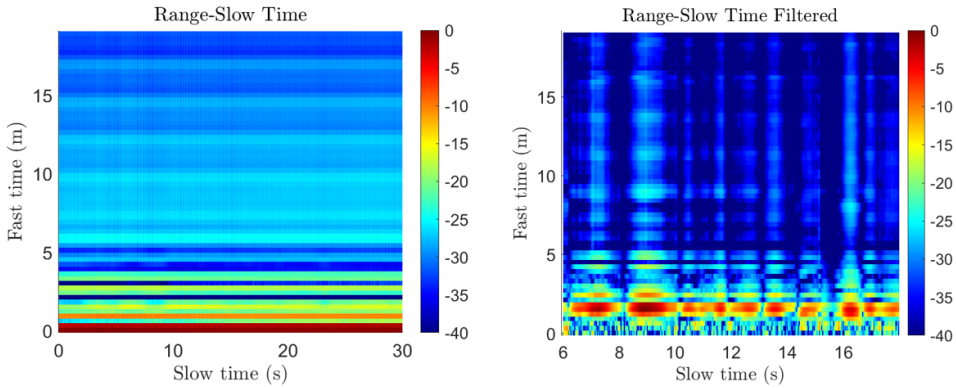


Figure 2.7: Raw CIR data of a breathing measurement (left), Filtered breathing measurement (right)

Therefore, a different approach is taken. Firstly, a Range-Doppler map is computed. To do this, a Fast Fourier Transform (FFT) is applied to all range-bins in the slow-time. In this map, high-energy peaks will appear in the range-frequency bins that correspond to the ranges in which humans are present, and the frequencies of their breathing. In order to detect these peaks, the 2D - Constant False Alarm Rate detection algorithm (2D-CFAR) is applied in the range-frequency region in which a human can be found.

CFAR is a detection procedure which uses a sliding window to estimate the parameters of the background model and thus determine if a target is present or not by adapting its detection threshold [45]. For this project, a particular type of CFAR, mean-level CFAR (ML-CFAR) is used. This variation estimates the power of the background noise based on the arithmetic mean of the neighboring range cells. Particularly, SOCA (smallest of cell averaging) CFAR is used, given that its variation, GOCA (greatest of cell averaging) has undesirable performance when 1+ targets exist in the region.

The importance of choosing an appropriate value for a probability of false alarm ( $P_{fa}$ ) with which the detection threshold is adjusted must be noted. This parameter will determine the sensitivity of the detection algorithm.

The resulting range-Doppler plot and the detections from Figure 2.7 can be observed in Figures 2.8 and 2.9 (with zoom).

As can be appreciated in the Figures above, the fact that humans can be modelled as extended targets, the energy of one human will be distributed among multiple consecutive range-bins and multiple frequency bins. In [46], the (single) highest-energy peak found by the 2D-CFAR algorithm is selected as the identified target. However, again this approach fails when multiple people are present or when high-energy multipath is present.

Therefore, a novel approach is presented, in which the 2D-CFAR detections are clustered into possible targets, and the weight-averaged range-frequency information of these clusters is classified as possible humans in the environment. The weight is estab-

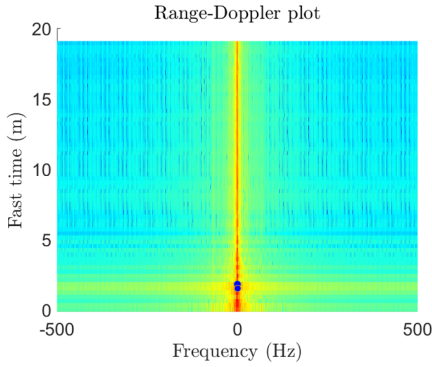


Figure 2.8: Range-Doppler map with clusters

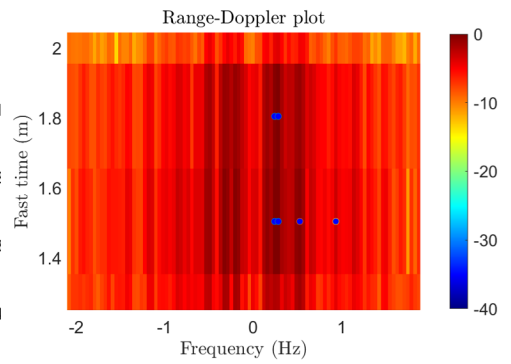


Figure 2.9: Range-Doppler map with clusters (zoom)

lished with respect to the energy of the echos in the cluster.

In Figure 2.10 the detected cells of the clusters are shown in blue. In yellow, the averaged range-frequency information extracted from each cluster.

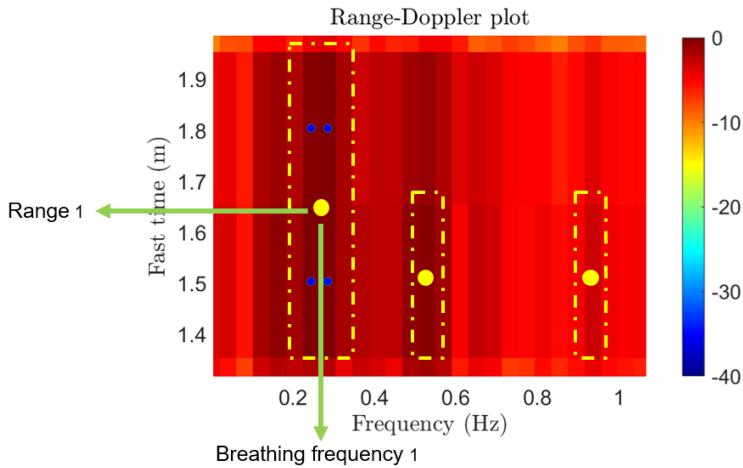


Figure 2.10: Range-Doppler map with clusters (zoom). The blue dots correspond to the identified range-frequency cells in which a human being is identified, while the yellow lines mark the edges of the identified clusters, and the yellow dots are placed in the weighted average positions for both range and breathing frequency identified.

In this case, 3 final detections are shown (3 yellow dots) each corresponding to a cluster average from which range and breathing frequency information is extracted.

### 2.2.3. CLASSIFIER TO DISCARD FALSE DETECTIONS

Finally, these identified range-bins are filtered by the classifier, which will make a final assessment of the detections identified and distribute them into 3 different classes. These have been characterized in Table 2.1.

Output	Name	Detected Human	Breathing estimation
0	Noise	No	No
1	Breathing Human	Yes	Yes
2	Moving human	Yes	No

Table 2.1: Classification Pipeline output

A summary of the processing algorithm is made on Figure 2.11. The explanation is detailed below.

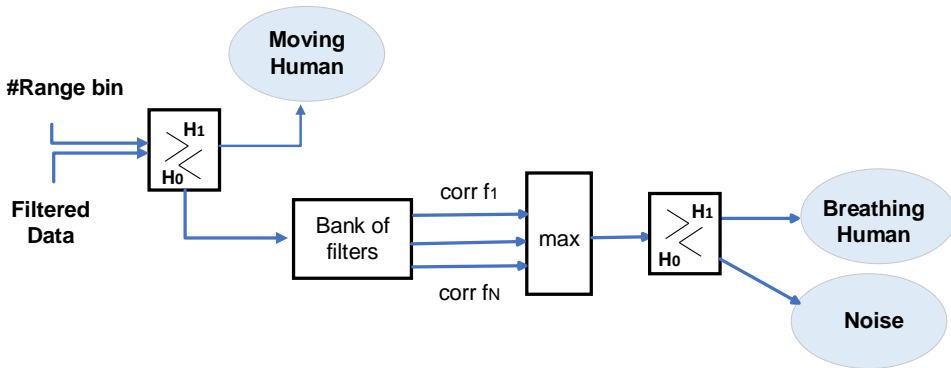


Figure 2.11: Classifier diagram. The evaluated range bin is passed through the processing pipeline, capable of differentiating if the identified signal corresponds to a moving human, to noise, or to a static human from which vital signs can be extracted.

For every range identified, firstly the detection of a possible moving human is made. Since the ranges in a cluster have been weight-averaged for more accuracy, the maximum-energy range bin in every cluster is selected for this evaluation instead.

Due to the fact that moving the chest for breathing is the largest movement that can be observed by the radar when the human is static, when it is not, the received signal will have much stronger fluctuation. Therefore, by setting up a threshold in the variation energy of the signal in slow-time in the identified ranges, a differentiation between a moving human vs a static human (or noise) can be made. This can be done empirically by observing a batch of measurements.

After this step, the classification turns again into a binary problem for static human presence detection. The detection is based on the use of a bank of sinusoids of frequencies 0.1 to 5 Hz in 0.05Hz steps. Each of these sinusoids is correlated with the amplitude of the signals in the identified ranges and the maximum level of correlation is found for each sinusoid. For a measurement with a given frequency  $f_b$  this will result in the clear appearance of a peak in the  $f_b$  frequency as seen in Figure 2.12 (right). However, for a noisy measurement which has falsely been identified by the 2D-CFAR algorithm, the peak distribution will not be consistent as seen in Figure 2.12 (left)

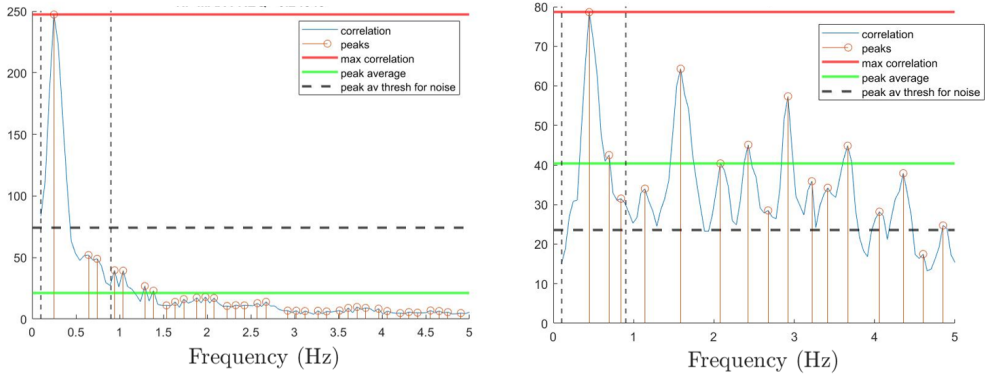


Figure 2.12: Correlation of breathing signal (left) being correctly classified as a breathing motion, and correlation of a noise signal (right), being correctly classified as noise.

In order to differentiate in between the two cases, the following criteria is established. Firstly, the maximum peak should fall within the defined human breathing range marked in the figures by the vertical lines at 0.1 and 0.8 Hz. Secondly, the average peak power should be below a certain threshold. The value of this threshold is determined by a percentage of the maximum correlation peak's value. If both these conditions apply, the signal is classified as a human. If not, it is classified as noise and discarded as a false alarm.

It must be noted that this classifier, which serves the purpose of discarding noise and identifying measurement of moving human targets, has not been demonstrated in this project. That is, the focus of this thesis is not centered on the evaluation of the classifier, and no experimental tests have been conducted with moving people due to lack of time. However, particularly for the case for moving people, it would be interesting to observe the performance of the association block when the breathing frequency information cannot be used as an input to the fusion algorithm. This is commented in the Future Work section in Chapter 5.

### 2.2.4. OUTPUT OF DETECTOR

Hence, the final output of the detector for a particular receiver  $m$  is the so-called detection matrix  $\mathbf{D}_m$ . It contains the range and estimated breathing frequency information  $[r_{m,n}, f_{b,m,n}]$  of the  $N_m$  detected targets for each of the  $M$  receivers as defined in Equa-

tion 2.8.

$$\mathbf{D}_m = \begin{bmatrix} (r_{m,1}, f_{b,m,1}) \\ (r_{m,1}, f_{b,m,2}) \\ \dots \\ (r_{m,N_m}, f_{b,m,N_m}) \end{bmatrix} \quad (2.8)$$

In this section, a novel processing pipeline for human detection has been presented. This detection block will be used to individually evaluate the received data from the multiple Rx in the network.

The detection is based on the experimentally-validated model developed for the radar signature of the breathing motion.

Firstly the radar data is filtered, and a 2D-CFAR algorithm is applied to a range-Doppler plot to identify the possible range and breathing frequency of humans as detected by the radar. The detections are clustered and a weight-average value for range and breathing frequency is provided for each cluster.

Finally, these detections are put through a classifier, which is capable of distinguishing 3 different classes, namely a moving target, the breathing frequency of which cannot be estimated, a static target, and a noise measurement, falsely detected by the 2D-CFAR algorithm. Noise measurements are discarded, and for moving targets, the previously identified breathing frequencies of the detections are discarded.

The final output of the detector is thus the detection matrix  $D_m$  for  $1 < m < M$  where  $M$  is the number of radar receivers.

## 2.3. DATA ASSOCIATION

After the data from the radars has individually been processed, a detection matrix  $\mathbf{D}_m$  is obtained from each of the  $M$  receivers as seen in Equation 2.8. This matrix contains the range and breathing frequency of the detected targets.

A processing block is needed to associate the different detections from the  $\mathbf{D}_m$  matrices into possible humans, and thus perform human localization.

### 2.3.1. ASSOCIATION HYPOTHESIS

For multiple people in the environment, the independent detections corresponding to different targets in the environment must be associated correctly for each receiver, otherwise, ghost targets will appear in the localization. The ghost target is defined by the combination of ranges that corresponds to the intersection of ranges from different targets. [47]. A schematic can be seen on Figure 2.13 for a correct range association. In red, a ghost target is shown as the combination of ranges among receivers which correspond to different targets.

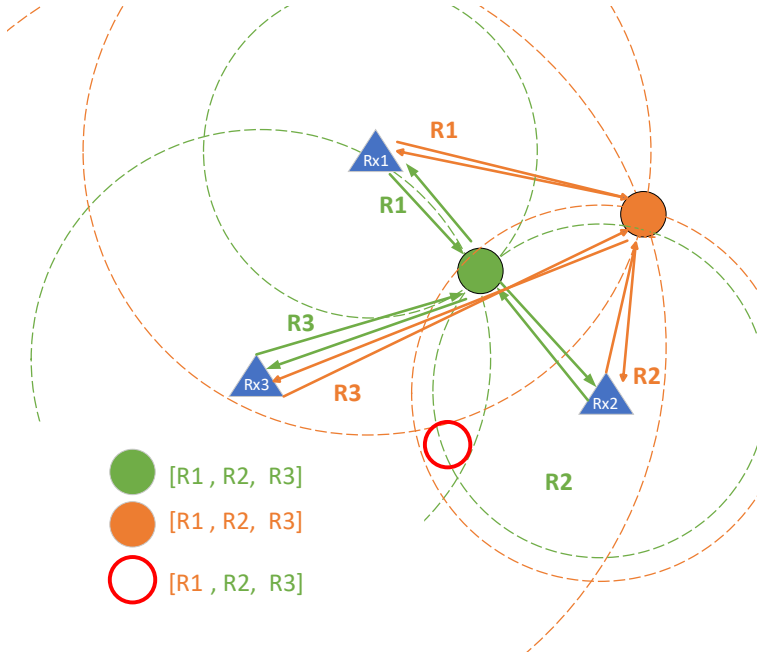


Figure 2.13: Visual explanation of the appearances of ghost targets. If detected ranges from the green target are associated with detected ranges from the orange target from a different radar Rx, a new false target is generated where those range-combinations cross. In this case, The red circle is a ghost target.

The number  $C$  of combinations in between the  $N_{D,n}$  detections for  $N_{Radars}$  can be expressed as seen in Equation 2.9

$$C = \prod_{n=1}^{N_{Radars}} (N_{D,n} + 1) \quad (2.9)$$

where  $N_{Radars}$  is the number of radar receivers used and  $N_{D,n}$  is the number of detections obtained in each radar. Moreover, for each radar, we evaluate the hypothesis for a missed detection.

An association algorithm is used to evaluate the  $C$  possible detection combinations in between radars. In [48] all hypothesis are evaluated by combining the range information from the detections, and a cost is established for for each of the  $C$  possible combinations. In [49] a similar solution is presented, but includes also the combination of breathing frequencies to compute the cost for each hypothesis.

In this project, an association algorithm was developed based on both [48] and [49] which uses both the range and breathing frequency estimation to properly localize the detected targets in our environment.

C hypothesis should be evaluated. An association cost is calculated for each of the hypothesis, and stored in a cost matrix  $\mathbf{C}$ . Each cost contained in the matrix is calculated based on the likelihood that a given hypothesis corresponds to a real target.

A particular hypothesis cost can be defined as the summation of 3 costs: the cost given by localization, the cost given by the breathing frequency, and the cost given by the number of radars considered for the hypothesis. The following sub-section describes the details of the proposed association algorithm.

### 2.3.2. ASSOCIATION ALGORITHM

- Firstly, the cost given by localization is defined. This cost is computed by estimating the error in localization  $d_{pos,m}$ . To compute this error, a position estimate needs to be found. Initially a range vector consisting on the  $N_{Radars}$  ranges that form the hypothesis is defined.

$$\mathbf{r}_m = [r_{1,m}, r_{2,m}, r_{3,m}, r_{4,m}] \quad (2.10)$$

For a given vector  $\mathbf{r}_m$ , a localization algorithm is applied to find the position estimate  $\hat{\mathbf{p}}_m$  corresponding to these ranges. Usually, algorithms such as multilateration (MLAT) are used. By solving the coordinate unknowns in a determined number of equations, accurate positioning can be found. Also, techniques such as LS [50] can be applied to fuse the ranging information from the various receivers. The problem usually comes from the computational complexity of such algorithms and the high sensitivity to errors in the measurements.

To solve this, [51] proposes an alternative approach in which the 3D space is divided into cells as in [52, 53]. In each cell, a vector  $\mathbf{d}_c$  containing the distances from that cell to all Tx-Rx radar combinations is computed and stored. This can be seen in Figure 2.14.

Using the machine learning method of  $k$ -Nearest Neighbor ( $k$ -NN), all  $\mathbf{d}_c$  vectors are compared to the vector  $\mathbf{r}_m$  made of detections from the radars in a particular hypothesis.

The  $k$ -NN is a non-parametric, supervised learning classifier, which uses proximity to make classifications or predictions about the grouping of an individual data point. In this context, it is applied to determine the cell which contains the range vector  $\mathbf{d}_c$  that most resembles that of the actual target detections  $\mathbf{r}_m$ , thus identifying the estimated position of the target  $\hat{\mathbf{p}}_m$ .

After computing  $\hat{\mathbf{p}}_m$ , the estimated range vector  $\hat{\mathbf{r}}_m$  is re-computed with the distances from  $\hat{\mathbf{p}}_m$  to the radars. Finally, the distance error is computed as :

$$d_{pos,m} = |\mathbf{r}_m - \hat{\mathbf{r}}_m| = |\mathbf{r}_m - distances(\hat{\mathbf{p}}_m)| \quad (2.11)$$

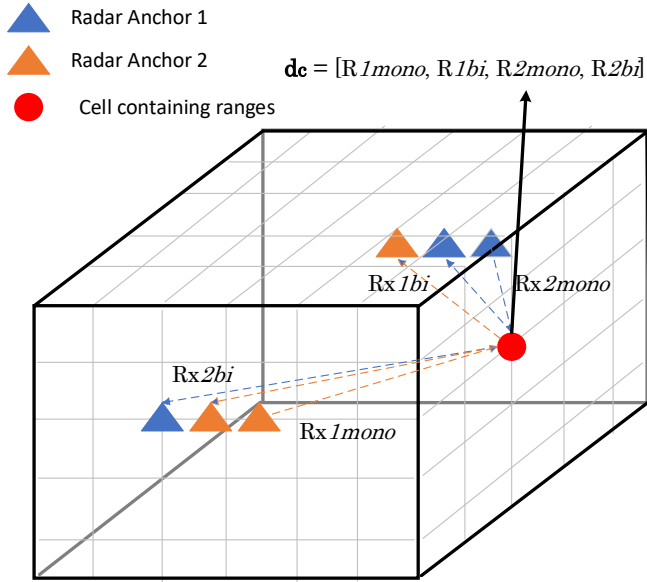


Figure 2.14: 3D grid with a schematic representation of the various  $d_c$  vectors containing the ranges to the Tx-Rx combinations.

Note: This particular radar setup mirrors the proposed radar-network positioning defined later in Chapter 3

- Secondly, the error in breathing frequency is defined. This is based on how much the detected breathing frequencies in the hypothesis resemble each other as

$$d_{Breath,m} = \sum_{n=1}^{N_{Radars}} f_{b,m,n} - \text{mean}(\mathbf{f}_{b,m}) \quad (2.12)$$

Where  $\mathbf{f}_{b,m}$  is the vector containing the breathing frequencies of the hypothesis.

- Finally, a cost is defined to account for missed detections in the hypothesis. If we rely on complete detection from the detection block, it can be established that a hypothesis which considers a missed detection from a radar will have a higher cost than a hypothesis which considers a full combination of detections. This cost can be computed as seen in [48]

$$d_{miss,m} = \log_{10} \left( \left( \frac{P_d}{P_{fa}} \right)^{N_{miss,m}} \right) \quad (2.13)$$

where  $N_{miss,m}$  is the number of missed detections accounted for in a particular hypothesis.

Therefore, the final computation of the cost matrix can be expressed as seen in Equation 2.14.

$$C(m) = d_{Pos,m} + d_{Breath,m} + d_{miss,m} \quad (2.14)$$

To identify the minimum cost hypothesis, an assigning function based on Lagrangian relaxation is used to solve the problem.

The output of the association algorithm is therefore the different combinations of rows in the detection-matrices between radar receivers that correspond to identified targets in the environment.

### 2.3.3. LOCALIZATION OF ASSOCIATED TARGETS

Finally, one last step of localization is applied.

In the computation of the cost matrix  $\mathbf{C}$ , the machine learning algorithm of  $k - NN$  is used to identify the position estimate for a given hypothesis  $\hat{\mathbf{p}}_m$ . For this final localization step, the process is repeated for the identified hypothesis in the output of the association algorithm.

Therefore, the localization accuracy highly depends on the performance of the  $k - NN$  method to both compute the cost matrix that allows the proper identification of the true hypothesis, and the final position estimation for the identified targets.

Moreover, accounting for the fact that ghost targets may appear as a result of incorrect associations, a 'Probability of target' is defined. Assuming that ghost targets result from missed detections and false alarms in the previously defined algorithm block, and that the defined association algorithm can account for these, some associated targets can be assigned a higher probability. That is, some associated targets will contain no missed detections (or false alarms) from any Rx, and others may contain a few. By observing the amount of miss-detections that the associated targets contain, it can be defined that those with more miss-detection considerations are more likely to be ghost targets. For result evaluation, a threshold can be defined to determine that low-probability targets need not be considered.

### 2.3.4. KNOWN LIMITATIONS OF THE DEFINED ASSOCIATION ALGORITHM

The developed approach, even if computationally inexpensive and effective, is also known to have some pitfalls.

Firstly, it is highly dependant on the detector output being accurate. Meaning that even if some false alarms can be discarded and missed detections can be overcome, accuracy loss in the input detection matrix, or the introduction of high numbers of errors may highly impact localization and the computation of the cost matrix.

Secondly, increasing the input number of detections will quickly increase the computational complexity of the algorithm due to the added number of hypothesis that need evaluation, making it unfit for real time applications.

Finally, note that even if the breathing frequency information and the number of radars are used to compute the cost matrix, there is a high dependency of the algorithm performance on the accuracy of the localization algorithm, both in the computation of the range error for the cost matrix, and on the final positioning step of the identified association of detections.

When the association and thus localization processes are correct, the accuracy directly depends on the resolution of the grid that is defined. Defining a finer grid, however, will increase computational complexity and human-occupancy might be distributed amongst neighboring grid-points. Moreover, the radar range accuracy, even if it can be improved with the cluster-averaging technique, will be of a few centimeters, and finer grid definitions might be inefficient. For this, a resolution of 5-10cm is used for the grid computation. This value has been proven to be computationally inexpensive while providing good accuracy results.

The number of radar receivers used for the detection is also a critical factor on the accuracy obtained. Because a 3D space is defined, a minimum of 4 radars must be used to find the region where the spheres intersect. However, because the sphere intersections that fall outside the defined grid are discarded, localization can be possible with less radars. This means that when missed-detections are considered, localization with accuracy is possible, but it deteriorates as the number of ranges used for localization decreases.

## 2.4. CONCLUSIONS ON THE PROPOSED ALGORITHMS FOR MULTIPLE PEOPLE DETECTION AND LOCALIZATION

In this Chapter, an initial detection block is defined, in which vital signs detections for multiple people are performed based on the study of the proposed model for human breathing radar signature. A novel approach to detect vital signs and to extract ranging information with improved accuracy is put forward.

Also, a newly defined association block is presented, in which the detections from various receivers can be combined in order to obtain localization of the detected humans in the environment. The information of range and breathing frequency previously identified can be used to compute an association cost, and thus determine the correct hypothesis.

The limitations of this association algorithm identified have also been detailed.

# 3

## MULTISTATIC RADAR NETWORK DESIGN AND SIMULATION

*In this chapter, the design and construction of a multistatic UWB radar network based on NXP's Ranger 4 boards is discussed.*

*Moreover, the hardware complexity of the setup and its limitations in terms of stability, make it difficult to obtain constant batches of measurements, especially in complex environments as is the inside of a vehicle. In order to evaluate the performance of the algorithm in a generalized way, a simulation for CIR radar data is also developed and presented in this chapter.*

### 3.1. MULTISATIC UWB NETWORK

In this section, the design specifications and methodology for the construction of a multistatic UWB network using NXP's Ranger4 boards is specified. At the beginning of this thesis, the capturing application for the Ranger4, which had previously been developed by NXP, was modified to support multiple-board configuration and simultaneous data-capturing.

A final study is made on the expected performance and known limitations of the setup.

#### 3.1.1. DEFINITION OF THE HARDWARE

The boards used for the experiments are chosen to be NXP's UWB IC: NCJ29D5, called Ranger4 [54]. The specifications of Ranger4 can be seen on Table 3.1

These boards have been programmed to perform monostatic radar measurements. In order to take said measurements, the board is connected to a computer via an FTDI cable as specified in the User Manual for the evaluation boards [55]. A command interface is provided over SPI to enable communication between the NCJ29D5-Radar device and an external host such as a microcontroller or a PC. When used in a PC as a host, the board can take measurements using the *NCJ29D5\_RadarConnect\_App* application.

Parameter	Available range
Radar type	Pulsed radar
Center frequency	6.4-8 GHz
Transmitted power	-12dBm - +14dBm
Bandwidth	500MHz
Operation	[Transceiver, Tx, Rx]
PRI	0.001 - 1 s
Code	[0-11]

Table 3.1: UWB Ranger4 parameters ([55])

An image of the board can be seen in Figure 3.1

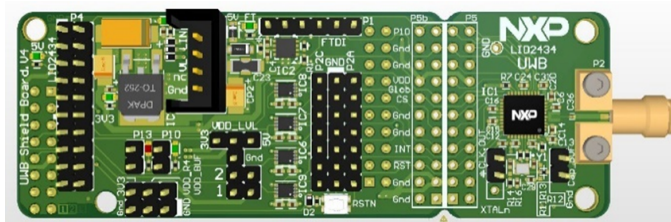


Figure 3.1: Ranger4 UWB IC: NCJ29D5 [54]

The antennas used are the Decawave Spline antennas [56], which are omnidirectional antennas with an operational frequency range of 3 to 8 GHz.

Ranger 4 has been designed for secure car accessing via smartphone. When it comes to radar applications such as vital signs detection, the chosen IC presents an evident downfall, which is that it offers a single SMA connection for an antenna. This translates into high losses due to coupling between transmitter (Tx) and receiver (Rx) and a great loss in the sensitivity of the Rx. In order to solve this, NXP is currently working on the development of Ranger5, which will include a separation between Tx and Rx, and present a boost in the sensitivity. However, the new boards will not be available at the time of the thesis work.

### 3.1.2. DUAL-BOARD SYSTEM

In order to emulate Ranger5's performance, the functions of Tx and Rx can be distributed among various Ranger4 boards. In order to do this, two boards are needed, in which one (Tx) will act as Master, and the second (Rx) will act as a Slave.

Besides the necessary re-programming of the boards for the dual functionality, some hardware modifications are necessary on the Slave board. Particularly, the crystal is removed, and its pin is connected to the Master board clock directly, as specified in the

Dual Board User Manual [57]. The trigger pins of both boards are also connected, so when the master sends the trigger, both boards will start transmitting and receiving at the same time.

Once the hardware modifications are made, and the two boards are connected to the PC via the FTDI wires, two instances of the *NCJ29D5\_RadarConnect\_App* application can be called, each specifying the allocated Port number and the correct configuration of each board. That is: the Master will operate in Tx-Rx mode, and the Slave on Rx mode only. This way, a distributed monostatic system can be created, ensuring separation between antennas and decreasing coupling. For reference, a picture of such setup can be observed in Figure 3.2 and the sensitivity increase observed in the Rx of this dual-board system with respect to the single transceiver board can be appreciated in Figure 3.3, where an experimental breathing motion is recorded. The increase in sensitivity is about 10 dB.

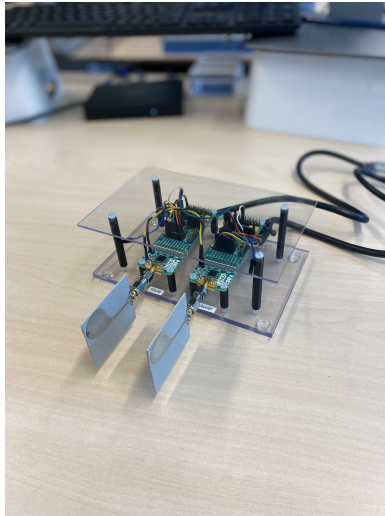


Figure 3.2: Dual Board setup. The Tx and Rx boards have been separated to increase Rx sensitivity.

### 3.1.3. MULTISTATIC RADAR NETWORK: STEPS FOR SETUP CONSTRUCTION AND VALIDATION

As it was defined in Chapter 1, one of the goals of this project is to evaluate the information that can be obtained from the environment with a multistatic radar network. Therefore, once it is tested that the functionalities of Tx and Rx can be distributed amongst boards, and that synchronizing various Rx boards to a Tx is possible, a multistatic radar network is built.

#### 1. MONOSTATIC AND BISTATIC RADAR

In monostatic radar, the transmitter and receiver antennas and boards are co-located, whereas in bistatic operation, the receiver antenna/ boards are placed in distances com-

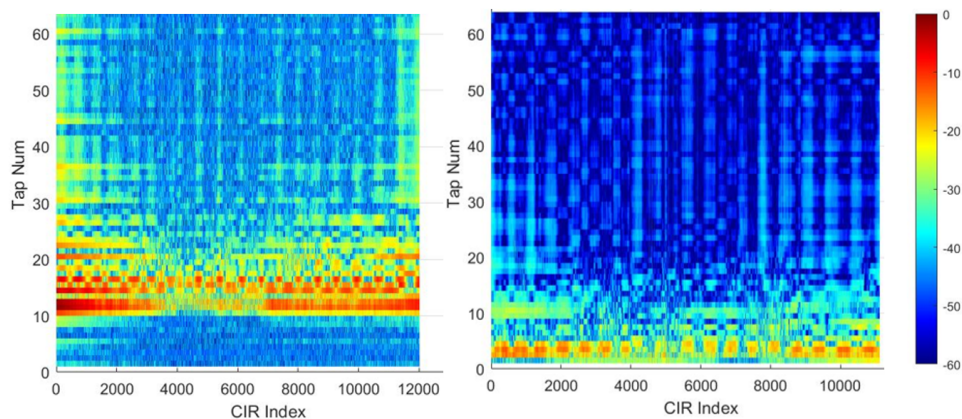


Figure 3.3: Transceiver measurement of a breathing motion (left) and distributed monostatic board measurement of the same breathing motion (right). A sensitivity improvement can be appreciated as a result of the antenna separation.

parable to the distance of the targets. A schematic definition of monostatic and bistatic radar can be seen in Figure 3.4

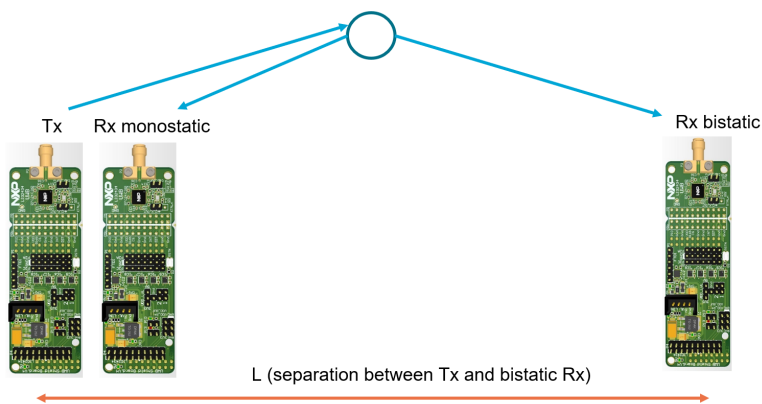


Figure 3.4: Monostatic and Bistatic radar setup

By distributing various Rx boards for a single Tx, both monostatic radar and bistatic radar can be built using Ranger 4 boards. The separation of antennas in bistatic radar should provide an increase of sensitivity as seen in Figure 3.3, and also a gain attributed to the different angles at which the targets are observed.

Several design aspects for the radar network are evaluated in the rest of this section, as the design of the multistatic UWB radar network can be optimized from various points of view.

## 2. ANCHOR STRUCTURE

Firstly, the structure of one anchor is defined. A 3-board setup is made in which a Tx is connected to 2 Rx boards, making a total of 3 boards/ anchor. The Rx boards are placed both close to the Tx, emulating monostatic operation, and far from the Tx, for bistatic operation. Figure 3.4 represents the structure of one anchor.

Each anchor in the system will operate independently from other anchors, that is, the addition of more anchors in the system should be transparent to existing anchors.

## 3. ANCHOR PLACEMENT

The position of the boards is defined. The system will consist of 2 anchors, essentially the minimum number to have bistatic pairs of transmitters and receivers in the considered setup.

In order to observe the breathing motion, the radars should be placed where the maximum displacement of the chest happens in line of sight of the radar (LoS), not orthogonal to it. Given the fact that the environment is a vehicle, it can be assumed that humans will be sitting down in the designated positions. Placing a radar Tx on the side of the car might not be optimal, as hinted in [8]. Therefore, it is decided that radars should observe the targets from the front or back preferably.

One of the Tx will be placed in the rear mirror of the car, where the displacement due to breathing can be detected. Moreover, since an important use-case is CPD, the Tx of the second anchor should observe the environment from the top of the back-seat. This would allow to observe the breathing motion of babies placed in crates, plus provide another illumination point of view in which the back-targets might be localized more easily. As for the receivers, Rx boards operating monostatically will be placed next to their respective Tx, together with an Rx board operating bistatically. A schematic of the defined anchor placement is shown in Figure 3.5.

This particular board placement where monostatic and bistatic boards from separate anchors are placed in proximity both in the rear-mirror of the car and over the back-seat, allows future deployment of 2 Ranger5 boards, which would substitute the current 6-board Ranger4 setup. In each of the Ranger5 boards, the Tx, monostatic Rx, and bistatic Rx from a different Tx could be encapsulated.

## 4. DATA MULTIPLEXING BETWEEN ANCHORS

In order to ensure that both anchors operate independently from each other, several multiplexing methods can be defined.

Initially, Code-Division Multiple Access (CDMA) was attempted. However, it was concluded that the bistatic Rx boards, placed in closeness to the opposite Tx, were adjusting their sensitivity levels to those transmitters, thus, after on-chip decoding, only the code-interference could be observed in the CIR data. In Annex B, a detailed explanation is given for the tests performed on CDMA and the conclusions extracted.

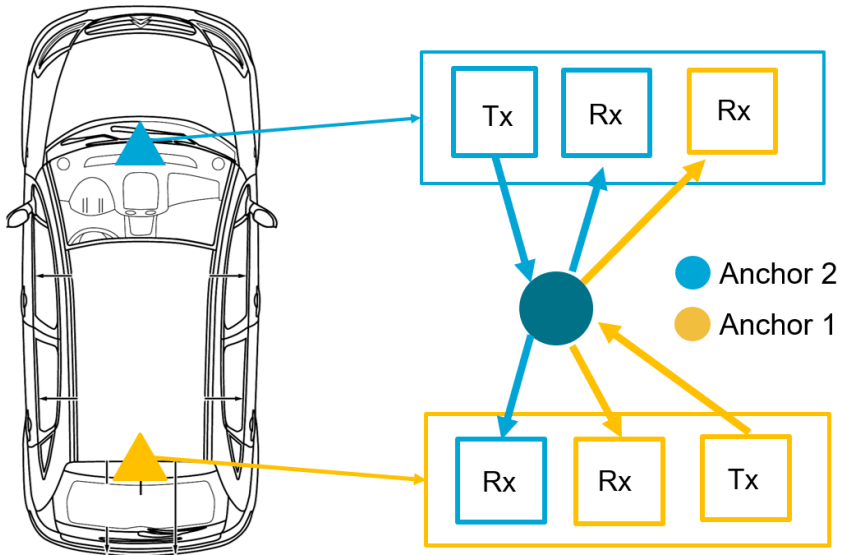


Figure 3.5: Anchor placement in car. 2 anchors, each consisting of a transmitter, a monostatic receiver and a bistatic receiver are placed inside the car in 2 different positions. One is the rear mirror of the car, and the second is the ceiling of the back-seats.

Time- Division Multiple Access (TDMA) requires synchronization in between the defined anchors. However, since each anchor runs its activation steps independently (see annex), a multi-threaded operation would need to be defined in order to make sure the streaming is time-synchronized with the defined parameters. Also in Annex B, a detailed explanation is given for the tests performed on TDMA and the conclusions extracted.

Finally, Frequency-Division Multiple Access (FDMA) is chosen. In this context, each anchor operates at different center frequency  $f_c$ , and a band gap is left in between the 2 frequencies. In order to follow standard operation, the chosen  $f_c$  for both anchors are 6.5GHz and 7.5GHz. With 500MHz bandwidth, the band-gap is of another 500MHz in between them, ensuring that there will be no interference while at the same time having a comparable scattering behaviour at the two frequencies considered.

It was found that FDMA properly satisfies the separation between the two anchors in the network. Finally, also in Annex B, a detailed explanation is given for the tests performed on FDMA and the conclusions extracted.

Thus, the chosen multiplexing system for the different anchors is FDMA.

### 5. HARDWARE REQUIREMENTS AND BOARD MODIFICATIONS

All 6 boards must be clock-synchronized. In order to distribute the clock signal over long distances, and to do it for multiple boards, the crystals of all 6 operating boards are removed, and a 7th board is used as a master clock. The master-clock signal is amplified and sent through a splitter, which sends the in-phase clock signal to 4 boards synchronously. The remaining 2 boards are clock-synchronized by connecting their clock inputs to the clock outputs of the nearest boards which receive a clock signal from the splitter. All 6 clock signals reach the respective boards completely in-phase.

Moreover, in order to ensure that all boards start their CIR stream capturing at the same time, a trigger signal is needed. To implement this, one of the boards is defined as the Master, which sends the trigger signal to all other boards via a wired connection. This allows for a synchronized start of the data capturing between all 6 radar boards. Otherwise, the Rx boards would start their operation asynchronously from the Tx boards and echos would not be received. In Figure 3.6, a schematic of the clock and trigger distribution over the boards can be seen.

It should be noted that a rigorous characterization of the clock distribution circuit and its hardware components go beyond the scope of this thesis, with main focus on the algorithm development and testing for which the setup was nevertheless necessary.

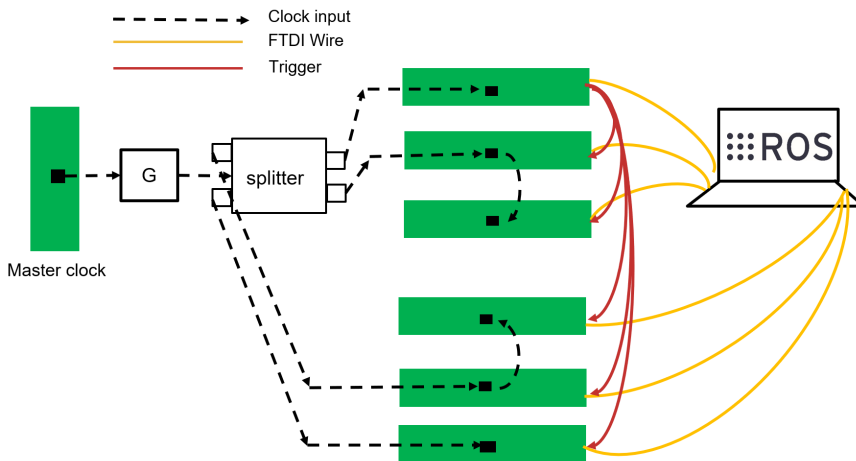


Figure 3.6: Clock and trigger distribution schematic

### 6. DATA CAPTURING ARCHITECTURE

In order to synchronize the operation of the network, Robot Operating System (ROS) is used. This software allows to create nodes, which are programs that can run specific operations in a robotics application. For our purpose, a node is defined as an application capable of initializing the boards in the anchor, configuring them with their designated Tx or Rx functionalities,  $f_c$  and codes, and to send a trigger signal that starts a synchronized data streaming of the boards.

The application is built in nodes which define the operation of 1 anchor. Therefore, by initializing two nodes, each with its configuration parameters, the 2 anchors can be started synchronously and without interference.

A detailed block-diagram of the developed ROS application has been made and is attached in Annex A.

### 7. FINAL DESIGN SUMMARY

In Table 3.2, the final design specifications are summarized, with the schematic figure given previously on Figure 3.5. The transmission code used for all boards is 0 [55].

Board	Anchor	$f_c$ (GHz)	Operation	Definition	Position
1	1	6.5	Tx	Tx 1	Back seat
2	1	6.5	Rx	Rx 1 (monostatic)	Back seat
3	1	6.5	Rx	Rx 1 (bistatic)	Rear mirror
4	2	7.5	Tx	Tx 1	Rear mirror
5	2	7.5	Rx	Rx 1 (monostatic)	Rear mirror
6	2	7.5	Rx	Rx 1 (bistatic)	Back seat

Table 3.2: Final definition of board design, anchor structure and multiplexing method

#### 3.1.4. RANGE CALIBRATION WITH THE CURRENT SETUP

For monostatic radars, the range at which a target is found can be derived from the expression  $R = \frac{\tau c}{2}$  where  $\tau$  is the total round-trip delay of the transmitted echo in seconds (TDOA) and  $c$  is the speed of light. However, a bistatic Rx board in this setup will observe the human at  $R_h = R_{Th} + R_{Rh} - L = \tau c$ , where  $L$  is the distance between the transmitter and the receiver and  $R_{Th}$  and  $R_{Rh}$  are the distances from the human to the transmitter and receiver respectively. This has also been discussed in [58].

This effect happens because the bistatic Rx will consider the 1st echo received from the Tx as a reference to start receiving echos. In monostatic operation, this distance can be approximated to zero, as the Tx and the Rx boards are very close to each other, therefore,  $R_h = R_{Th} + R_{Rh} = \tau c$ .

However, in bistatic radar,  $L$  is non-negligible, thus the radar will start recording data after the echo has already travelled a distance of  $L$  to reach the Rx board in LoS. Therefore, it is essential that the position of the boards is known, in order to properly compensate for this offset in the computation of the ranges. This can be a reasonable assumption in a practical development in vehicles, where the baseline distance between anchors can be measured a priori.

In order to test this, an experiment was made with two boards. One board was given the functionality of Tx and the other of Rx. A 5m wire and a 2m wire connected the boards simultaneously to simulate  $R_{Th} + R_{Rh}$  for the 5m wire, and the LoS distance  $L$  for the 2m wire.

It could be observed how the TDOA was of the resulting  $\tau = \frac{R}{c}$  in which  $R_h = R_{Th} + R_{Rh} - L = 3m$ , as can be seen in Figure 3.7.

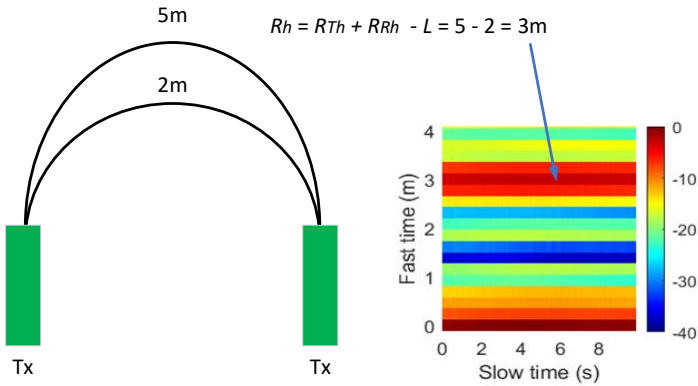


Figure 3.7: Test with boards to properly observe range offset in the Rx boards w.r.t distance  $L$ .

Therefore, in the measured CIR data, it is important to compensate for the range offset as  $\hat{R}_h = R_{Th} + R_{Rh} = (\tau c) + L$ . Knowing this, and assuming  $L$  is known, the simulations of both monostatic and bistatic radar ranges will be computed as considering this offset.

### 3.1.5. CONCLUSIONS ON CONSTRUCTION OF MULTISTATIC UWB RADAR NETWORK

A network of 6 UWB Ranger4 boards has been designed to operate synchronously in independent anchors. For this, the boards have been clock-synchronized and trigger synchronized. In this network, 2 anchors are defined to operate independently. 1 anchor can be defined as a group of 3 boards, namely a Tx board, a monostatic Rx board and a bistatic Rx board, as can be seen in Figure 3.4. The anchors are placed both in the rear mirror of the car, and in the ceiling of the back-seat. and the transmissions from the different boards are multiplexed using FDMA. For bistatic boards, a range-offset needs to be accounted for in the measurements to compensate for the distance between the Tx board and the Rx board. Finally, the capturing architecture is designed using ROS nodes, which allow the independent configuration and CIR streaming start of the defined anchors in different nodes.

Some limitations of this setup have been found.

Firstly, the synchronized data stream from the 6 boards is sent to the computer using FTDI cables connected to USB ports. This heavy data stream can be unstable after some time. Therefore, measurements longer than 30 seconds cannot easily be taken without one of the board's data streams being cut off, thus losing the reception of the CIR radar data mid-measurement.

If one of the 6 boards is affected by this phenomena, the measurement needs to be re-taken, in order to process the data with the developed algorithm.

### 3.2. SIMULATION OF CIR DATA

Given the amount of time that needs to be invested into building a database of experimental data from the radar network, it is preferable to develop a realistic simulation of CIR radar data obtained in a recreated environment of the car and different passenger occupancy scenarios in order to evaluate the performance of the algorithm. This will also allow to test the effect of different topologies of the radar network, which is cumbersome and not practical via experiments.

Simulations in literature focus on developing accurate physical models for breathing humans, including multiple reflections from the chest [59], however, most simulations fail to consider the multipath effect due to the presence of static objects in the environment. When dealing with detection of multiple people, it is crucial to consider false alarms caused by the multipath echos. By modelling various reflective objects in the car, together with human targets and the breathing motion caused by these, a realistic approximation of an in-vehicle environment can be achieved.

UWB radar signal reflection inside the vehicle environment can be considered to be of 3 different types, as similarly stated by [44]. The reflections from the human, the reflections from static objects and the combination of the two creating multipath components.

Following the architecture of the developed hardware setup, a CIR data matrix is simulated for each Rx in the network, considering its position w.r.t the simulated targets.

#### 3.2.1. HUMAN MODELLING

To simulate CIR data of a given radar in a known position, we firstly consider the received echos from the the human(s). These have multiple characteristics including amplitude, position, range-profile and path losses.

##### 1. DEFINITION OF AMPLITUDE FOR THE MODEL

Amplitude derived from human Radar Cross Section (RCS) can be approximated as the reflection from an ellipsoid which fluctuates in size to simulate the breathing motion of the human torso. The RCS of an ellipsoid can be expressed as seen in [60], with:

$$\Gamma_h = \frac{\pi a^2 b^2 c^2}{([a \sin(\theta) \cos(\phi)]^2 + [b \sin(\theta) \sin(\phi)]^2 + [c \cos(\theta)]^2)^2} \quad (3.1)$$

where  $[a, b, c]$  are the dimensions of the ellipse in the  $[x, y, z]$  axis, and  $\theta, \phi$  are the spherical coordinates from which the human is observed by the radar Rx. This can be seen in Figure 3.8.

In Equation 2.3 we defined the expression for the fluctuation of the amplitude for the human-breathing model as  $\alpha(t) = \Gamma - \beta \sin(2\pi f_b t)$ .  $\Gamma$  will be computed considering a human torso size of magnitude  $[a, b, c]$ , and considering  $\theta$  and  $\phi$  values corresponding to the position of the radar receiver with respect to the human. The factor  $\beta$  is the amplitude of RCS fluctuation caused by the breathing motion. The chest enhances and contracts a distance of  $m_b$  in this motion, therefore, by increasing  $[a, b, c]$  with  $\frac{m_b}{2}$

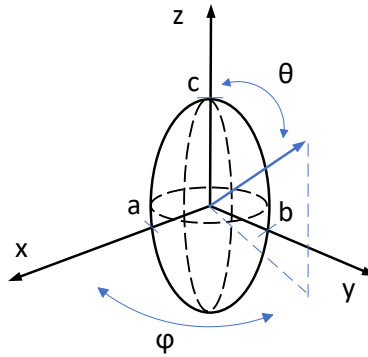


Figure 3.8: Geometry of an ellipsoid

and  $\frac{-m_b}{2}$ , we can compute the maximum and minimum RCS values to model  $\beta$  as  $\beta = \frac{\max(RCS) - \min(RCS)}{2}$ .

It is important to mention that no research has been found on how to analytically model the RCS of a ellipsoid with a bistatic radar. Therefore, for the bistatic CIR radar data matrix simulations, a monostatic assumption to calculate  $\beta$  and  $\Gamma$  will be made.

## 2. PATH LOSS CONSIDERATION

Path losses will be considered in the computation of the simulation. For this, we derive the radar range equation.

The non-directional power density transmitted by the antenna can be expressed as  $S_u = \frac{Pt}{4\pi R_{Th}^2}$  where  $Pt$  is the peak transmit power and  $R_{Th}$  is the radius of the sphere where we observe  $S_u$ . For a directional antenna with certain gain in a specific direction, we obtain  $S_g = \frac{PtG_t}{4\pi R_{Th}^2}$ . When the signal reaches the target, an echo is re-radiated towards the radar with an RCS factor  $\Gamma$  depending on the geometry, size, material, etc of the target. The reflected power at the target is  $S_r = \frac{PtG_t\Gamma}{4\pi R_{Th}^2}$  and as it travels to the receiver it is again attenuated with a factor  $\frac{1}{4\pi R_{Rh}^2}$  where  $R_{Rh}$  is the distance to the receiver. The power received by the antenna in the receiver will be dependant on the antenna efficiency  $A_{eff} = \frac{G_r\lambda^2}{4\pi}$ . The total expression for radar received power equation is thus

$$P_r = \frac{PtG_tG_r\lambda^2}{4\pi} \frac{1}{4\pi R_{Th}^2} \Gamma \frac{1}{4\pi R_{Rh}^2}. \quad (3.2)$$

The parameter  $\frac{PtG_tG_r\lambda^2}{4\pi}$  will be constant for all targets at all ranges, so it will not be considered for the simulation. Instead, the simulated received power  $Pr_h$  for the target will be modelled as the target RCS ( $\alpha(t)$ ) and the propagation losses  $PL_h$ . This can be seen

in Equation 3.3

$$Pr_h = PL_h \alpha(t) = \frac{1}{4\pi R_{Th}^2} \frac{1}{4\pi R_{Rh}^2} \alpha(t) \quad (3.3)$$

### 3. COMPUTATION OF DISTANCES

As explained in section 3.1, the separation of the Tx-Rx boards ( $L$ ) causes an offset in the received TDOA of value  $\frac{L}{c}$  seconds.

For simplicity purposes, in the simulation both monostatic and bistatic radar ranges to the target will be computed considering this effect, thus be simulated as  $R_h = R_{Th} + R_{Rh} - L = \tau c$  as the total range travelled by the echos.

### 4. HUMAN FAST-TIME PROFILE

The human body is an extended target, which means that some of the energy of the target will be leaked into neighboring range-bins. To model this effect, an adapted version of the description in [49] was used. The authors used values to generate this profile that were unaccurate w.r.t. the observed fast-time profiles in the measurements. Mainly in this Equation, the constant values were modified to broaden the human profile to more than a single peak in a given range-bin, which is consistent with a chest amplitude larger than the radar range resolution of  $\Delta R = 30cm$ . The final values were experimentally defined. This final expression can be seen in Equation 3.4,

$$h(\tau, t) = \exp(-0.55e18(\tau)^2) \cos(2\pi 1.25e8\tau) \quad (3.4)$$

where  $h(\tau, t)$  is the model of the fast time profile of the human target.

### 5. TOTAL EQUATION

The total expression for the simulation of  $N$  humans can be derived as

$$\begin{aligned} z_h(\tau, t) &= \sum_{n=1}^N PL_{h,n} \alpha_n(t) \exp(j2\pi\phi_n(t)) (h(\tau, t) * \delta(\tau - \tau_{h,n}(t))) \\ &= \sum_{n=1}^N PL_{h,n} (\Gamma_n - \beta_n \sin(2\pi f_{b,n} t)) \exp(j2\pi\phi_n(t)) h(\tau - \tau_{h,n}(t), t) \end{aligned} \quad (3.5)$$

where  $\tau_h = \frac{R_h}{c}$ , and  $\phi_n(t)$  corresponds to the phase introduced by a particular human ( $n$ ) displacement of the chest.

#### 3.2.2. PART 2: STATIC OBJECTS

In order to model a realistic scenario, static objects which cause high-energy echos should also be taken into account.

For simplicity, it is assumed that reflective targets can be modelled as flat planes, for example, the walls of the vehicle. Following [60], we can model the RCS of a plat plane of a given area  $A$  as

$$\Gamma_{sc} = \frac{4\pi A^2}{\lambda^2} \quad (3.6)$$

where  $\lambda = \frac{c}{f_c}$ .

### 1. PATH LOSS

The Path loss associated to the static clutter can be defined as in 3.3 with  $Pr_{sc} = PL_{sc}\Gamma_{sc}$  with  $PL_{sc}$  being the propagation losses computed considering the static clutter to be the target as was done in  $PL_h$  for a human.

### 2. TOTAL EQUATION FOR STATIC CLUTTER SIMULATION

The total expression for the simulation of  $M$  static components can be derived as

$$z_{sc}(\tau, t) = \sum_{m=1}^M PL_{sc,m}\Gamma_{sc,m}\delta(\tau - \tau_{sc,m}(t), t) \quad (3.7)$$

where  $\tau_{sc} = \frac{R_{Tsc} + R_{Rsc} - L}{c}$  where  $R_{Tsc}$  and  $R_{Rsc}$  are the distances from the static clutter element to the transmitter and receiver respectively.

#### 3.2.3. PART 3: MODELLING OF MULTIPATH

If reflective objects are present in the environment, such as sides and ceiling of the vehicle, the reflections from the human will bounce on static objects and be received by the radar at further ranges, causing multipath effect. This can be observed in Figure 3.9, where the reflection from the human is found at range  $R_h = R_{Th} + R_{Rh} - L$  and the multipath component when the signal bounces on static objects appears at further ranges  $R_{Th} + R_{hsc} + R_{Rsc} - L$ . The component  $R_{MP}$ , therefore, corresponds to the range difference between the distance at which the human is observed  $R_h$ , and the distance at which reflected echos are observed.

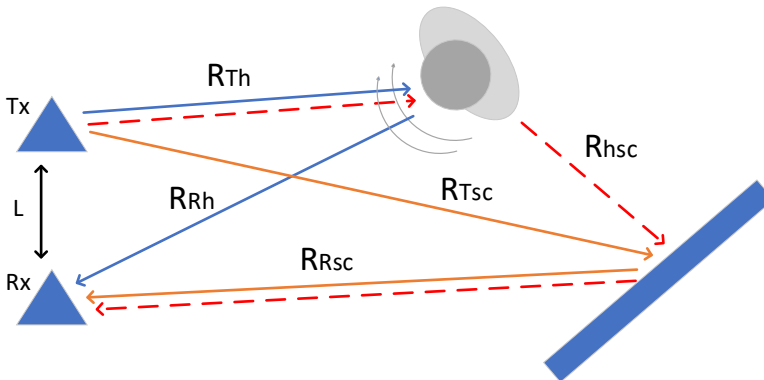


Figure 3.9: Schematic of multipath reflections, considering one transmitter, one receiver, one human in the scene (depicted in gray) and one reflecting target generating multipath (depicted in blue).

These signals will be modelled in amplitude and phase following the movement of human breathing as defined in the modelling of human targets.

To model the different  $R_{MP}$  range delays for a given human, we consider that a multipath echo is generated from each of the static objects that has been defined in the environment. Therefore, for  $N$  humans and  $M$  static components, a total of  $M * N$  multipath reflections will be obtained.

### 1. PATH LOSS IN MULTIPATH

Similarly to the derived expression which considers path loss for a LoS human target, we can express the received power as the multiplication of the path loss given by the distances travelled and the RCS of the objects that the signal interacts with.

Considering our model in which the multipath is a reflection between the human and a single target, each multipath echo's received power can be expressed as seen in 3.8

$$Pr_{MPm,n} = \sum_{n=1}^N \sum_{m=1}^M \frac{1}{4\pi R_{T,h_n}^2} \frac{1}{4\pi R_{h_n,sc_m}^2} \frac{1}{4\pi R_{R,sc_m}^2} \alpha_{h,n}(t) \Gamma_{sc,m} \quad (3.8)$$

where  $R_{T,h}$  is the distance from the transmitter to the human,  $R_{h,sc}$  is the distance from the human to the object, and  $R_{R,sc}$  is the distance from the object to the receiver.

### 2. TOTAL EQUATION

The total received signal for the multipath component generated by  $N$  humans and  $M$  static components can therefore be expressed as the summation of the convolution between the model for a breathing human  $z_{h,n}(\tau, t)$  with a delay  $\tau_{h,n}d$  corresponding to the position of the human as was derived in Equation 3.5, and a train of  $M$  deltas which introduce deterministic delays corresponding to  $R_{MP}$  as

$$z_{MP}(\tau, t) = \sum_{n=1}^N \sum_{m=1}^M z_{h,n}(\tau, t) * \frac{PL_{MPm,n}}{PL_{h,n}} \Gamma_{sc,m} \delta(\tau - \tau_{m,n}(t), t) \quad (3.9)$$

where  $\tau_{m,n}(t) = \frac{R_{MPm,n}}{c}$  is the time delay associated to the  $R_{MPm,n}$  distance. Note that the path loss considered in  $z_{h,n}(\tau, t)$  has been adjusted to that observed for the multipath echos with  $PL_{MPm,n}$ , and that  $\Gamma_{sc,m}$  is considered.

#### 3.2.4. FINAL EXPRESSION FOR MODELING CIR DATA WITH HUMANS, STATIC CLUTTER, AND MULTIPATH COMPONENTS

Finally, once the single human, its multipath components, and the static clutter have been simulated, zero-mean Gaussian noise  $n(\tau, t)$  is added with a given SNR.

It can be seen from the measurement data that depending on the amplitude of the chest or on the position of the people w.r.t. the radar, different SNR values can be used. A range of 0-20 dB is defined. The feasibility of this approach is shown in Figure 3.10, where the FFT of an experimental measurement of a breathing human is compared to that of a simulation with a randomly picked SNR value in the allocated range, specifically, 5dB. Very good agreement between the experimental data and the simulated data with the proposed model is shown.

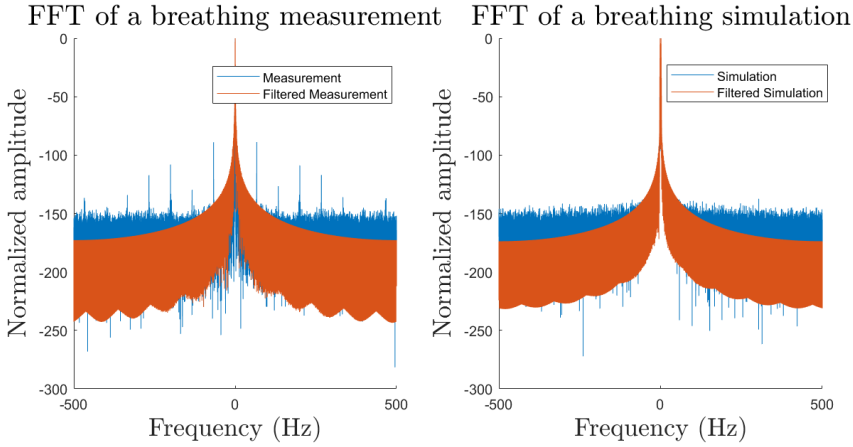


Figure 3.10: FFT of a breathing measurement in the identified range vs FFT of a Simulation using SNR value of 5dB

To summarize, the total expression for the simulation of CIR radar data is detailed in Equation 3.10 as the summation of the defined contributions.

$$z_{total}(\tau, t) = z_h(\tau, t) + z_{sc}(\tau, t) + z_{MP}(\tau, t) + n(\tau, t) \quad (3.10)$$

### 3.2.5. SIMULATION LIMITATIONS

Some limitations of this simulated model are acknowledged.

Firstly, only 1 multipath echo is considered to be generated from the static components. In reality, signals would bounce on multiple static clutter components and generate further multipath echos. However, given the assumption that the environment of the car is of a limited size, these echos can be in any case discarded as possible targets, therefore, they are not considered in the simulation. The reflection between multiple targets in the environment are also not considered given the fact that multipath echos from other humans will have lower amplitude than those coming from highly reflective objects such as metallic plates (car structure, for example).

Secondly, for RCS computation, monostatic assumptions for targets have been made due to lack of literature that discusses bistatic RCS analytically. Also, the system is limited to simple ellipsoid and flat plane models for humans and static components. In reality, targets are more complex.

Nevertheless, the proposed simulation framework can be considered a good approximation, showing very good agreement with experimental data and enabling simulations of many scenarios and key parameters in a Monte Carlo fashion.



# 4

## PRELIMINARY VALIDATION IN A CONTROLLED ENVIRONMENT

*This chapter presents the initial validation of the hardware, CIR simulation framework and developed algorithms by means of comparison with controlled data.*

*Firstly, to evaluate the CIR data extracted from the boards, an initial test is made to verify the ranging accuracy obtained with the different radars in the network. Secondly, the same test is done for the simulated CIR data, and results are given for the ranging accuracy improvement defined in the algorithm.*

*After the CIR data ranging capabilities have been evaluated, the performance of the algorithm is studied through the processing of one iteration of simulated CIR data of a single-breathing person in an ideal environment (no reflections). It can be observed that detection of vital signs and localization are ideal.*

*Finally, seeing the effect that various algorithm parameters have in the processing results for both detection and association blocks, a discussion on the effect of these parameters is presented and conclusions are drawn.*

### 4.1. VALIDATION OF THE CIR RADAR DATA OBTAINED WITH THE UWB RADAR NETWORK

Due to the complexity of the prototype built for the multistatic radar network, it is important to study its ranging capabilities. For this purpose, the boards are positioned in the anechoic chamber of TU Delft, an ideal scenario where no multipath effect should be observed. A reflective metallic object is located in the center of the chamber, and the boards are placed as can be seen in Figure 4.1

There is a special interest to observe the measured distances to the object with the bistatic Rx, after having applied the ranging correction factor of  $R_h = R_{Th} + R_{Rh} = (\tau_{received}c) + L$  that was discussed in Chapter 4.2.

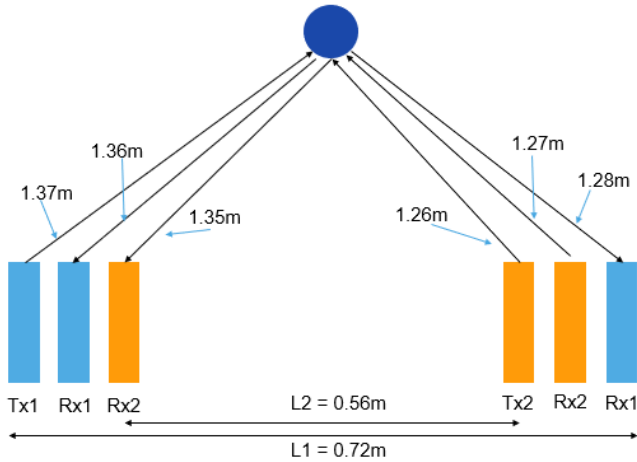


Figure 4.1: Positioning of boards and sphere in Anechoic Chamber of TU Delft for initial ranging test

#### 4.1.1. RESULTS FOR DIHEDRAL RANGE VALIDATION IN ANECHOIC CHAMBER

For this test, both a metallic sphere and a dihedral were placed in the center point of the room. However, due to its smaller RCS, and the fact that the anechoic chamber presented other reflective objects to hold the structure of the setup, the sphere was not easily detected by the radars. Therefore, the results with the dihedral are presented.

For reference, in Figure 4.2, an image of the received CIR data is presented. An empty measurement taken without the reflective object has been subtracted from the captured CIR radar data, in an attempt to remove other reflective objects in the environment, as could be the structures that hold the boards, or the door of the anechoic chamber.

In Figure 4.3 the range-profile of the received data obtained by averaging the amplitude of the samples in slow-time is shown. As can be seen, each radar observes the dihedral at a different position.

In Table 4.1 the results are shown for the ranges at which the target is observed with the radar and the measured ranges at which the target was placed in reality, with the corresponding error between them.

Radar	Measured ranges (m)	Real ranges (m)	Error (m)
Monostatic Rx 1	2.70	2.72	0.02
Bistatic Rx 1	2.52	2.65	0.13
Monostatic Rx 2	2.70	2.54	0.16
Bistatic Rx 2	2.66	2.61	0.05

Table 4.1: Comparison between the real ranges to the reflective object and the measured ranges with the different radars after correction of range offset has been applied.

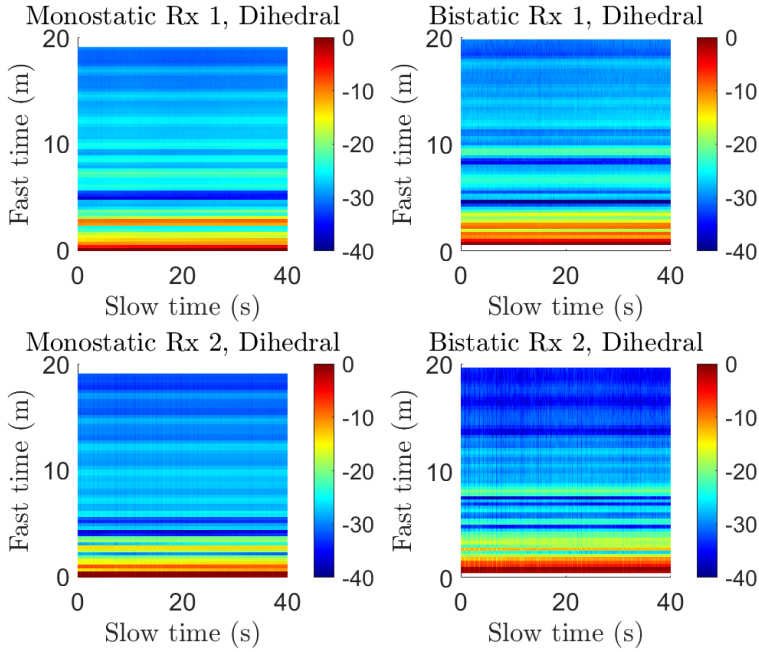


Figure 4.2: CIR radar matrices obtained in measurements of a dihedral in anechoic chamber

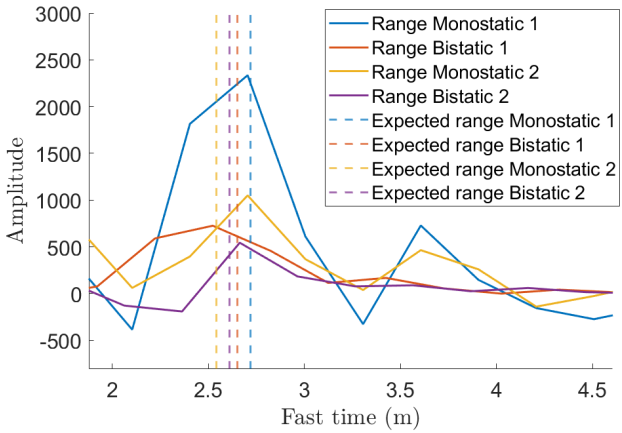


Figure 4.3: Ranging accuracy of each of the Rx boards after correcting the ranges with factor  $L$

#### 4.1.2. CONCLUSIONS ON RANGE VALIDATION IN ANECHOIC CHAMBER

As can be seen, due to the range resolution of  $\Delta R = 0.3m$ , observing the position of target with accuracy of more than a few cm is complex. However, it can be concluded that the range compensation has been applied correctly since the bistatic ranges highly resemble the measured ones. Without the compensation of  $L_1 = 0.72m$  and  $L_2 = 0.56m$  for bistatic Rx 1 and 2 respectively, the error would be much larger than the range resolution. Therefore, it can be concluded that the target can be detected within enough ranging accuracy by all radars in the radar network.

The effect of the accuracy in the detection will be evaluated for target localization purposes in other sections in this Chapter. Due to the fact that the object present is static, the processing algorithm cannot be used to perform detection and localization. However, it is expected that for human targets, the ranging accuracy obtained can be improved by the cluster-averaging of the detections defined in Chapter 2.

4

#### 4.2. VALIDATION OF THE SIMULATED CIR RADAR DATA

A study on the simulated CIR data generated by the proposed framework described in Chapter 3 is presented in this section in order to evaluate its accuracy.

For this, a single simulation is evaluated.

##### 4.2.1. RESULTS FOR SIMULATION RANGE VALIDATION IN IDEAL ENVIRONMENT

A human is simulated in an ideal environment with no reflections. The human and the boards are placed in similar positions as the experiment conducted in the previous section (see Figure 4.1).

The different parameters used to generate this target are defined in Table 4.2 with values defined in [61], [25], [2].

Variables	Value
$f_b$	0.5 Hz
Chest size	[0.3,0.2,0.45](m)
Chest displacement	5 (mm)
SNR	10 (dB)

Table 4.2: Human simulation used parameters. Note that the chest displacement and the chest size (ellipsoid model sizes) have realistic values from [2]

The obtained CIR data is presented in Figure 4.4.

In Figure 4.5, the range-profile of the received data obtained by averaging the amplitude of the samples in slow-time is shown.

As can be seen, again these simulations present some residual ranging error. In Chapter 2, it was defined that for human detection, in order to improve detection accuracy, the clusters obtained in the Range-Doppler map would be computed as averages weighed on the energy of the range-bins, instead of using just the range bin where the maximum

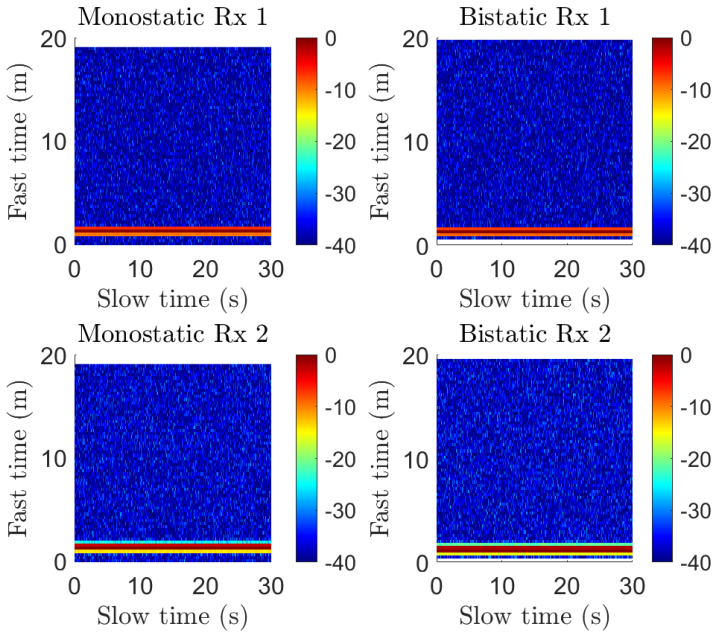


Figure 4.4: CIR radar data obtained with the human simulation in the defined ideal environment

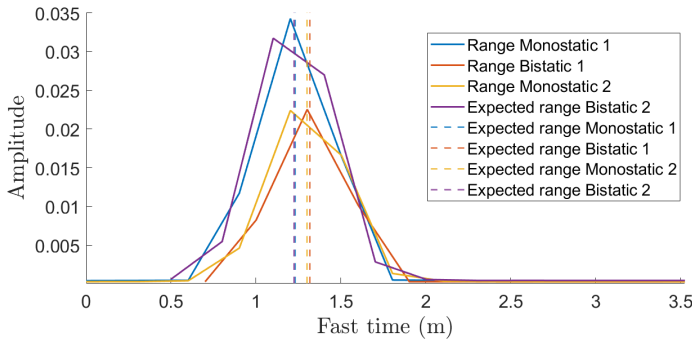


Figure 4.5: CIR radar data obtained with the human simulation in the defined ideal environment

is found. In Table 4.3 the ranging accuracy is compared between calculating the range where the human is present using the location of the maximum energy range-bin vs averaging the detection clusters in the Range-Doppler map. The latter approach significantly reduces the ranging error.

Radar	Real Range (m)	Max peak (m)	Cluster av. (m)	Error max peak (m)	Error cluster (m)
Monostatic Rx 1	1.22	1.2	1.2	0.02	0.02
Bistatic Rx 1	1.32	1.31	1.3	0.05	0.01
Monostatic Rx 2	1.30	1.2	1.30	0.10	0
Bistatic Rx 2	1.22	1.1	1.24	0.12	0.02

Table 4.3: Comparison between the obtained ranges to the simulated human and the defined ranges with the different radars

#### 4.2.2. CONCLUSIONS ON RANGE VALIDATION FOR THE SIMULATION

It can be seen how, as was expected, the ranging accuracy improves greatly by using the averaging of the detections in the range-Doppler map. Therefore, this is considered a good approach to solve the problem of ranging accuracy for localization due to limited radar range resolution.

### 4.3. VALIDATION OF THE ALGORITHM PERFORMANCE WITH SIMULATED CIR RADAR DATA IN CONTROLLED SETUP

In this section, the pipeline proposed in Chapter 2 is validated by studying the processing of a single simulation of CIR radar data in an environment where a human is present. This same environment is also considered in Chapter 5, in a Monte Carlo fashion, as it attempts to recreate the presented experimental measurements obtained in the anechoic chamber of TU Delft. The focus of this preliminary validation of a single simulation is to test that the processing pipeline is capable of accurately detecting and locating an unknown number of humans in the environment and that the simulated data accurately resembles that of an experimental measurement.

Firstly, similarly as was done in the previous section, the simulation environment is defined with the positions of the boards and the characteristics of the human.

Secondly, the parameters of the processing pipeline are introduced and defined. As can be seen on Figure 2.1, there are separate processing blocks in the algorithm, namely the detection block and the association block. In this example, the different outputs of the blocks defined are studied as the simulated data is processed.

#### 4.3.1. DEFINITION OF SIMULATION ENVIRONMENT

Firstly, the environment is defined. The radar boards are virtually placed in the positions defined in Table 4.4. In the 3D space around the boards, a target is placed in the coordinates  $[-0.8, 0.2, -0.1]$  (m), and the parameters used for target generation are summarized in Table 4.5. For an overview of the setup, refer to Figure 4.9, where the final result for localization is shown.

Board	[x,y,z] (m)	Frequency (GHz)
Tx1	[-0.05,0.2,0]	6.5
Tx2	[0.05,1.32,-0.1]	7.5
Rx1 monostatic	[0,0.2,0]	6.5
Rx1 bistatic	[-0.05,1.32,-0.1]	6.5
Rx2 monostatic	[0,1.32,-0.1]	7.5
Rx2 bistatic	[0.05,0.2,0]	7.5

Table 4.4: Definition of the parameters related to the location/topology of the radar units for the simulated test

Variables	Value
Coordinates	[-0.8, 0.2, -0.1] (m)
$f_b$	0.3 Hz
Chest size	[0.3,0.25,0.45](m)
Chest displacement	5 mm
SNR	10 dB

Table 4.5: Human simulation used parameters. Note that the chest displacement and the chest size (ellipsoid model sizes) have realistic values from [2]

### 4.3.2. PROCESSING OF THE SIMULATION

Firstly, in Figure 4.6, the 4 different CIR radar data matrices generated are shown.

#### 1. EVALUATION OF THE DETECTION BLOCK

The complex CIR data matrices are filtered with a Butterworth band-pass filter to eliminate the static components and higher-frequency noise. The result can be seen in Figure 4.7

After filtering the data, the Range-Doppler plot is computed for each Rx, and the 2D-CFAR algorithm is applied on the interest range-frequency area in which the human can be. In this case, a value for 2D-CFAR  $P_{fa}$  of  $1e-3$  is used. In Chapter 2, it was stated that the human can be found in a region of interest, namely the human can be assumed to be in a range lower than the longest distance in which it can be found in a particular environment, and with a breathing frequency in the established human breathing range. For the particular space defined, the human return cannot be found after 3 meters in range, and as stated in the literature, human breathing frequency is of [0.1 - 0.8] Hz [25]. This defines the region in which 2D-CFAR detection is applied.

The resulting Range-Doppler plots with the detections can be seen in Figure 4.8. In each simulation, a few clusters of detections have been made (blue dots). When the cluster-averaging process is applied, the average detections (yellow dots) are considered the range and breathing frequency values for each detection.

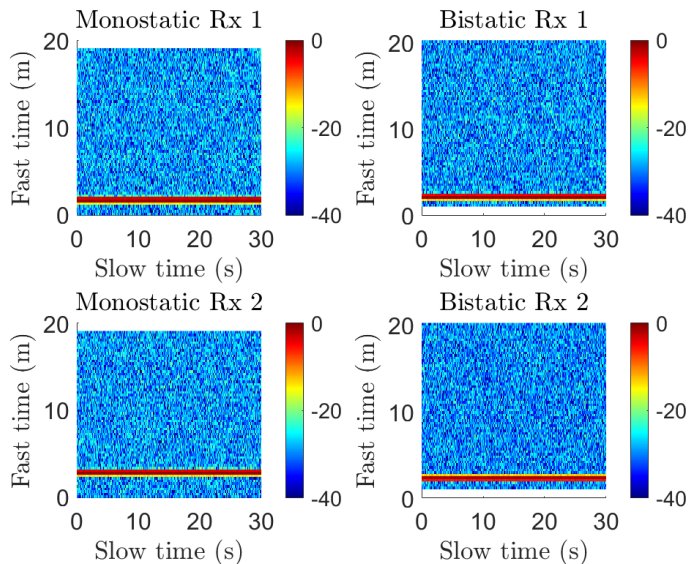


Figure 4.6: Top left: Simulated CIR data from monostatic Rx 1. Top right: Simulated CIR data from bistatic Rx 1. Bottom-left: Simulated CIR data from monostatic Rx 2. Bottom-right: Simulated CIR data from bistatic Rx 2

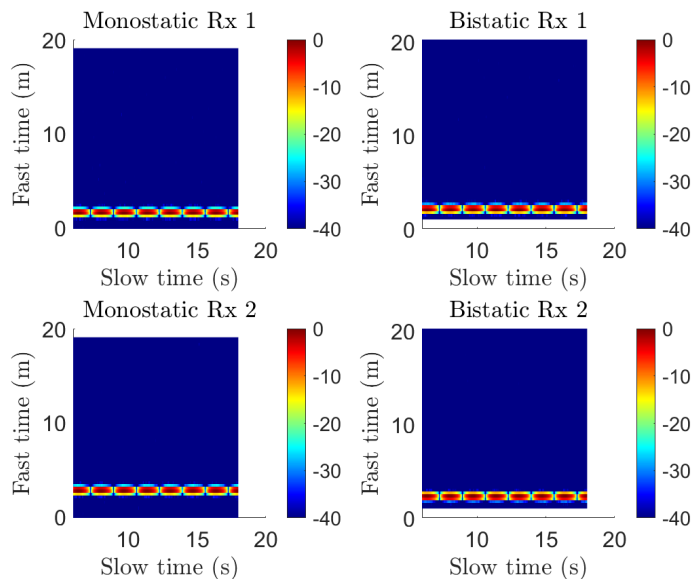


Figure 4.7: Top left: Simulated CIR data from monostatic Rx 1. Top right: Simulated CIR data from bistatic Rx 1. Bottom-left: Simulated CIR data from monostatic Rx 2. Bottom-right: Simulated CIR data from bistatic Rx 2

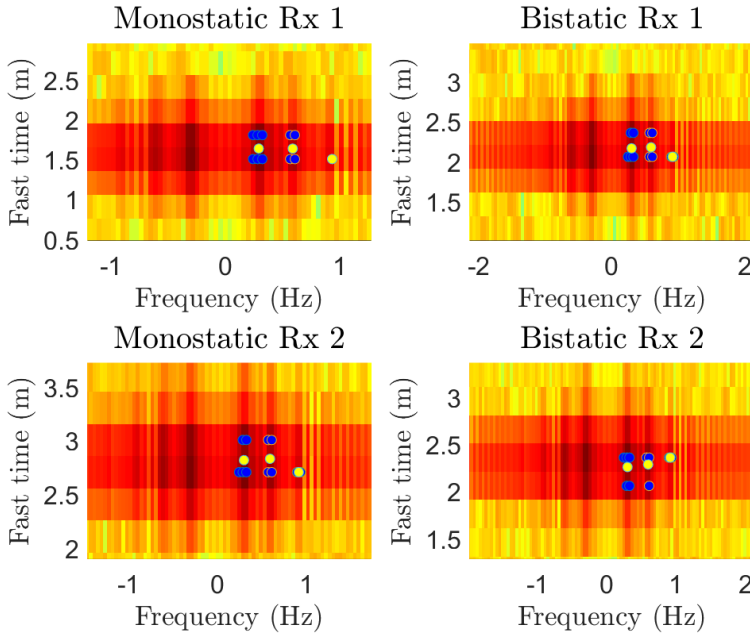


Figure 4.8: Top left: Simulated Range-Doppler data from monostatic Rx 1. Top right: Simulated Range-Doppler data from bistatic Rx 1. Bottom-left: Simulated Range-Doppler data from monostatic Rx 2. Bottom-right: Simulated Range-Doppler data from bistatic Rx 2. The blue dots are the identified range-frequency cells which may correspond to a human being, and the yellow dots are the result of averaging the detection clusters.

Finally, the classifier block is applied to ensure that each of the identified detections correspond to possible static humans.

The final detections matrices including the range-frequency averages (yellow dots seen in Figure 4.8) identified in each receiver are sent to the association algorithm. In Table 4.6, a comparison is made between the detection matrix  $\mathbf{D}_m$  in each of  $1 < m < 4$  radar Rx and the true range-frequency information that the radar should have detected. As can be seen, there are a few false alarms attributed to breathing harmonics, however, all detections point towards the same target.

Receiver	Detections [range(m); $f_b$ (Hz)]	True target [range(m); $f_b$ (Hz)]
Monostatic 1	[1.63,1.63,1.50; 0.29,0.59,0.94]	[1.61; 0.3]
Bistatic 1	[2.16,2.17,2.06; 0.3,0.59,0.92]	[2.13; 0.3]
Monostatic 2	[2.82,2.83,2.70; 0.3,0.59,0.91]	[2.79; 0.3]
Bistatic 2	[2.26,2.28,2.36; 0.30,0.60,0.91]	[2.29; 0.3]

Table 4.6: Detections matrix comparison to true target range and breathing frequency

## 2. EVALUATION OF THE ASSOCIATION BLOCK

The association algorithm is capable of associating the ranges corresponding to the true breathing frequency (0.3Hz) correctly, and the rest of the detections corresponding to harmonics are also grouped amongst Rx by their estimated breathing frequencies.

3 targets are therefore identified. 2 of them have been localized with 0 localization error as ranging accuracy is very high, with a maximum error of 3cm as can be seen in Table 4.6. However, for the 3rd target associated, corresponding to the last breathing harmonic, the energy of the target is smaller, and the cluster range-average presents more range error in the detection stage. Therefore, localization capabilities are compromised, leading to increased localization error.

The final localization step can be seen in Figure 4.9, where good performance of the proposed detection and localization approach is shown.

4

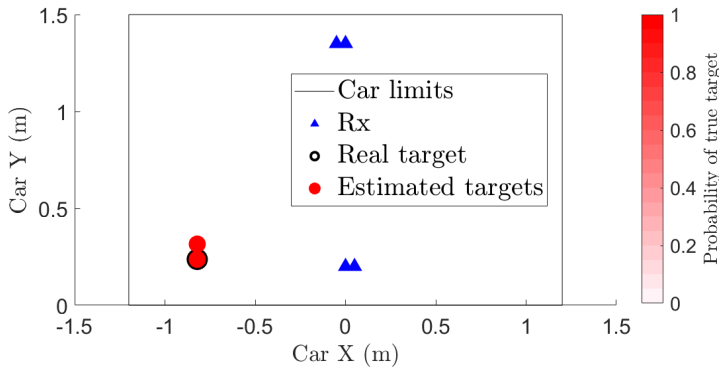


Figure 4.9: Final position Estimation of one simulated target in an environment that recreates the experimental measurements performed in TU Delft's anechoic chamber presented in Chapter 5.

### 4.3.3. CONCLUSIONS ON THE PROCESSING OF THE SIMULATION WITH THE DEVELOPED ALGORITHM

From this simulated test, it can be concluded that the proposed algorithm is capable of detecting the targets and associating the information from the multiple receivers in order to provide a final localization estimate of the identified targets.

With this, it is considered that the simulation framework can be used to generate measurements of a particular environment in order to evaluate the detection and localization performance.

Note how the breathing frequency harmonics are detected because low-sensitivity thresholds were used for the detection. That is, high values for 2D-CFAR  $P_{fa}$  were set. If lower values of 2D-CFAR  $P_{fa}$  are used, less clusters will be detected. Finding an appropriate value for this is complex, as restricting this value can also affect the ranging accuracy of the detections, worsening the total localization accuracy as was shown in this example.

Moreover, the effect of not just the 2D-CFAR  $P_{fa}$  values used, but also other parameters in the processing algorithm should be studied, namely the duration of the measurement and the  $\Delta F$  resolution, to determine the effect they will have on the processing.

#### 4.4. THE EFFECT OF THE PARAMETERS

Various parameters are considered in the processing of the CIR data as described in Chapter 2. These can be summarized in Table 4.7.

Parameter	Value/ Range	Data
Duration (s)	12	Long enough to detect a period in the breathing. If too short, estimating the periodic breathing frequency is not possible. If too long, real-time applications become less realistic
2D-CFAR $P_{fa}$	0.001- 0.02	Large enough to detect human in environment. If too large, false alarms are detected and if close-multiple targets, they might be merged into the same target
$\Delta F$	0.04 Hz	Defines the resolution in the frequency domain for breathing frequency estimation in the 2D-CFAR algorithm. If the value is high, targets with differentiable breathing frequencies in range-proximity might be undifferentiated. If too small, computational complexity increases.

Table 4.7: Important parameters for processing and how they affect the data

The variation of each of these will impact the overall performance of the algorithm. For the correct processing of the simulations and the measurements, values for each of these parameters have been tested, and some conclusions can be extracted on how the output of the algorithm is affected.

These are briefly discussed in this section.

##### 4.4.1. DURATION

The duration of the measurement directly affects the estimation of the breathing pattern. The longer the processed CIR data is, the easier it will be for the algorithm to detect a periodic pattern in the breathing. However, the more likely it is that  $f_b$  changes over time or that a human moves in a real-life experiment.

Since a human breathing period is of between 1.25 - 5 seconds, the standard value chosen for the measurement duration is of 12 seconds. This allows several periods to be present in the measurement.

#### 4.4.2. 2D-CFAR $P_{fa}$

As briefly mentioned in the introduction of the 2D-CFAR algorithm and in the last section, this parameter plays a key part in the detection block. If the value is too high, false alarms will appear in the detection, and in case of multiple people, several detection clusters might be joint in the same. If it's too small, missed detections may be obtained because the detection sensitivity is not high enough.

An example can be found on Figure 4.10. In this case, the same environment defined in Table 4.4 was used, with the addition of a new target in position  $[-0.8, 0.9, -0.1]$ . A low  $P_{fa}$  value of  $1e-5$  was used in all receivers.

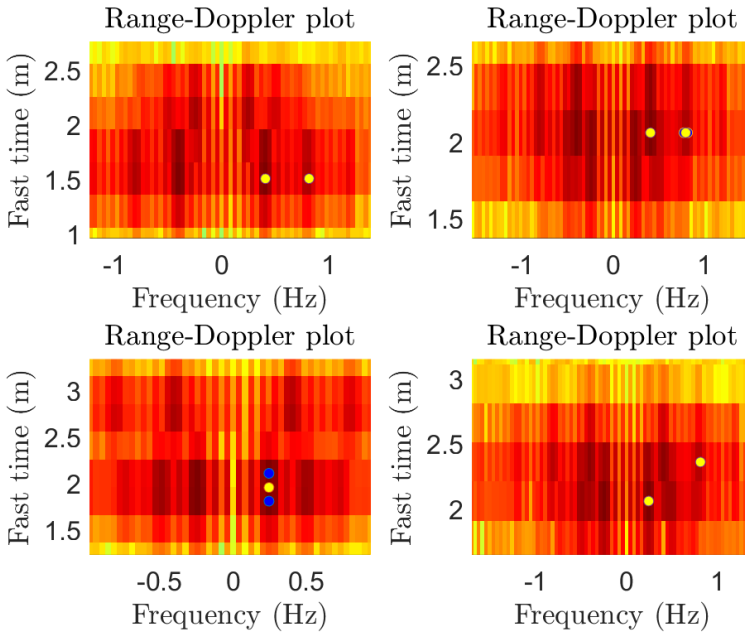


Figure 4.10: Range Doppler plot and detections for Rx monostatic 1 (top-left), Rx bistatic 1 (top-right), Rx monostatic 2 (bottom-left), Rx bistatic 2 (bottom-right) with  $P_{fa} = 1e-5$

As a result of lowering the  $P_{fa}$ , both targets are not detected in all receivers and the ranging accuracy is compromised, since only one range-bin is identified per cluster, and averaging with neighboring bins is not possible.

As a result, one target cannot be properly located and localization accuracy has decreased. This can be seen in Figure 4.11.

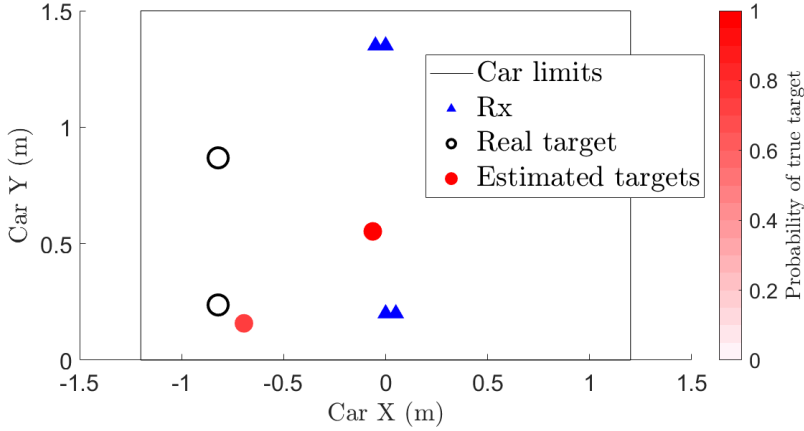


Figure 4.11: Localization of targets with  $P_{fa} = 1e-5$ . A decrease in localization accuracy is observed, and the inability to locate the second target is noted.

If the value for  $P_{fa}$  is increased to a high value of  $1e-2$ , the detection improvement in the Range Doppler plot can be seen in Figure 4.12.

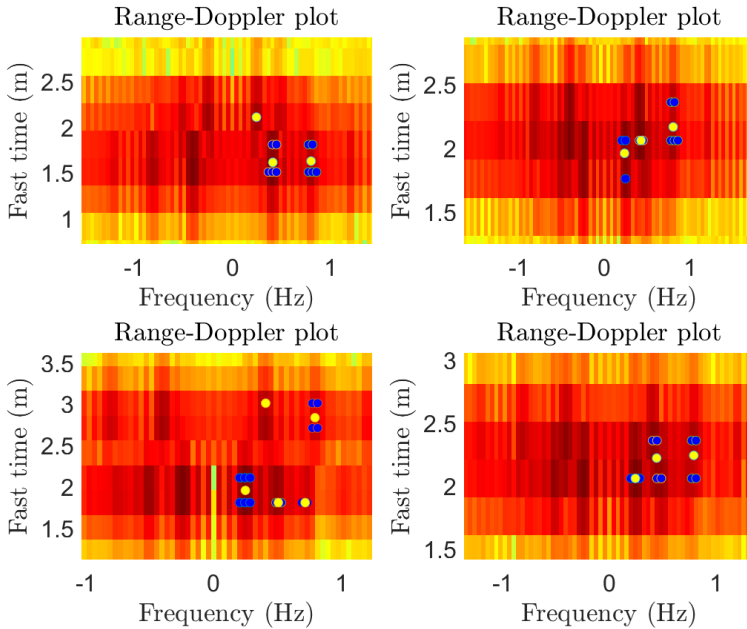


Figure 4.12: Range Doppler plot and detections for Rx monostatic 1 (top-left), Rx bistatic 1 (top-right), Rx monostatic 2 (bottom-left), Rx bistatic 2 (bottom-right) with  $P_{fa} = 1e-2$

The final localization result shown in Figure 4.13, thus, does not have missed targets as all were detected and the hypothesis were properly associated. However, more ghost targets appear in the environment as a result of the increased amount of false alarms in the detection matrices. This can also be observed to affect the localization accuracy for one target, as errors might be introduced in the association.

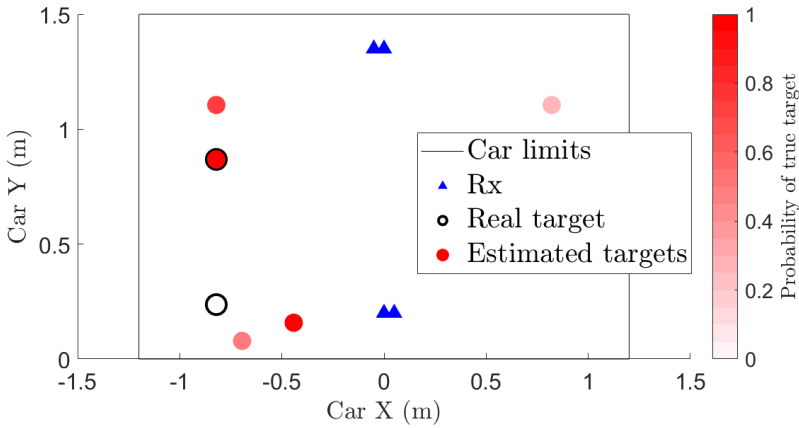


Figure 4.13: Localization of targets with  $P_{fa} = 1e-2$

Therefore, establishing a correct parameter for  $P_{fa}$  is complex. For the scope of this thesis, a range of experimentally tested values is used as defined in Table 4.7. Experimental and simulated CIR data alike are processed with values within this range.

Future work can focus on the development of an optimization tool, or on the development of a different detector with more quantifiable performance evaluation based on its parameters. In Chapter 6, this is proposed in the Future Work section.

#### 4.4.3. FFT WINDOW SIZE

The defined FFT Window Size is directly proportional to the resolution in the frequency domain for the estimation of the breathing frequency. If the resolution is bigger than the frequency differentiation in between multiple targets placed in closeness, these could be falsely identified as an extended single target breathing at an in-between frequency.

Therefore, a longer window size, thus a smaller frequency resolution that allows the differentiation of multiple targets is used. It has been found experimentally that using a resolution of 0.04 Hz yields good separation without increasing computational complexity significantly.

## 4.5. CONCLUSIONS ON THE VALIDATION

In this section, various validation studies on different components of the developed setup, CIR data simulation framework, and processing algorithms have been presented separately.

Firstly, it can be concluded that the developed hardware can correctly detect the targets with accurate ranging after the bistatic compensation. There is no observation of interference between the anchors, therefore it can be said that the multiplexing method of FDMA is appropriate for the construction of an UWB radar network using Ranger4 boards.

Secondly, the same ranging accuracy study has been performed on the simulation of a breathing human in the environment. The simulations have been processed with the detector, and the different detection clusters have been identified using 2D-CFAR algorithm. The ranging error obtained by looking at the range bin with maximum energy in each cluster, and the error obtained by computing an average range inside the cluster have been compared, and it has been determined that the averaging technique proposed greatly improves the ranging accuracy with respect to methods presented in literature, which use the maximum energy method.

Thirdly, it can be concluded that the algorithm is capable of detecting the simulated human with very good accuracy in ideal scenarios. This indicates that the CIR radar data simulations developed can be used to evaluate various scenarios with different radar positions and human being parameters.

However, it was found that the parameters used in the algorithm to process the data, play a key role in the performance and should be studied.

Finally, a study of said parameters is presented. A discussion on the effect that their variation has on the final detection and association results is given, together with a justification of the final choice made for such parameters.

Overall, it can be concluded that both the board setup prototype and the simulated CIR data can be used to evaluate results for multiple people location using the processing pipeline proposed, and that this, in turn, is capable of detecting the humans with good ranging accuracy of a few cm, and to associate the detections for accurate localization. The performance of this algorithm will also vary depending on various parameters that have been identified.

In the next Chapter 5, an extensive experimental validation is performed. For this, experimental measurements are evaluated and compared to Monte Carlo simulations of CIR radar data which mirror the real-life environments of the experiments.



# 5

## EXTENSIVE EXPERIMENTAL VALIDATION

*In this chapter, the algorithm proposed is tested in various sets of measurements, namely in the anechoic chamber of TU Delft and inside NXP's test car in the High Tech Campus.*

*Moreover, given the inability to extract large batches of consistent measurements due to the complexity of the hardware, the results obtained with the experimental data are compared to those obtained after generating sets of Monte Carlo iterations of simulated radar data. The simulations can be compared as they recreate the same environments as the experimental measurements using the proposed simulation framework. The tests are made for single people and multiple people placed in the surroundings of the setup, and conclusions are extracted on the feasibility of localizing multiple people in ideal scenarios and in multipath-dense scenarios. A block diagram of the comparison process is shown in Figure 5.1.*

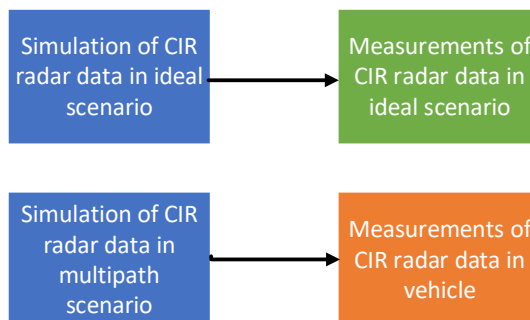


Figure 5.1: Block diagram of experimental validation of the setup

Finally, the current setup limitations are identified and new setups are proposed to overcome them. The results of Monte Carlo simulations for these new scenarios are presented and evaluated. A final conclusion on the obtained results and feasibility of the proposed solution is presented.

## 5.1. MEASUREMENT SETUP AND CIR SIMULATION COMPARISON IN THE ANECHOIC CHAMBER

A comparison is made in between simulated CIR data generated by the proposed framework and experimentally measured radar data captured in the anechoic chamber of TU Delft with the hardware characterized in Chapter 3.1, as a general evaluation based solely on experimental data is hard to obtain due to the hardware limitations. For this, Monte Carlo simulations for the radar data attempt to recreate the characteristics of the measurement setup.

Both simulated and measured data matrices are processed with the discussed processing algorithm, and their results are evaluated and compared in the following sections.

The 6 UWB radar boards are positioned similarly as they would be inside a vehicle in the anechoic chamber, and virtually in the simulations, following the positions defined in Table 5.1. A schematic of the evaluated scenario can be found in Figure 5.2.

Board	[x,y,z] (m)	Frequency (GHz)
Tx1	[-0.05,0.2,0]	6.5
Tx2	[0.05,1.32,-0.1]	7.5
Rx1 mono	[0,0.2,0]	6.5
Rx1 bi	[-0.05,1.32,-0.1]	6.5
Rx2 mono	[0,1.32,-0.1]	7.5
Rx2bi	[0.05,0.2,0]	7.5

Table 5.1: Board configuration in measurements and simulation in ideal scenario in anechoic chamber

Various people are placed in the occupancy areas A and B, both individually and together at the same time. The coordinates of these positions w.r.t. the environment depicted in Figure 5.2 are specified in Table 5.2.

Target	Coordinates (m)
Coordinates pos. A	[-0.8, 0.2, -0.1]
Coordinates pos. B	[-0.8, 0.9, -0.1]

Table 5.2: Human simulation coordinates in anechoic chamber

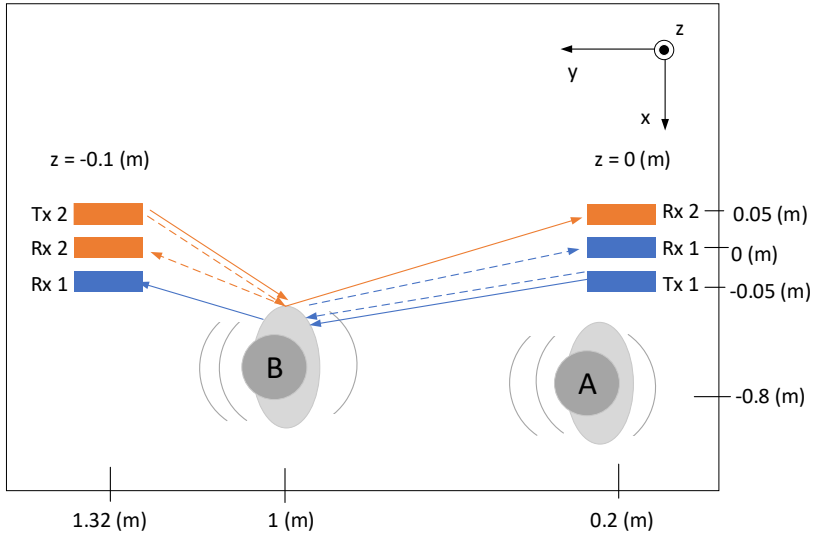


Figure 5.2: Schematic of board and human-occupancy placement for measurements in the anechoic chamber

In Table 5.3 the human-occupancy distribution over the different simulations/measurements can be seen.

Scenario	A	B
1	X	O
2	O	X
3	X	X

Table 5.3: Human-occupancy distribution in anechoic chamber

Finally, in Table 5.4, the ranges of values used in the algorithm to process both the CIR measurements and the CIR simulations are presented.

Variables	Value / Value Range
Duration	12 (s)
$P_{fa}$ of 2D-CFAR	[0.003 - 0.012]
$\Delta F$ (frequency resolution)	0.04 (Hz)

Table 5.4: Parameter range values used for both the processing of the measurements and the simulations alike

Firstly, the processing of the simulation is evaluated, and finally, the results are presented for the processing of the experimental data. Comparisons are made in the next section and conclusions are extracted.

### 5.1.1. PERFORMANCE EVALUATION WITH MONTE CARLO SIMULATIONS OF CIR RADAR DATA

The simulation is designed in the same way as the anechoic chamber experiments, with the boards virtually placed in the positions described in Table 5.1, and the simulated targets placed following Table 5.2.

As for the generation of the targets, various variables are considered. These have been summarized in Table 5.5. As defined in the literature[25], the breathing frequency of a human is between [0.1 - 0.8] Hz, and the chest amplitude is [5-15]mm [61].

Parameter	Value range
Breathing frequency $f_b$	[0.1 - 0.8] (Hz)
Chest displacement amplitude $m_b$	[5 - 15] (mm)
Human torso size (ellipsoid) [x,y,z]	[0.2,0.3,0.45] (m)
SNR	10 (dB)

Table 5.5: Ranges of values used for the simulations of humans in the anechoic chamber environment

Monte Carlo simulations can be used to generate various repetitions with randomly generated variables and thus obtain a statistical evaluation of the performance of the simulations.

A differentiation can be made between the parameters used to generate the human body radar signature, as are the breathing amplitude ( $m_b$ ) and the breathing frequency ( $f_b$ ), and the noise level introduced in the simulation.

For the purpose of evaluating the general accuracy of the CIR radar data simulation, mainly of the detection and localization properties, 100 Monte Carlo simulations are defined with constant SNR level. Depending on the experimental measurement, different values of SNR can be obtained. In order to follow a standard evaluation throughout this thesis, the value picked is of 10dB, as was also the case in [2]. The parameters  $f_b$  and  $m_b$  are sampled in the following a uniform distribution in the defined range in Table 5.5.

Finally, to evaluate the simulations, performance metrics need to be defined. A differentiation between detection metrics and association metrics is made. For the detection block:

- Probability of detection (PD) (monostatic radar)
- Probability of detection (bistatic radar)
- Average number of false Alarms (N FA)(monostatic radar)

- Average number of false Alarms (bistatic radar)
- Average Detection range error (monostatic radar)
- Average Detection range error (bistatic radar)

For the association block:

- Number of targets associated
- Number of ghost targets
- Number of missed targets
- Localization error of detected targets

If a given target has been identified by the radar in an expected target range, it is considered to be a detection (PD). For multiple targets, in this case a maximum of 2, the total amount of targets present in the environment is considered for the computation of the detection probabilities. That is, the number of real detected targets is counted in each of the iterations, and the final number is averaged over the 100 iterations and divided by the number of real targets. Moreover, the results are given by averaging the performance of both monostatic and bistatic radars. For each detection identified, the detection range error is computed to evaluate its accuracy. Similarly to the probability of detection, the average number of false alarms (FA) is an indicator of the detector's performance. This is accounted for in the same way as PD, but counting the number of falsely detected targets in each iteration and averaging it over the 100 Monte Carlo repetitions.

As for the association, the average number of targets is computed after removing targets with probability of less than 75%. Out of these targets, their localization Root Mean Square Error (RMSE) is computed for the true position of the simulated targets. From there, the number of missed targets is increased if no associated targets are near a particular true position, and ghost targets are increased if a particular associated target is not near any simulated initial position. This threshold distance is defined as 0.19m, in this case, the halfway distance between targets A and B. Out of the associated targets considered a good detection, the localization RMSE is computed. An average over all the iterations is given for the defined parameters.

The results for the performance metrics obtained after considering all 100 Monte Carlo simulations defined for each of the occupancy scenarios defined in Table 5.3 ('ID' on the 1st column) can be seen on Table 5.6. The 2D-CFAR  $P_{fa}$  values used were of  $4e-3$  and  $5e-3$  for monostatic and bistatic radar respectively.

ID	PD		N FA		Range Error (cm)		N Target	N Ghost	N Miss	Loc Error (cm)
	Mono	Bi	Mono	Bi	Mono	Bi				
1	0.99	1	0.98	1.09	2.5	3.3	1.94	0.54	0.18	5
2	1	0.98	0.92	0.86	1	2.4	1.71	0.42	0.07	3
3	0.65	0.807	0.75	0.36	3	4.7	1.76	0.74	1.08	[7.3;2.9]

Table 5.6: Result of Monte Carlo Simulations, where Scenario indicates the type of scenario simulated as seen on Table 5.3 and performance metrics are shown for each of them.

### 5.1.2. CONCLUSIONS ON THE ANALYSIS OF THE MONTE CARLO SIMULATION RESULTS

- Firstly, high PD values can be observed for scenarios 1 and 2 in which a single target is present in the environment. This was to be expected. However, a noticeable drop in the detection capabilities is observed for two-people, mainly for monostatic radars. Monostatic radar in this setup struggles to see different targets, as one is much closer to the antennas than the other, while bistatic radar is capable of differentiating multiple people. Therefore, one of the advantages of including bistatic radars and of observing the scene from multiple points can already be observed in this simulation.
- Monostatic radars present more ranging accuracy than bistatic radars.
- The average number of false alarms is high, of almost one false detection per radar in single-target scenarios, but lower in double-target scenarios. Thus, if 2D-CFAR  $P_{fa}$  is maintained, less false alarms appear as more targets are introduced in the environment.
- The appearance of ghost targets is more prominent as more people are introduced in the scene, and the number of missed targets increases drastically as more people are in the scene, averaging around 1 missed target for 2 people in the environment.
- Finally, localization RMSE is observed to be higher for double-target scenarios. This can be mainly attributed to the fact that PD has decreased, therefore less detections can be accounted for in the range vector for localization. The removal of range information to perform localization will worsen the accuracy of the localization algorithm.

### 5.1.3. MEASUREMENTS IN ANECHOIC CHAMBER

The targets are placed in positions A and B as seen on Table 5.3. The boards and the position of the antennas can be observed in Figure 5.3. This configuration was constrained by the structure of the chamber and its components.

A limited amount of experimental measurements is obtained, specifically a total of 10 viable measurements are evaluated. In Annex C, a detailed study of the processing of these measurements performed in the anechoic chamber is attached. In it, the same performance metrics defined for the Monte Carlo simulations are applied to the individual results extracted from the measurements.

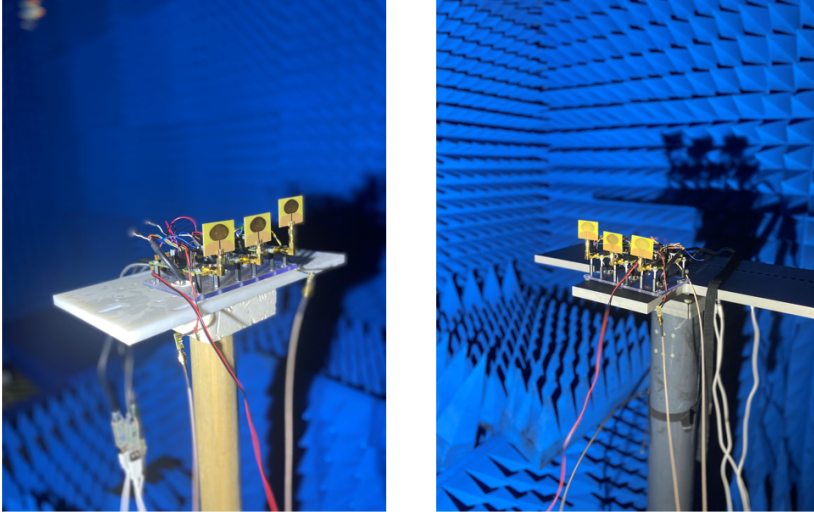


Figure 5.3: (Left): Tx2 , Rx monostatic 2, Rx bistatic 1 in anechoic chamber. Omnidirectional antennas facing forward. (Right): Tx1 , Rx monostatic 1, Rx bistatic 2 in anechoic chamber. Omnidirectional antennas facing forward.

### 1. RESULT EVALUATION FOR SINGLE-PERSON SCENARIO

4 single person measurement results are evaluated. These are labeled 3,4,5,7 in Table C.1. As an example of results of a single-person breathing in positions A and B, measurements 5 and 3 are shown in Figures 5.4 and 5.5 respectively.

As can be observed in Table C.1, values for 2D-CFAR  $P_{fa}$  for single target scenarios, range between 0.018 - 0.021 for monostatic radars and 0.006-0.012 for bistatic radars. Varying these values has a high impact on the results, as already noted.

From both these figures and the analysis attached in Annex C, it can be observed that:

- All radars are capable of detecting the target in all measurements, thus concluding that the detection of single-targets has ideal results.
- Ranging accuracy presents error in the order of a few centimeters, as was to be expected in the validation study performed in Chapter 4.1 with a dihedral.
- Some measurements found 2 targets in the single target scenario. In some cases, one of them can be attributed to a ghost target as a result of association of false alarms.

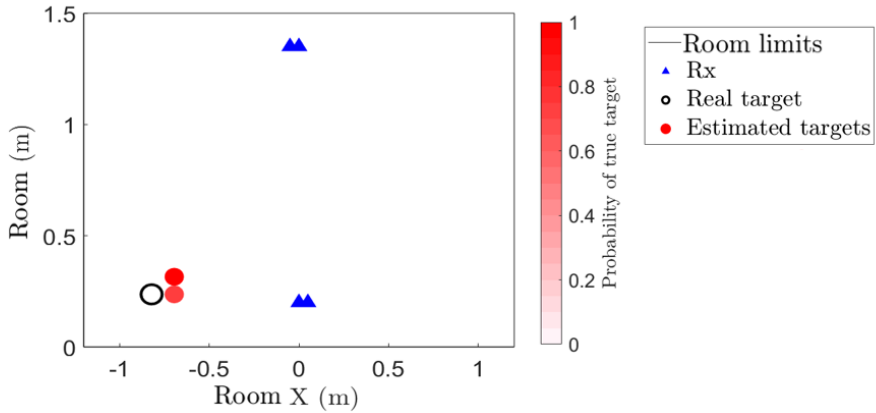


Figure 5.4: Localization of breathing person in position A (measurement 5) (X,Y) cut

5

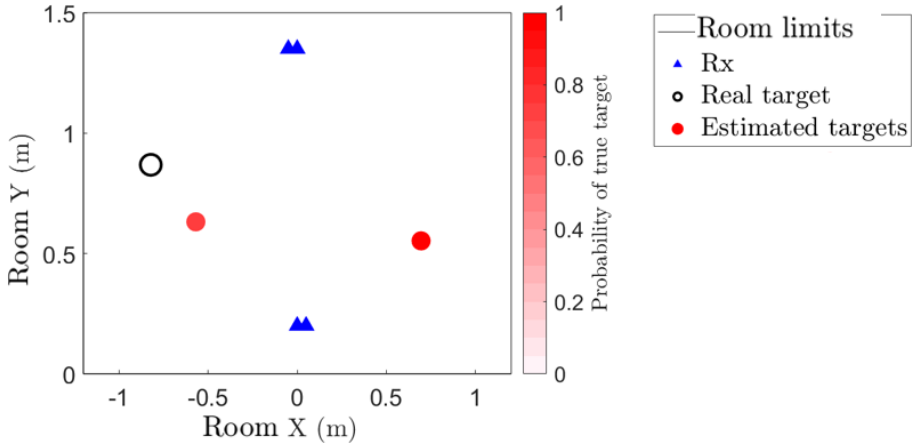


Figure 5.5: Localization of breathing person in position B (measurement 3) (X,Y) cut

- With a smaller amount of false alarms, less ghost targets appear. This can be observed in measurement 4 particularly, where, as opposed to others, almost no false alarms appear.
- The localization RMSE values obtained in the measurements can be high, up to 23cm. However, as the number of FA decreases, localization RMSE can be of 6cm or 15cm. The algorithm can be considered to accurately locate targets when the output of the detection of a real target is complete, or missing one detection.

Therefore, the main problem observed in these measurements are not the detection and location accuracy of the real target present in the environment, but rather discarding false alarms and thus preventing the appearance of ghost targets.

## 2. RESULT EVALUATION FOR TWO-PEOPLE SCENARIO

5 measurements in which 2 targets are present in positions A and B simultaneously have been evaluated. In Table C.1, these are labeled 8-12.

As an example of the results for a measurement of two people breathing in position A and B, in Figure 5.6 measurement 9 is presented.

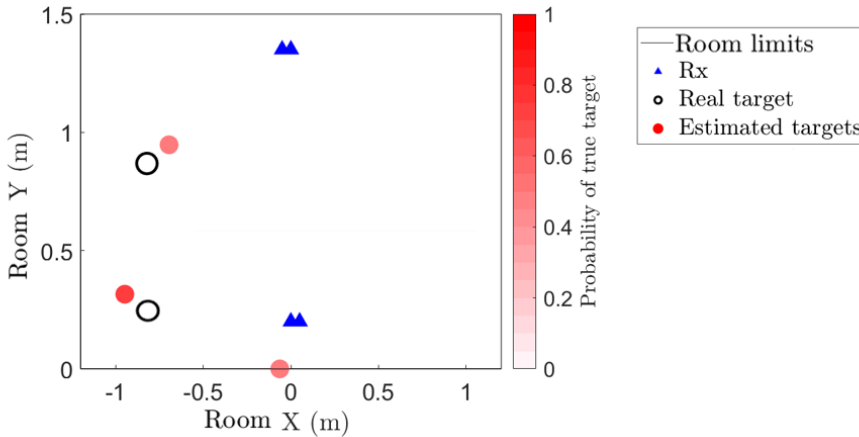


Figure 5.6: Localization of breathing people in position AB in anechoic chamber (X,Y) cut. Measurement 9

As can be observed in Table C.1 in Annex C, values for  $P_{fa}$  for single target scenarios range between 0.018 - 0.022 for monostatic radars and 0.022-0.025 for bistatic radars.

- PD has decreased for double-target scenarios. Bistatic radars seem to have more uniform detection capabilities, whereas a difference can be observed in between the monostatic radar in the back (almost all had 1 detection) vs the monostatic radar in the front, which could detect 2 targets.
- The ranging accuracy of the detected targets is comparable to that of the single-target scenario. As for the number of false alarms, even if, again up to 2 false alarms are observed, in more measurements than not, the values range between 0-1.
- For the association block, the final number of targets is almost always found to be 2, with comparable localization RMSE values to that of the single-target scenarios. This is consistent with the fact that less false alarms appear in the detections.
- On average, 1 target is missed in the detections, and 1 ghost target appears.

### 5.1.4. COMPARISON BETWEEN THE EXPERIMENTAL MEASUREMENTS AND THE SIMULATIONS IN THE ANECHOIC CHAMBER

As can be observed in the discussion of the experiments, the results fall within the range of the resulting metrics found in the Monte Carlo simulations.

- For single target scenarios, the same high detection probabilities are observed in both measurements and simulations. In two-target measurements, a drop in the detection capabilities was noted, consistent with the simulation, especially for monostatic radars. This would indicate that monostatic radars have more problem observing the targets from specific angles, and that targets are more likely to be occluded.
- The experimentally measured ranging error is higher than that of the simulations. However, it is still considered to be acceptable given that the radar range resolution is of 30cm. Moreover, bistatic RCS could not be accurately modelled because of lack of literature, and a monostatic assumption was made. The difference could also be attributed to a measurement error of the real distances to the target, as sequential people stepped in and out of the anechoic chamber for this batch of measurements.
- For all scenarios, the average number of false alarms found in the simulation can be observed to be in the range of the experiments, with a decrease in number of false alarms for multiple targets while 2D-CFAR  $P_{fa}$  remains in the same range.
- In the association block, the average number of targets found in the Monte Carlo simulations is consistent in the measurements, especially noting the appearance of up to 0.54 ghost targets in single-person scenarios, and of 0.74 in two-people measurements. The same remark is made for missed targets, with a low 0.18 number of misses in single target scenarios, but a rather higher 1.08 in double target scenarios.
- Finally, as for localization RMSE, the simulation average seems to be lower than the range of error found in the measurements. That is, errors in the range of 6 - 23 cm have been found, whereas the simulations average at 4cm for single targets and higher, up to 7.3 for double targets. This can be attributed to the fact that measurements presented higher ranging error in the detection, particularly bistatic radars.

Overall, it can be said that the observation of the scene from multiple focus points enhances the detection capabilities w.r.t monostatic radar systems, particularly for multiple-target scenarios, as monostatic radars observe a decrease in detection.

The detection algorithm is capable of properly identifying the human in the environment in all 4 radars. The performance of the 2D-CFAR algorithm plays a major role in determining which ranges and frequencies are identified in each target. Therefore, the parameter of 2D-CFAR  $P_{fa}$  highly influences the performance of the detector.

Finally, the association algorithm is capable of identifying the correct hypothesis, and fusing the correct detections from the receivers. However, it is sensitive to PD loss and FA in the detections, providing ghost targets and missed targets.

## 5.2. MEASUREMENT SETUP AND CIR SIMULATION COMPARISON IN-VEHICLE

After evaluating the performance of the measurements and simulations in an ideal non-reflective scenario, a more challenging environment is evaluated. In this case, given the fact that the use-case of this thesis is in-vehicle localization, the measurements are conducted inside a vehicle provided by NXP. The simulations attempt to recreate the environment by placing the boards and the targets in similar positions as the measurements, together with static reflective objects simulating the walls and ceiling of the car, with which multipath echos are generated using the proposed framework in Chapter 3.

Both simulated CIR data and measured CIR data are processed with the defined algorithm and compared in the following sections.

In Table 5.7, the positions of the 6 UWB radar boards are defined. As mentioned in Chapter 3.1, 3 boards will be placed in the frontal part of the car, illuminating the scene from the front, and 3 other boards will be placed in the ceiling of the back-seat.

For the simulations, the same positions will be used to generate the CIR radar data. This setup has been drawn in Figure 5.7 for reference.

Board	[x,y,z] (m)	Frequency (GHz)
Tx1	[0.05,0.2,0]	6.5
Tx2	[-0.05,1.23,-0.15]	7.5
Rx1 mono	[0,0.2,0]	6.5
Rx1 bi	[0.05,1.23,-0.15]	6.5
Rx2 mono	[0,1.23,-0.15]	7.5
Rx2bi	[-0.05,0.2,0]	7.5

Table 5.7: Board configuration for in-car measurements

Various people are placed in the occupancy areas A and B, both individually and together at the same time. Table 5.8 shows the coordinates corresponding to the defined targets A and B, and in Table 5.9, the human occupancy distribution for the human targets in this environment is defined.

Target	Coordinates (m)
Coordinates pos. A	[-0.5, 0.2, -0.4]
Coordinates pos. B	[-0.5, 0.8, -0.4]

Table 5.8: Human position coordinates in vehicle

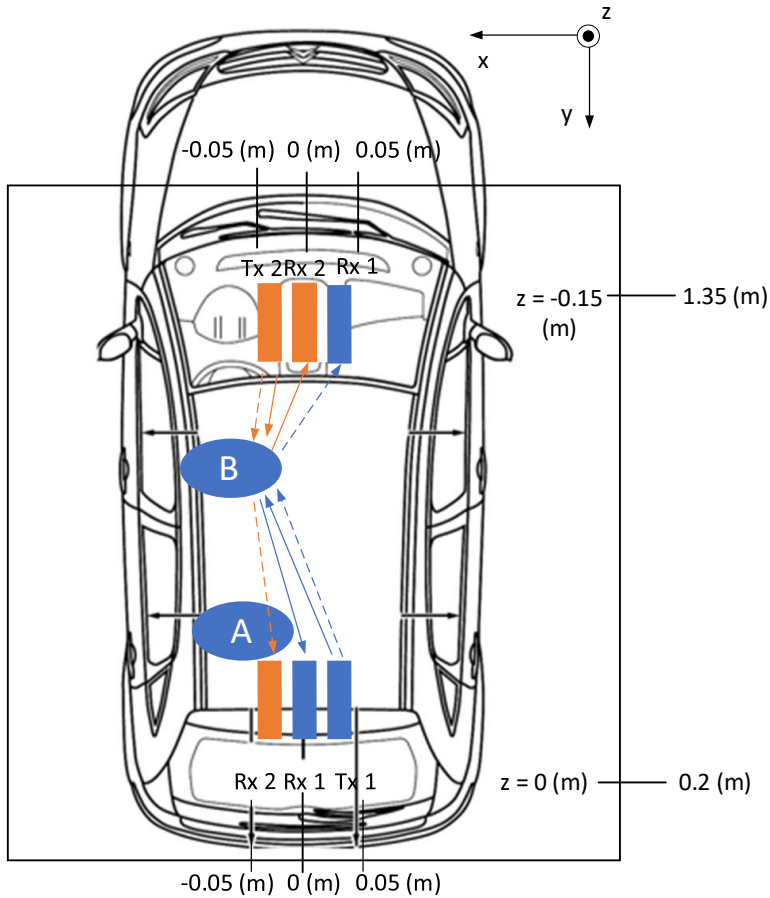


Figure 5.7: Schematic of board positions in car measurements, where A and B represent the evaluated positions for targets in the car.

Scenario	A	B
1	X	O
2	O	X
3	X	X

Table 5.9: Human-occupancy distribution in vehicle

As for the processing of the measurements, the same values defined for the algorithm parameters found in Table 5.4 for the ideal scenario are used.

### 5.2.1. PERFORMANCE EVALUATION WITH MONTE CARLO SIMULATIONS OF CIR RADAR DATA IN-VEHICLE

Similarly as was done in the previous section 5.1, a set of 100 Monte Carlo simulations of CIR radar data is created using the proposed framework to evaluate the performance of the defined setup in a statistical manner.

The variables for the breathing frequency  $f_b$  and the chest displacement  $m_b$  are randomly sampled in each repetition from a uniformly distributed range of values which are defined in Table 5.5, and a constant level of SNR of 10 dB is also used.

The simulation is made with the virtual radar boards and targets placed in the same locations as in the NXP vehicle as seen in Tables 5.7 and 5.8. The different occupancy scenarios evaluated follow those defined in Table 5.9.

The CIR radar data simulations include the effect of multipath to model the various returns that the signal will have in the vehicle. As explained in Chapter 3.2, the static objects on which the human echos rebound are modelled as flat PEC surfaces.

For this set of Monte Carlo simulations, an assumption was made that the car environment could be modelled using the following flat PEC positions, defined in Table 5.10.

Flat PEC	Coordinates (m)	Simulated size ( $m^2$ )
PEC 1	[-0.8, 0.2, -0.5]	2
PEC 2	[0, 0.2, 0]	2
PEC 3	[0.8, 0.2, -0.5]	2

Table 5.10: Positions of simulated flat PEC planes used to emulate static objects such as walls or ceiling in which echos rebound and form multipath.

The results for the performance metrics obtained after considering all 100 Monte Carlo simulations defined for each of the occupancy scenarios defined in Table 5.9 ('ID' on the 1st column), can be seen on Table 5.11. The 2D-CFAR  $P_{fa}$  values used were of 5e-3 and 4e-3 for monostatic and bistatic radar respectively.

ID	PD		N FA		Range Error (cm)		N Target	N Ghost	N Miss	Loc Error (cm)
	Mono	Bi	Mono	Bi	Mono	Bi				
1	0.51	1	0.55	0.83	4.6	3.3	1.63	1.06	0.47	5
2	0.52	1	1.28	1.49	2.4	2.5	2.06	1.11	0.38	8
3	0.33	0.89	1.11	0.83	3.6	5	2.22	1.05	1.21	[10,8]

Table 5.11: Results of Monte Carlo simulations where Scenario indicates the type of scenario simulated as seen on Table 5.9 and performance metrics are shown for each of them.

### 5.2.2. CONCLUSIONS ON THE ANALYSIS OF THE MONTE CARLO SIMULATION RESULTS

A few things should be noted.

- Monostatic PD presents a noticeable low value of 51% and 52% for single target scenarios, and even worse, of 33% for double targets. This can directly be linked to the fact that the back monostatic radar, Rx monostatic 1, positioned looking downwards, observes the enhancement of the chest as this moves almost orthogonally to the radar LoS. This points towards the fact that targets in the seats would be hard to observe with solely a monostatic radar in the back of the car. In multiple target scenarios, again, detection probabilities drop. This is consistent with the results of the ideal environment without multipath.
- Range accuracy has decreased with respect to the ideal environment.
- As for the average number of false alarms, over 1 false alarm is observed in every receiver, particularly in single-target environments.
- Over 1 ghost target can be observed in each single-person simulation, and up to 0.47 missed targets are observed. Moreover, in double target scenarios, the number of missed targets escalates to 1.2 targets on average.
- The location RMSE of the correctly detected and localized targets for scenarios 1 and 2 has values of around 5-8cm, and is higher for double targets, with 10cm.

### 5.2.3. MEASUREMENTS IN VEHICLE

Measurements are taken at the NXP facilities of the High Tech Campus in Eindhoven. A test-car is used to mount the setup in the positions described in Table 5.7. In Figure 5.8, a picture of the boards mounted in the vehicle can be seen. A limited amount of 10 measurements is taken in the car for processing. In Annex D, a comprehensive analysis of the processing results for each of the measurements is provided, following the defined performance metrics.

#### 1. RESULT EVALUATION FOR SINGLE PERSON MEASUREMENTS

The car has 5 seats available. Single-person measurements are taken in both the driver seat and the back-left seat. The details of the processing of various measurements for single-target scenarios have been noted in Table D.1 in Annex D for measurement indexes 27, 28, 30, 31, 34, 35.

As can be observed, the range of the 2D-CFAR  $P_{fa}$  used was of 0.004 - 0.01 for monostatic radar and 0.003-0.018 for bistatic radar. Varying these values has a high impact on the results, as already noted.

As an example of results of a single-person breathing in positions A and B, measurements 27 and 34 are shown in Figures 5.9 and 5.10 respectively.

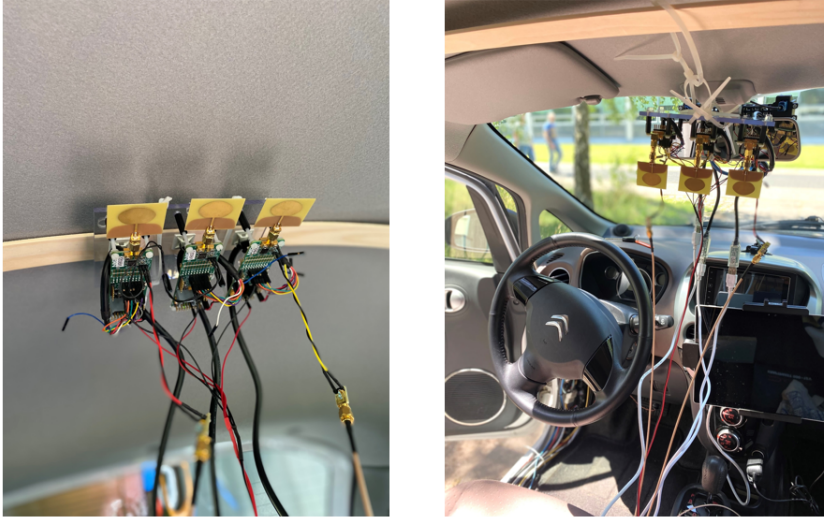


Figure 5.8: (Left): Tx1 , Rx monostatic 1, Rx bistatic 2 in vehicle measurements placed in the back. Omnidirectional antennas facing downwards. (Right): Tx2 , Rx monostatic 2, Rx bistatic 1 in vehicle measurements placed in the front. Omnidirectional antennas facing forward.

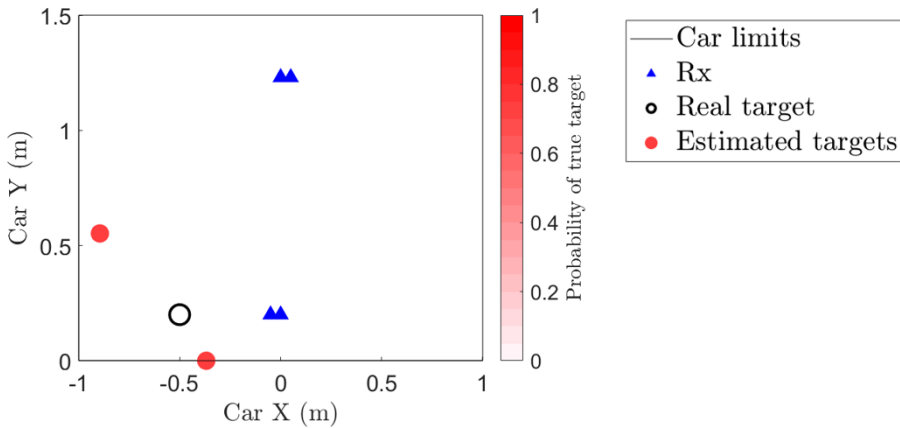


Figure 5.9: Localization of breathing person in position A (X,Y) cut (measurement 27)

From both these figures and the analysis attached in Annex D, it can be observed that:

- All radars are capable of detecting the human presence in the environment with ranging accuracy of less than 10 cm in accurate measurements. However, the position of the monostatic back-radar w.r.t. the chest displacement of the targets worsens detection for monostatic radar.

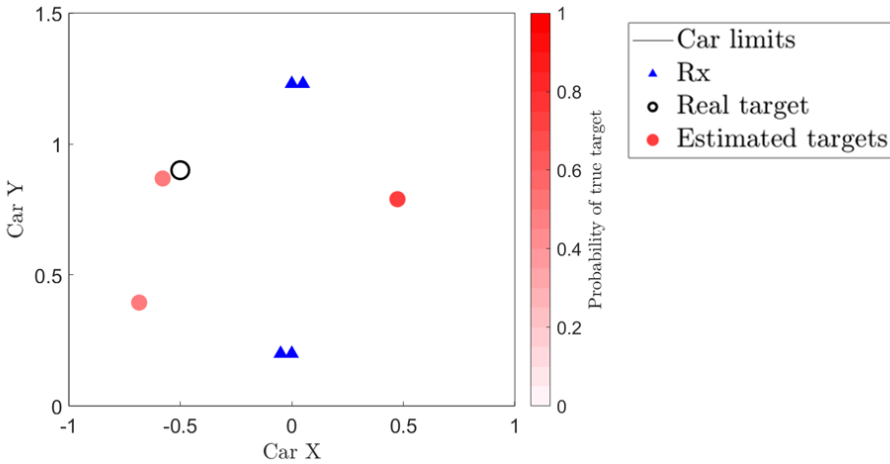


Figure 5.10: Localization of breathing person in position B (X,Y) cut (measurement 34)

5

- Up to 3 false alarms are detected in a received data matrix, depending on the variation of the value of 2D-CFAR  $P_{fa}$ . Bistatic radar presents a lower number of false alarms than monostatic radar.
- After association, up to 2 targets are localized in the environment, with up to 2 ghost targets in one measurement.
- Good localization accuracy of 16cm can still be achieved when most radars are capable of detecting the target with ranging error lower than 10cm.

Overall, the losses in PD, and increased amount of false alarms have compromised the results by introducing various ghost targets, even if the real targets can still be located, introducing a location RMSE in the range of 16-29 cm.

## 2. RESULT EVALUATION FOR TWO-PEOPLE MEASUREMENTS

The details of the processing of various measurements for double-target scenarios have been noted in Table D.1 for measurement indexes 40, 41, 44, 47. The range of 2D-CFAR  $P_{fa}$  used was of 0.005 - 0.015 for monostatic radar and 0.008-0.019 for bistatic radar. As an example of results of a double-person breathing in positions A and B, measurement 44 is shown in Figure 5.11.

Observing the processing of the measurements for two-people breathing simultaneously inside a vehicle, the following can be noted.

- Firstly, detection capabilities have dropped with respect to single-target scenarios. Mostly Rx monostatic 1 fails to detect both targets.

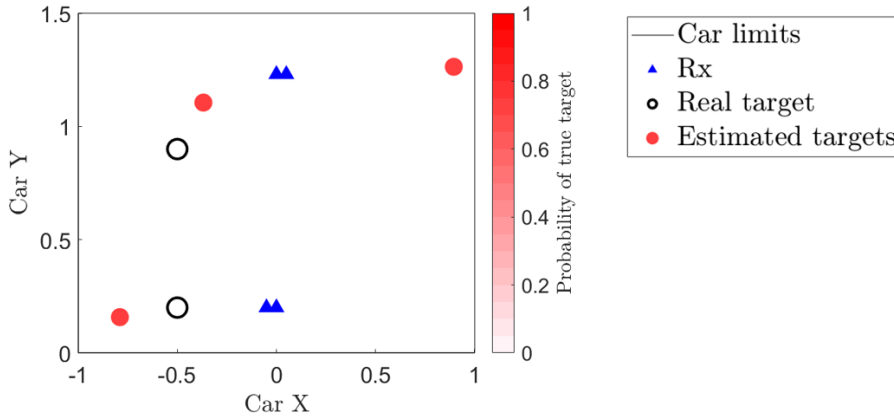


Figure 5.11: Localization of breathing people in positions A and B (X,Y) cut (measurement 44)

- The ranging accuracy is similar to that of the single-target measurements. For some it is very good, but for others it decreases. As already noticed, the general variability and inconsistency of the measurement makes a general assessment difficult.
- The number of false alarms is lower than for single-target measurements. However, the number of identified ghost targets has increased, with almost all measurements being affected by at least 1.
- Finally, localization RMSE is considered to be accurate, of less than 16cm in some cases, except for those measurements where not enough ranges were detected, and targets could not be located properly.

#### 5.2.4. COMPARISON BETWEEN THE EXPERIMENTAL MEASUREMENTS AND THE SIMULATIONS IN THE VEHICLE

As was concluded in the comparison between the simulations and the measurements in the ideal environment, the measurement results fall within the range of expected values found with the simulation results. More importantly, the same pitfalls can be observed.

- Firstly, the poor detection of the monostatic radar placed in the back of the car is observed in both measurements and simulation. This can be attributed to the position of the radar w.r.t. the target. Secondly, a drop in PD is observed for all radars as more targets are introduced in the scene, but significantly more for monostatic radars, which suffer from target occlusion.
- The increase in the total number of false alarms in the different receivers w.r.t an ideal environment can also be concluded to be consistent throughout the simulations and the measurements.

- The number of ghost targets has increased w.r.t. ideal environments in both simulations and experimental measurements.
- Localization RMSE oscillates greatly for all environments, since its accuracy drops as missed detections are introduced in the measurement, and false alarms in the detections increase. This is consistent in the simulations. For some experimental measurements, localization RMSE of 16cm can be obtained for single targets, and up to 9cm for double targets.

### 5.3. CONCLUSIONS ON EXPERIMENTAL VALIDATION OF THE MEASUREMENTS AND THE EFFECT OF MULTIPATH

After evaluating the experiments conducted both in an ideal environment and in a vehicle, the complexity of detecting and localising an unknown number of people can be seen. Overall, the results match the expectations, and reinforce some of the assumptions made.

5

- Single targets can be detected by all radars in the network, even in multipath environments. Even if high-energy echoes due to reflections with static objects are present, these can be discarded as our application limits the possible ranges in which the targets can be found to no more than 3-meter round-trip delays. Therefore, multipath does not seem to significantly affect PD.
- When multiple targets are introduced in a scene, PD consistently drops, as some humans in the environment might occlude others. This is especially noticeable in monostatic radars. The targets in the scene present similar bistatic range delays, indicating that targets in the same range can be separated with the distinction of their breathing frequency in most cases.
- The importance of the correct positioning of the boards is shown, particularly for monostatic radars. Bistatic radars present a more uniform detection performance, especially in scenarios with multiple people.
- An increased detection range error is observed in multipath environments, which negatively affects the performance of the association algorithm.
- Every radar Rx board will introduce false alarms. The number of false alarms detected increased in the multipath environment, up to 1.49 false alarms in single-target scenarios and 1.11 in double-target scenarios. However, the detector parameters play a key role in the number of false alarms that appear, as well as in the probability of detection. This puts forward the need for further parameter optimization in the detection algorithm.
- When detection is ideal, namely when it has both good ranging and breathing frequency accuracy, with high PD and a low number of false alarms, the association algorithm is capable of determining the correct hypothesis of combination between detections from multiple receivers corresponding to real targets, and not false alarms.

- As the vehicle environment simulated presents a higher number of false alarms and lower PD, and increased range error, the number of missed targets increases with respect to the anechoic chamber environment, from values around 0.1 in ideal environments to around 0.4 in multipath environments for single targets and from 1 target up to an average of 1.2 targets in double target scenarios. Similarly for ghost targets, from 0.42 to 0.74 ghost targets appear depending on the number of people in ideal environments and up to 1.1 for the car. The degradation of the association performance, therefore, is highly correlated to the loss of accuracy in the detection matrices and thus to the introduction of more people in the scene and the introduction of multipath.

In the following section, different scenarios are evaluated using Monte Carlo simulations in an attempt to improve the obtained results in environments that could not be replicated with experimental measurements at this stage.

## 5.4. REPOSITIONING OF THE BOARDS VIA SIMULATION

In this section, various scenarios are evaluated based on possible improvements of the current setup results for the vehicle environment.

5

### 5.4.1. SEPARATION OF THE BOARDS THAT FORM THE ANCHORS FOR INCREASED SPATIAL DIVERSITY

It has been observed that the association algorithm is sensitive to poor detection, a high number of false alarms and increased ranging error. This could be attributed to the computation of the cost matrix, particularly the range cost defined in Chapter 2. This cost calculation directly depends on the localization accuracy for a given hypothesis.

With the current positioning of the boards, the detected ranges, particularly for bistatic radar, are rather similar in all the targets that can be simulated in a vehicle. Therefore, a proposal is made to separate the boards that form the anchors in an attempt to gain spatial separation, and improve localization, and thus the performance of the association algorithm.

By spacing the boards, detection parameters are not expected to change significantly, but rather the performance of the association block.

The environment of the car evaluated in the previous section is defined as a starting point. Therefore, boards in the anchors are spaced 15 cm outwards (x direction) from the positions defined in Table 5.7. These new values are defined in 5.12.

A set of 100 Monte Carlo simulations is evaluated for a double-target scenario, with the coordinates of the people sitting in the car, as previously defined in Table 5.8. A double-target scenario is evaluated, as this is the most constrained environment in terms of detection, and a realistic idea of the improvement of the board separation is wanted. In Table 5.13, the performance metrics for the Monte Carlo simulations for board separation are defined in the first row (labelled as 'Sep'), and the results already discussed for the boards in the original position are attached in the row below (labelled as 'Prev').

Board	[x,y,z] (m)	Frequency (GHz)
Tx1	[ 0.2, 0.2, 0 ]	6.5
Tx2	[-0.2,1.23,-0.15]	7.5
Rx1 mono	[ 0 , 0.2, 0 ]	6.5
Rx1 bi	[ 0.2, 1.23,-0.15]	6.5
Rx2 mono	[ 0 , 1.23,-0.15]	7.5
Rx2bi	[-0.2, 0.2, 0 ]	7.5

Table 5.12: Board positioning for simulation of setup with increased spatial diversity w.r.t. simulations in vehicle performed so far.

ID	PD		N FA		Range Error (cm)		N Target	N Ghost	N Miss	Loc Error (cm)
	Mono	Bi	Mono	Bi	Mono	Bi				
<b>Sep</b>	0.37	0.86	1.13	0.65	2	4.9	2.01	0.25	0.86	[4.8,1.6]
<b>Prev</b>	0.33	0.89	1.11	0.83	3.6	5	2.22	1.05	1.21	[10,8]

Table 5.13: Result of Monte Carlo Simulations for board re-positioning for added spatial diversity ('Sep'), vs results presented for non-separated boards in section 5.2 ('Prev'), both with double targets placed in occupancy areas A and B.

As can be observed, PD is maintained, which was to be expected, since detection happens for each Rx board individually. However, looking at the association block metrics it can be seen that the number of identified ghost targets has dropped to 0.25 from over 1, and the number of missed targets has also been reduced to 0.86, while improving RMSE localization error.

Therefore, it can be concluded that the added range separation introduced by the spacing of the boards leads to better localization, and therefore more accurate cost-matrix computation and association.

Given the fact that such a setup can be permanently mounted in a vehicle, spacing the antennas should not be a problem, as these can be integrated in the ceiling of the vehicle.

#### 5.4.2. BOARD LOWERING FOR INCREASED PROBABILITY OF DETECTION

Another way of improving localization accuracy besides range separation would be to ensure that the maximum number of detections are available for the association step, that is, increasing PD.

In the car environment, PD was found to be extremely low for the monostatic radar placed in the back, due to its position w.r.t the target's chest displacement. Therefore, a proposal is made to lower the back-radars and place them behind the center back-seat, essentially lowering the z coordinate by 40cm and also the y coordinate by 15cm w.r.t the positions defined in Table 5.7. The final board positions thus are defined in Table 5.14.

Board	[x,y,z] (m)	Frequency (GHz)
Tx1	[0.05,0.05,-0.4]	6.5
Tx2	[-0.2,1.23,-0.15]	7.5
Rx1 mono	[0,0.05,-0.4]	6.5
Rx1 bi	[0.05,1.23,-0.15]	6.5
Rx2 mono	[0,1.23,-0.15]	7.5
Rx2bi	[-0.05,0.05,-0.4]	7.5

Table 5.14: Board configuration for in-car measurements after lowering anchor 1 for increased PD

As was mentioned in numerous studies such as in [29], it is possible to detect vital signs from the back using UWB radar. Therefore, with these positions, detection of targets is expected to improve, as was the case for the ideal environment in which boards were on the same plane as the human chests. Higher PD should in its turn result in an improvement w.r.t. the number of missed targets, but ghost targets are expected to increase, because of the increased number of detections used as input in the association algorithm.

A set of 100 Monte Carlo simulations is evaluated for a double-target scenario, with the coordinates of the people sitting in the car, as previously defined in Table 5.8. A double-target scenario is also picked for the study of this proposed topology.

In Table 5.15, the performance metrics for the Monte Carlo simulations for lowering the boards on the back are defined in the first row (labelled as 'Low'), and for comparison, the results already discussed for the boards in the original position (Table 5.7) are attached below (labelled as 'Prev').

ID	PD		N FA		Range Error (cm)		N Target	N Ghost	N Miss	Loc Error (cm)
	Mono	Bi	Mono	Bi	Mono	Bi				
<b>Low</b>	0.75	0.97	2.17	0.94	2.8	2.7	2.69	1.38	0.92	[7.6,2.9]
<b>Prev</b>	0.33	0.89	1.11	0.83	3.6	5	2.22	1.05	1.21	[10,8]

Table 5.15: Result of Monte Carlo Simulations for lowering boards in the back for increased PD ('Low'), vs results presented for boards placed in the ceiling as defined in section 5.2 ('Prev'), both with double targets placed in occupancy areas A and B.

Lowering the anchor automatically increased PD, as well as the number of false alarms found in the monostatic radars. The average number of missed targets has lowered from 1.21 to 0.92, and the number of ghost targets has increased from 1.05 to 1.38. This was to be expected, as an increased number of hypothesis resulted in a higher number of associated targets, and thus ghost targets. Localization RMSE decreases. This is a direct result of including more ranges in the localization algorithm (higher PD).

### 5.4.3. CONCLUSIONS ON THE PROPOSAL OF NEW SETUPS

It can be concluded that the proposed setup tested in the vehicle with measurements can be improved. By spacing the boards outwards, the range separation is improved and the association algorithm is capable of localizing the targets while decreasing the number of ghost targets greatly and also the number of missed targets.

Moreover, lowering the boards placed on the ceiling will present an increase in PD, which, in turn, will lower the number of missed targets.

These results have not been verified experimentally. However, these radar topologies should be considered for future tests in a vehicle.

## 5.5. COMPARING RESULTS TO SOTA

In this section, the results obtained are compared to SOTA.

Firstly, other papers that focus on multiple-people localization are observed. The solutions proposed are based on SIMO/MIMO radars [9], [43] where targets are localized using angular estimation with the antenna arrays. In this thesis, however, localization is performed with a multistatic network of radars, therefore comparison cannot be easily done.

On a different note, in [48], a network of monostatic OFDM radars is used to detect 2 trihedrals in an anechoic chamber. Even though the specifics of the detections obtained are not discussed, the results yield high RMSE values of 1.72m and 4.54m. Therefore, the results obtained in this thesis for localization seems to outperform those presented in the literature.

Also, in [49], a similar association approach is considered, including breathing frequency estimation. It is concluded that as the number of targets increases, particularly under the presence of false alarms, the number of ambiguities becomes very large, which is the same conclusion that has been extracted from this work. However, the aforementioned association algorithm did not account for the possibility of missed detections in the detection stage, thus other aspects of the association algorithm cannot be directly compared either.

Secondly, the defined radar signature model for human breathing is also considered. In literature it is simulated as a static RCS amplitude which presents a sinusoidal phase displacement due to the motion of the chest. However, it has been discussed in Chapter 2, that accounting for the amplitude changes as the human RCS increases and decreases with the chest movement yielded a more accurate representation of the measured data.

Finally, as in [48], distributed monostatic networks can be used to localize targets in an environment. However, it can be observed in the results that the introduction of bistatic radar in the network increases the detection capabilities w.r.t. only monostatic radars. Higher PD values will translate into less missed targets after association, as has been studied. Therefore, introducing bistatic radar presents an improvement in detection.

## 5.6. CONCLUSIONS OF THE EXPERIMENTAL VALIDATION

In this section, the conclusions are given for the experimental result testing of the proposed algorithm.

Firstly, it can be concluded that localization of multiple people using a network of multistatic UWB radar is possible with acceptable performances with localization RMSE in the order of 9cm in ideal non-reflective scenarios, and of 16cm in the vehicle environment, with a maximum of 2 people tested.

The detection of targets is decentralized, meaning that detection in one receiver does not depend on the other receivers in the network. However, the joint output of the different detection blocks will impact the final association algorithm. As PD lowers, more targets are missed in the association algorithm and ghost targets appear. On the same line, as false alarms appear in the detection matrices more ghost targets appear and more targets cannot be located. This is especially noticeable in multipath environments, where the number of false alarms is higher, and detection range error increases.

To overcome this, a new setup is proposed in which the boards have been separated to gain spatial diversity and thus overcome range ambiguities in the localization algorithm, a critical step in the cost matrix computation for the association. By increasing the distances between the boards, the number of ghost targets is reduced from 1 to 0.25 in double-target scenarios, and missed targets present a decrease from 1.2 to 0.86 while reducing localization RMSE.

Finally, the positioning of the boards w.r.t. the target breathing motion is proven to be critical, particularly for monostatic radars. By placing the anchor where chest displacement is more visible to the radar, PD is increased and so is the performance of the association. That is, the number of missed targets is decreased.

Hence, the advantages of using an UWB radar network to illuminate the scene from multiple focus points are proven w.r.t. using only monostatic radars or MIMO radars. These are, the more uniform detection capabilities presented by bistatic radars, and the possibility to re-position the boards to enhance spatial diversity and thus improve localization.



# 6

## CONCLUSIONS AND FUTURE WORK

*In this Chapter, a summary of the thesis is presented and the conclusions are discussed. Finally, different proposals for future work are put forward.*

### 6.1. CONCLUSIONS

Starting from 2022, Euro NCAP will reward manufacturers that offer CPD as standard. Moreover, seatbelt-reminder detectors are based on pressure sensors triggered by non-human and human targets alike. This thesis aims to present a wireless solution for CPD and seatbelt-reminder by investigating the complex problem of multiple people detection and localization in multipath scenarios, particularly a vehicle, based on vital signs detection with a network of UWB radar.

Vital signs estimation using UWB radar has been investigated in the literature. However, most studies rely on assumptions that are incompatible with our system constraints. Namely, human presence is assumed a priori, or human position and/or number of humans was known. Moreover, the localization of multiple targets in a particular scenario had been investigated with SIMO/MIMO radars using angular estimation. However, the possibility to use a network of UWB radars to illuminate the targets from different positions has not been considered in detail in the literature.

The main contributions of this thesis can be summarized as follows:

- A novel model for the radar signature of a breathing human was derived, and it was concluded, after a qualitative comparison with radar measurements, that it can be used to accurately model the breathing motion as seen by a radar.
- The development of a detection algorithm capable of identifying an unknown number of human targets with improved ranging accuracy w.r.t. literature, based on vital-sign detection. The output of this detection algorithm is a detections matrix containing the range and estimated breathing frequency information of the targets.

- The development of an association algorithm to centrally fuse the detection matrices from the different radar receivers in the network using machine-learning based cost-matrix computation, and thus be able to identify the correct combinations for detections from different receivers to localize the real targets in the defined environment.
- The design and construction of a network of multistatic UWB radar based on NXP's Ranger4 boards to capture the radar data matrices to be processed.
- The proposal of a simulation framework to generate configurable CIR radar data matrices to evaluate the performance of the proposed setup in various environments via the generation of Monte Carlo simulations.
- The validation of the proposed algorithm for detection and association with both experimental data measured in ideal scenarios and a vehicle, and in simulated radar data through the study of the defined performance metrics.
- The investigation of how detection and localization can be improved based on the proposal of different radar topologies and a study of the results obtained using simulated data.

## 6

After evaluating the results, it can be concluded that localization of multiple people using a network of multistatic UWB radar is possible with acceptable performances with localization RMSE in the order of 16cm for the initially proposed radar setup inside the vehicle, after testing a maximum of 2 people.

Specifically, it was demonstrated that the network increases the probability of detection w.r.t. SOTA by introducing bistatic radars and by illuminating the scene from various focus points. This can be observed in the results, namely as the consistent PD obtained for bistatic radar w.r.t. monostatic radar, as monostatic radar's detection capabilities are highly dependant on the radar's position w.r.t. human chest movement, and decrease rapidly as more people are introduced in the scene.

It was also noted that, particularly in multipath environments where detection presented more false alarms and higher range errors w.r.t. ideal environments, the association algorithm showed an increased number of ghost targets and missed targets throughout the experimental measurement results and on the performance metrics of Monte Carlo simulations with the proposed radar topology in Chapter 3.

To improve this, it was demonstrated by means of evaluating a set of Monte Carlo simulations with different radar topologies, that increasing the probability of detection by re-positioning the anchors inside of the vehicle led to a decrease in the number of missed targets. Moreover, increasing spatial diversity between the boards made the association block more robust against false alarms and missed detections in the detection block, by significantly reducing the average number of localized ghost targets and missed targets.

The results and conclusions of this thesis are being written for an IEEE publication.

## 6.2. FUTURE WORK

In this section, future work is proposed in order to continue the investigation.

- The low tolerance of the association block for poor detection and false alarms calls for an improvement in the detection block. It has been studied that various parameters in the algorithm have an important impact on the overall detection performance. Therefore, an optimization of such parameters is proposed to enhance detection capabilities of the proposed processing block. That is, parallelly running the algorithm using various values for 2D-CFAR  $P_{fa}$  in order to find an optimal point, or recursively varying this value depending on different factor such as the size of the detection matrices obtained, the signal SNR, etc.
- Testing of the newly proposed network topologies based on the results of Monte Carlo simulations can be done inside a vehicle in order to corroborate the conclusions extracted from the simulations.
- In order to improve the assessment of the algorithm, measurements can be taken by tracking the ground-truth of the vital signs of the humans, to facilitate the evaluation of measurements.
- The evaluation of experimental measurements in a vehicle where human targets are moving, for example, moving their hands, reading a book, scrolling on a phone, talking, etc. The defined processing pipeline includes a classification stage in which moving people can be detected without vital-sign information. However, this has not been deeply investigated in this thesis. Therefore, it would be interesting to test the proposed algorithm performance in this case.
- The measurement setup requires improvement. Currently, the prototype is based on the combination of Ranger4 boards. However, by using Ranger5 boards, which already include Tx/Rx separation, the stability of the connection is expected to improve as the number of boards necessary to replicate the same measurements would be reduced.
- In the development of the radar signature model for human breathing, an interesting new way to extract vital signs periodicity was found. In Equation 2.5 it was derived how the Doppler frequency is a result of the displacement of the chest through time. In [2], the vital signs information is found using a spectrogram and image processing techniques to observe the evolution of this  $f_d$  value. However, it was found that simply by extracting the position of the maximum value of the spectrogram columns,  $f_d$  is easily identified after applying signal smoothing techniques.

This has not been used in this project due to lack of time, however it puts forward an interesting new proposal to continue to improve vital signs detection.



# BIBLIOGRAPHY

- [1] Yuqing Li. “Vital Sign Monitoring using Doppler Signal Decomposition”. In: *MS3 Group MS3 Thesis* (Aug. 2020). DOI: <http://resolver.tudelft.nl/uuid:171a04f3-5745-4eff-8a06-c10e4aafce45>.
- [2] Yichuang Han. “Contactless Vital Signs Monitoring via Radar Sensing for Sleep Applications”. In: *MS3 group MS3 Thesis* (Aug. 2021). DOI: <http://resolver.tudelft.nl/uuid:b19eae93-23b9-46e6-b2ef-a21cbb9d6d87>.
- [3] Xinming Huang et al. “Real-time non-contact infant respiratory monitoring using UWB radar”. In: *2015 IEEE 16th International Conference on Communication Technology (ICCT)*. 2015, pp. 493–496. DOI: [10.1109/ICCT.2015.7399885](https://doi.org/10.1109/ICCT.2015.7399885).
- [4] James J. McKenna and Thomas McDade. “Why babies should never sleep alone: A review of the co-sleeping controversy in relation to SIDS, bedsharing and breast feeding”. In: *Paediatric Respiratory Reviews* 6.2 (2005), pp. 134–152. ISSN: 1526-0542. DOI: <https://doi.org/10.1016/j.prrv.2005.03.006>. URL: <https://www.sciencedirect.com/science/article/pii/S1526054205000230>.
- [5] Giovanni Diraco, Alessandro Leone, and Pietro Siciliano. “A Radar-Based Smart Sensor for Unobtrusive Elderly Monitoring in Ambient Assisted Living Applications”. In: *Biosensors* 7.4 (2017). ISSN: 2079-6374. DOI: [10.3390/bios7040055](https://doi.org/10.3390/bios7040055). URL: <https://www.mdpi.com/2079-6374/7/4/55>.
- [6] Faheem Khan et al. “An Overview of Signal Processing Techniques for Remote Health Monitoring Using Impulse Radio UWB Transceiver”. In: *Sensors* 20 (Apr. 2020), p. 2479. DOI: [10.3390/s20092479](https://doi.org/10.3390/s20092479).
- [7] Yonggu Lee et al. “A Novel Non-contact Heart Rate Monitor Using Impulse-Radio Ultra-Wideband (IR-UWB) Radar Technology”. In: *Scientific Reports* 8.1 (Aug. 2018), p. 13053. ISSN: 2045-2322. DOI: [10.1038/s41598-018-31411-8](https://doi.org/10.1038/s41598-018-31411-8). URL: <https://doi.org/10.1038/s41598-018-31411-8>.
- [8] Amer Nezirovic, Alexander G. Yarovoy, and Leo P. Ligthart. “Experimental study on human being detection using UWB radar”. In: (2006), pp. 1–4. DOI: [10.1109/IRS.2006.4338133](https://doi.org/10.1109/IRS.2006.4338133).
- [9] Daniel Novák and Dušan Kocur. “Multiple static person localization based on respiratory motion detection by UWB radar”. In: *2016 26th International Conference Radioelektronika (RADIOELEKTRONIKA)*. 2016, pp. 252–257. DOI: [10.1109/RADIOELEK.2016.7477386](https://doi.org/10.1109/RADIOELEK.2016.7477386).
- [10] Euro NCAP. *Test and assessment protocol: Child Presence Detection*. <https://cdn.euroncap.com/media/64101/euro-ncap-cpd-test-and-assessment-protocol-v10.pdf>. May 2021.

- [11] “Novel signal processing method for vital sign monitoring using FMCW radar”. In: *Biomedical Signal Processing and Control* 33 (2017), pp. 335–345. ISSN: 1746-8094. DOI: <https://doi.org/10.1016/j.bspc.2016.12.008>. URL: <https://www.sciencedirect.com/science/article/pii/S1746809416302208>.
- [12] Yogesh Nijsure et al. “An Impulse Radio Ultrawideband System for Contactless Noninvasive Respiratory Monitoring”. In: *IEEE Transactions on Biomedical Engineering* 60.6 (2013), pp. 1509–1517. DOI: [10.1109/TBME.2012.2237401](https://doi.org/10.1109/TBME.2012.2237401).
- [13] NXP Semiconductors MARC ROBASZKIEWICZ. *SAVING LIVES WHEN TEMPERATURES RISE. In-cabin UWB Radar to Ensure Everyone's Out of a Parked Car*. <https://www.nxp.com/docs/en/white-paper/RADAR-CHILD-DETECTION-WP.pdf>. Jan. 2022.
- [14] Yiyi Chu et al. “Influential variables impacting the reliability of building occupancy sensor systems: A systematic review and expert survey”. In: *Science and Technology for the Built Environment* 28.2 (2022), pp. 200–220. DOI: [10.1080/23744731.2021.1993672](https://doi.org/10.1080/23744731.2021.1993672). eprint: <https://doi.org/10.1080/23744731.2021.1993672>. URL: <https://doi.org/10.1080/23744731.2021.1993672>.
- [15] Dingyang Wang, Sungwon Yoo, and Sung Ho Cho. “Experimental Comparison of IR-UWB Radar and FMCW Radar for Vital Signs”. In: *Sensors* 20 (Nov. 2020), pp. 1–22. DOI: [10.3390/s20226695](https://doi.org/10.3390/s20226695).
- [16] Heba Abdelnasser, Khaled A. Harras, and Moustafa Youssef. “UbiBreathe: A Ubiquitous Non-Invasive WiFi-Based Breathing Estimator”. In: *Proceedings of the 16th ACM International Symposium on Mobile Ad Hoc Networking and Computing. MobiHoc '15*. Hangzhou, China: Association for Computing Machinery, 2015, pp. 277–286. ISBN: 9781450334891. DOI: [10.1145/2746285.2755969](https://doi.org/10.1145/2746285.2755969). URL: <https://doi-org.tudelft.idm.oclc.org/10.1145/2746285.2755969>.
- [17] Qifan Pu et al. “Whole-Home Gesture Recognition Using Wireless Signals”. In: *Proceedings of the 19th Annual International Conference on Mobile Computing Networking. MobiCom '13*. Miami, Florida, USA: Association for Computing Machinery, 2013, pp. 27–38. ISBN: 9781450319997. DOI: [10.1145/2500423.2500436](https://doi.org/10.1145/2500423.2500436). URL: <https://doi-org.tudelft.idm.oclc.org/10.1145/2500423.2500436>.
- [18] Ming-Zher Poh, Daniel J. McDuff, and Rosalind W. Picard. “Non-contact, automated cardiac pulse measurements using video imaging and blind source separation.” In: *Opt. Express* 18.10 (May 2010), pp. 10762–10774. DOI: [10.1364/OE.18.010762](https://doi.org/10.1364/OE.18.010762). URL: <http://opg.optica.org/oe/abstract.cfm?URI=oe-18-10-10762>.
- [19] Jing Li et al. “Advanced Signal Processing for Vital Sign Extraction With Applications in UWB Radar Detection of Trapped Victims in Complex Environments”. In: *Selected Topics in Applied Earth Observations and Remote Sensing, IEEE Journal of* 7 (Mar. 2014), pp. 783–791. DOI: [10.1109/JSTARS.2013.2259801](https://doi.org/10.1109/JSTARS.2013.2259801).
- [20] Pramod Verma et al. “Analysis of clutter reduction techniques for through wall imaging in UWB range”. In: *Progress in Electromagnetics Research B* 17 (Jan. 2009), pp. 29–48. DOI: [10.2528/PIERB09060903](https://doi.org/10.2528/PIERB09060903).

- [21] Pramod Verma et al. “Analysis of clutter reduction techniques for through wall imaging in UWB range”. In: *Progress in Electromagnetics Research B* 17 (Jan. 2009), pp. 29–48. DOI: [10.2528/PIERB09060903](https://doi.org/10.2528/PIERB09060903).
- [22] Kuo-Kai Shyu et al. “Detection of Breathing and Heart Rates in UWB Radar Sensor Data Using FVPIEF-Based Two-Layer EEMD”. In: *IEEE Sensors Journal* 19.2 (2019), pp. 774–784. DOI: [10.1109/JSEN.2018.2878607](https://doi.org/10.1109/JSEN.2018.2878607).
- [23] Byeong-ho Lee et al. “Adaptive clutter suppression algorithm for human detection using IR-UWB radar”. In: *2017 IEEE SENSORS*. 2017, pp. 1–3. DOI: [10.1109/ICSENS.2017.8234016](https://doi.org/10.1109/ICSENS.2017.8234016).
- [24] Mindaugas Tumalskis. “Application of UWB radar for human respiration monitoring”. In: *BioMed 2016*. 2016.
- [25] Nir Regev and Dov Wulich. “Radar-Based, Simultaneous Human Presence Detection and Breathing Rate Estimation”. In: *Sensors* 21.10 (2021). ISSN: 1424-8220. DOI: [10.3390/s21103529](https://doi.org/10.3390/s21103529). URL: <https://www.mdpi.com/1424-8220/21/10/3529>.
- [26] Antonio Guillén, David Girbau, and R. Villarino. “Analysis of vital signs monitoring using an IR-UWB radar”. In: *Progress In Electromagnetics Research* 100 (Jan. 2010), pp. 265–284. DOI: [10.2528/PIER09120302](https://doi.org/10.2528/PIER09120302).
- [27] Kuo-Kai Shyu et al. “UWB Simultaneous Breathing and Heart Rate Detections in Driving Scenario Using Multi-Feature Alignment Two-Layer EEMD Method”. In: *IEEE Sensors Journal* 20.17 (2020), pp. 10251–10266. DOI: [10.1109/JSEN.2020.2992687](https://doi.org/10.1109/JSEN.2020.2992687).
- [28] Satish Mohanty, Karunesh Gupta, and Solomon Raju Kota. “Comparative study between VMD and EMD in bearing fault diagnosis”. In: *9th International Conference on Industrial and Information Systems, ICIIS 2014* (Feb. 2015). DOI: [10.1109/ICIINFS.2014.7036515](https://doi.org/10.1109/ICIINFS.2014.7036515).
- [29] Elliott Schires, Pantelis Georgiou, and Tor Sverre Lande. “Vital Sign Monitoring Through the Back Using an UWB Impulse Radar With Body Coupled Antennas”. In: *IEEE Transactions on Biomedical Circuits and Systems* 12.2 (2018), pp. 292–302. DOI: [10.1109/TBCAS.2018.2799322](https://doi.org/10.1109/TBCAS.2018.2799322).
- [30] Texas Instruments Lab. *IWR6843 TI-mmWave sensor*. <https://training.ti.com/mmwave-vital-signs-lab>. 2022.
- [31] Faheem Khan and Sung Ho Cho. “A Detailed Algorithm for Vital Sign Monitoring of a Stationary/Non-Stationary Human through IR-UWB Radar”. In: *Sensors* 17.2 (2017). ISSN: 1424-8220. DOI: [10.3390/s17020290](https://doi.org/10.3390/s17020290). URL: <https://www.mdpi.com/1424-8220/17/2/290>.
- [32] Jing Li et al. “Through-Wall Detection of Human Being’s Movement by UWB Radar”. In: *IEEE Geoscience and Remote Sensing Letters* 9.6 (2012), pp. 1079–1083. DOI: [10.1109/LGRS.2012.2190707](https://doi.org/10.1109/LGRS.2012.2190707).
- [33] Yanni Yang et al. “Multi-Breath: Separate Respiration Monitoring for Multiple Persons with UWB Radar”. In: *2019 IEEE 43rd Annual Computer Software and Applications Conference (COMPSAC)*. Vol. 1. 2019, pp. 840–849. DOI: [10.1109/COMPSAC.2019.00124](https://doi.org/10.1109/COMPSAC.2019.00124).

- [34] Wei-Chih Su et al. “Stepped-Frequency Continuous-Wave Radar With Self-Injection-Locking Technology for Monitoring Multiple Human Vital Signs”. In: *IEEE Transactions on Microwave Theory and Techniques* 67.12 (2019), pp. 5396–5405. DOI: [10.1109/TMTT.2019.2933199](https://doi.org/10.1109/TMTT.2019.2933199).
- [35] Ingo Walterscheid, Oliver Biallawons, and Patrick Berens. “Contactless Respiration and Heartbeat Monitoring of Multiple People Using a 2-D Imaging Radar”. In: *2019 41st Annual International Conference of the IEEE Engineering in Medicine and Biology Society (EMBC)*. 2019, pp. 3720–3725. DOI: [10.1109/EMBC.2019.8856974](https://doi.org/10.1109/EMBC.2019.8856974).
- [36] Junjun Xiong et al. “Multitarget Respiration Detection With Adaptive Digital Beamforming Technique Based on SIMO Radar”. In: *IEEE Transactions on Microwave Theory and Techniques* 68.11 (2020), pp. 4814–4824. DOI: [10.1109/TMTT.2020.3020082](https://doi.org/10.1109/TMTT.2020.3020082).
- [37] Chuanwei Ding et al. “Noncontact multiple targets vital sign detection based on VMD algorithm”. In: *2017 IEEE Radar Conference (RadarConf)*. 2017, pp. 0727–0730. DOI: [10.1109/RADAR.2017.7944298](https://doi.org/10.1109/RADAR.2017.7944298).
- [38] Jiaming Yan et al. “Through-Wall Multiple Targets Vital Signs Tracking Based on VMD Algorithm”. In: *Sensors* 16.8 (2016). ISSN: 1424-8220. DOI: [10.3390/s16081293](https://doi.org/10.3390/s16081293). URL: <https://www.mdpi.com/1424-8220/16/8/1293>.
- [39] Li Zhang et al. *Noncontact Multi-Target Respiration Sensing Using SIMO Radar with UBSS Method*. Dec. 2021. DOI: [10.1109/LMWC.2021.3138767](https://doi.org/10.1109/LMWC.2021.3138767).
- [40] Takato Koda et al. “Noncontact Respiratory Measurement for Multiple People at Arbitrary Locations Using Array Radar and Respiratory-Space Clustering”. In: *IEEE Access* 9 (2021), pp. 106895–106906.
- [41] Sohee Lim et al. “Detection and Localization of People Inside Vehicle Using Impulse Radio Ultra-Wideband Radar Sensor”. In: *IEEE Sensors Journal* 20.7 (2020), pp. 3892–3901. DOI: [10.1109/JSEN.2019.2961107](https://doi.org/10.1109/JSEN.2019.2961107).
- [42] Yu Teng, Chris Baker, and Karl Woodbridge. “Netted Radar Sensitivity and the Ambiguity Function”. In: *2006 CIE International Conference on Radar*. 2006, pp. 1–4. DOI: [10.1109/ICR.2006.343573](https://doi.org/10.1109/ICR.2006.343573).
- [43] Marco Mercuri et al. “Automatic radar-based 2-D localization exploiting vital signs signatures”. In: *Scientific Reports* 12.1 (May 2022), p. 7651. ISSN: 2045-2322. DOI: [10.1038/s41598-022-11671-1](https://doi.org/10.1038/s41598-022-11671-1). URL: <https://doi.org/10.1038/s41598-022-11671-1>.
- [44] Jakob Möderl, Franz Pernkopf, and Klaus Witrisal. “Car Occupancy Detection Using Ultra-Wideband Radar”. In: *2021 18th European Radar Conference (EuRAD)*. IEEE Xplore. 2021.
- [45] Chunmei Xu et al. “An improved CFAR algorithm for target detection”. In: *2017 International Symposium on Intelligent Signal Processing and Communication Systems (ISPACS)*. 2017, pp. 883–888. DOI: [10.1109/ISPACS.2017.8266600](https://doi.org/10.1109/ISPACS.2017.8266600).
- [46] Bitu Sobhani et al. “Multiple target detection and localization in UWB multistatic radars”. In: *2014 IEEE International Conference on Ultra-WideBand (ICUWB)*. 2014, pp. 135–140. DOI: [10.1109/ICUWB.2014.6958965](https://doi.org/10.1109/ICUWB.2014.6958965).

- [47] A. Samokhin, I. Ivashko, and A. Yarovoy. “Algorithm for multiple targets localization and data association in distributed radar networks”. In: *2014 15th International Radar Symposium (IRS)*. 2014, pp. 1–6. DOI: [10.1109/IRS.2014.6869183](https://doi.org/10.1109/IRS.2014.6869183).
- [48] Lucas Giroto de Oliveira et al. “Range Association and Fusion in a Network of Single-Channel Monostatic OFDM Radars”. In: *2020 IEEE MTT-S International Conference on Microwaves for Intelligent Mobility (ICMIM)*. 2020, pp. 1–4. DOI: [10.1109/ICMIM48759.2020.9299074](https://doi.org/10.1109/ICMIM48759.2020.9299074).
- [49] ChangKyeong Kim and Joon-Yong Lee. “ToA-based multi-target localization and respiration detection using UWB radars”. In: *EURASIP Journal on Wireless Communications and Networking* 2014 (2014), pp. 1–15.
- [50] Jianjun David Ni et al. “Design and Performance Evaluation on Ultra-Wideband Time-Of-Arrival 3D Tracking System”. In: 2012.
- [51] Martin Strohmeier, Ivan Martinovic, and Vincent Lenders. “A k-NN-Based Localization Approach for Crowdsourced Air Traffic Communication Networks”. In: *IEEE Transactions on Aerospace and Electronic Systems* 54.3 (2018), pp. 1519–1529. DOI: [10.1109/TAES.2018.2797760](https://doi.org/10.1109/TAES.2018.2797760).
- [52] Xuanyu Zhu. “Indoor Localization Based on Optimized KNN”. In: *Network and Communication Technologies* 5 (Dec. 2020), p. 34. DOI: [10.5539/nct.v5n2p34](https://doi.org/10.5539/nct.v5n2p34).
- [53] Khuong Nguyen and Zhiyuan Luo. “Conformal Prediction for Indoor Localisation with Fingerprinting Method”. In: vol. 382. Sept. 2012, pp. 214–223. ISBN: 978-3-642-33411-5. DOI: [10.1007/978-3-642-33412-2\\_22](https://doi.org/10.1007/978-3-642-33412-2_22).
- [54] NXP. *NCJ29D5: UWB IC for Automotive Applications*. <https://www.nxp.com/products/wireless/secure-ultra-wideband-uwband/trimension-ncj29d5-uwband-ic-for-automotive-applications:NCJ29D5>. Oct. 2021.
- [55] NXP. “NCJ29D5-Radar Evaluation Kit, Quick Start Guide”. In: (2021).
- [56] Matthias John and Max J. Ammann. “Antenna Optimization With a Computationally Efficient Multiobjective Evolutionary Algorithm”. In: *IEEE Transactions on Antennas and Propagation* 57.1 (2009), pp. 260–263. DOI: [10.1109/TAP.2008.2009775](https://doi.org/10.1109/TAP.2008.2009775).
- [57] NXP. “UG-SCA-6711, Multi Device Radar Quick Start Guide”. In: (2021).
- [58] Egor Zaikov and J. Sachs. “UWB Radar for Detection and Localization of Trapped People”. In: Aug. 2010. ISBN: 978-953-307-139-8. DOI: [10.5772/10004](https://doi.org/10.5772/10004).
- [59] Van Nguyen and Mary Weitnauer. “UWB impulse radar for vital signs sensing — A modeling framework for arbitrary periodic heart and lung motion”. In: Oct. 2015, pp. 1–4. DOI: [10.1109/BioCAS.2015.7348371](https://doi.org/10.1109/BioCAS.2015.7348371).
- [60] G.S.N. Raju P. Rajyalakshmi. “Characteristics of Radar Cross Section with Different Objects”. In: vol. 4. 2. 2011, pp. 205–216. DOI: [ISSN0974-2166](https://doi.org/10.1109/ISSN0974-2166).

- [61] Lanbo Liu et al. "Numerical simulation of UWB impulse radar vital sign detection at an earthquake disaster site". In: *Ad Hoc Networks* 13 (2014). (1)Special Issue : Wireless Technologies for Humanitarian Relief (2)Special Issue: Models And Algorithms For Wireless Mesh Networks, pp. 34–41. ISSN: 1570-8705. DOI: <https://doi.org/10.1016/j.adhoc.2012.08.006>. URL: <https://www.sciencedirect.com/science/article/pii/S1570870512001539>.

# APPENDICES

In Appendix [A](#), a block diagram of the designed ROS capturing system is presented.

In Appendix [B](#), the different multiplexing techniques for the separation of the anchors, namely CDMA, TDMA and FDMA is presented.

Finally, in Appendices [C](#) and [D](#), the detailed analysis of the results obtained with the processing of the experimental data in the Anechoic Chamber of TU Delft and NXP's concept car respectively is presented. The result analysis follows the performance metrics defined in Chapter [5](#).



# A

## ROS CAPTURING ARCHITECTURE BLOCK DIAGRAM

In Figure A.1, a block diagram of the designed ROS capturing system has been presented. In it, it can be seen how the different nodes are started independently, one for each anchor. The different configuration parameters are defined and finally a generalized trigger signal is sent to start the CIR transmission/reception of all 6 boards at the same time.

After the CIR radar data captured is published in a live stream in the defined ROS topics, this can be captured for a determined number of seconds, and stored in a .bag file. The .bag files can be converted to .csv format and imported into MATLAB for processing.

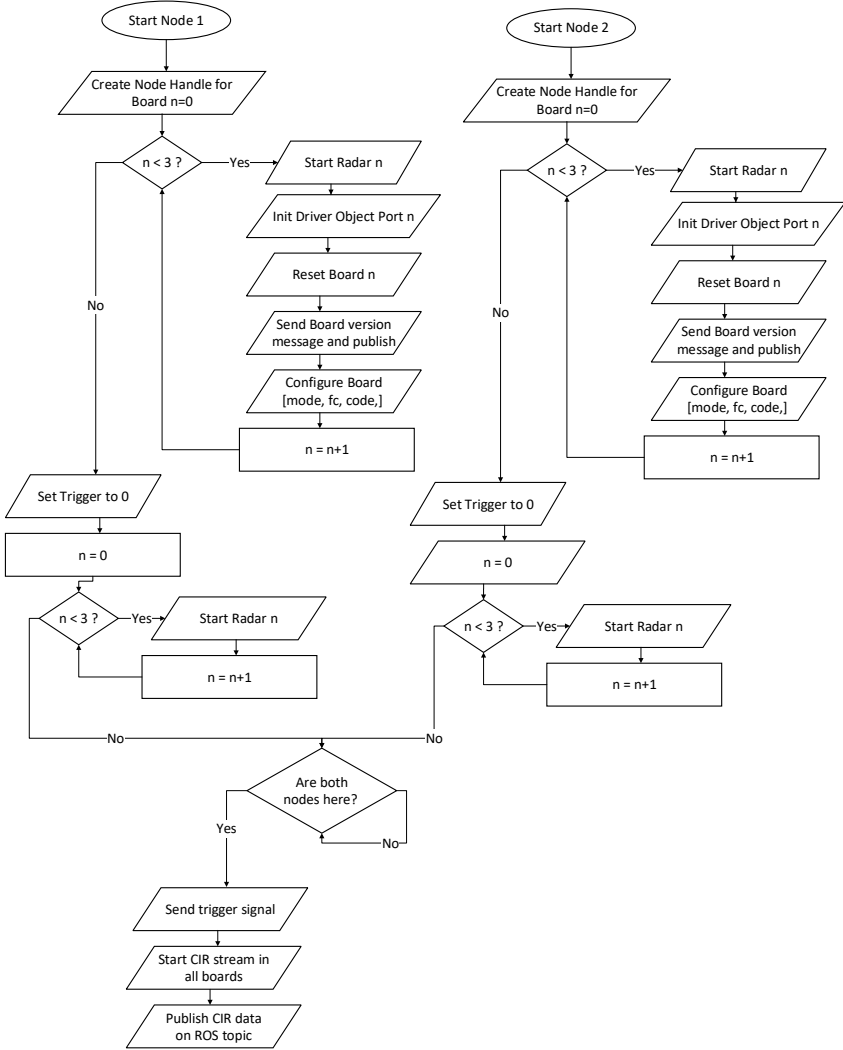


Figure A.1: Block diagram of multistatic UWB network capturing system

# B

## MULTIPLEXING TECHNIQUES INVESTIGATED FOR THE MULTISTATIC UWB NETWORK

### **B.1. CODE DIVISION MULTIPLE ACCESS IMPLEMENTATION**

One of the multiplexing options for the boards is to use Code Division Multiple Access (CDMA).

With CDMA, the transmitted pulses are encoded in orthogonal binary or ternary code sequences. By configuring the different transmitters to operate with a certain code, and its respective receives to operate with the same code, only the echos corresponding to the same encoding can be decoded by the receiver. Therefore, even if the Rx boards receive echos from various transmitters, they will only be able to decode those corresponding to the transmitters of their anchor, and the rest will not be detected.

In theory, this setup works and there is no code interference observed in the received CIR data. However, in the implementation of said setup, what could be attributed to code interference was observed in the CIR data .

Since all Rx boards can be placed anywhere w.r.t. the Tx boards, the receivers calculate their sensitivity by adjusting the threshold to the 1st echo they receive from the Tx boards. That is, if the boards are close together, as is the case in distributed monostatic operation, the LoS echo transmission is very short, of a few cm. Therefore, the sensitivity will be adjusted to a low value and further reflections will be visible with less energy. However, if the boards are further apart as in a bistatic radar, the LoS echo will be received later, and the boards will have higher sensitivity.

Because all boards have been clock-synchronized and operate at the same frequency, even if the received echos correspond to different codes, the Rx boards will automatically adjust their reception sensitivity to the first-received echo, indistinctly to the code.

Given the current setup in which the bistatic Rx boards are much closer to the Tx boards of the opposite anchor than to their own Tx boards, the reception sensitivity of the bistatic Rx boards was automatically tuned to the echos received with shorter LoS, that is the opposite transmitters. Since sensitivity had been tuned to shorter ranges, the CIR radar data was corrupted by the high-energy interference lines result of decoding the received pulses from different codes. The correct pulses were observed still and properly decoded, but with less energy and affected by the corruption.

An example of such received CIR data in a monostatic and bistatic radar boards can be observed in Figure B.1, where the 2 transmitters were multiplexed with the binary codes 0 and 5 as defined in the User Manual [55].

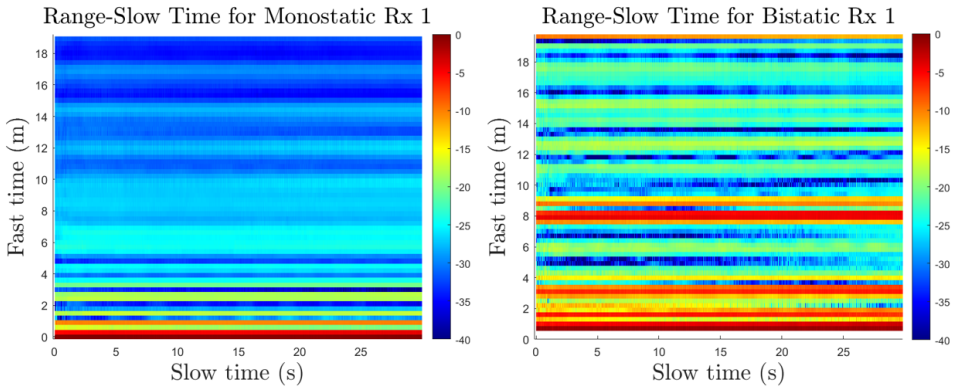


Figure B.1: (Left) : Monostatic CIR radar data. Tx board operating at Code 0 and Rx board operating at Code 0. | (Right) : Bistatic CIR radar data. Tx board operating at Code 0 and Rx board operating at Code 0. However, Tx board operating at Code 5 was closer, thus interference lines appear due to sensitivity adjustment to incorrect echo.

As was defined, the visible horizontal 'lines' in the bistatic Rx boards correspond to the code interference caused by the correlation of different code sequences, in this case, 0 and 5.

For future projects, thus, it can be seen how multiple distributed monostatic operation can be made possible using CDMA. Even bistatic operation is possible using CDMA, however, the closeness of the Rx boards to Tx corresponding to other anchors will be critical and thus will need studying before the project can be carried out.

Due to the constraints of this system, which requires boards to be distributed following the defined positions, CDMA has been discarded as a multiplexing technique for the bistatic receivers.

## B.2. TIME DIVISION MULTIPLE ACCESS IMPLEMENTATION

Another method to multiplex the transmitted information of the boards is to use Time Division Multiple Access (TDMA). This method uses the same frequency for the transmitters and also the same codes, but uses a fixed delay in between the pulses transmitted from different anchors.

The capturing tool implemented with ROS relies on the independent initialization of both anchors, each with its own configuration. When both anchors have been initialized and are ready to start transmitting/receiving, a generalized trigger signal is sent to all boards with no delay, thus all pulses are transmitted in the same time instant and the Rx boards start listening at the same time instant.

With TDMA, two different trigger signals would be sent. One to an anchor at time instant zero, and another to the second anchor, at a delayed time instant, smaller than the PRI of the boards. However, in order to implement this with ROS, the code would need to change its architecture to accommodate multi-threaded operation.

To get an idea of the possible functionality of a TDMA system, however, a few tests were made with the so-called unplanned TDMA. In this approach, both nodes were started independently as defined in A.1, but the trigger was not generalized in between both boards. Instead, two separate triggers were sent for each anchor, once each node has started all boards in that anchor. Therefore, given the fact that the start of the nodes was sequential, the triggers did not happen at the same time, but there was no control as to how much the delay introduced in between the systems would be.

The results for this unplanned TDMA were positive and resulted in no interference between the boards. However, the lack of control on the delay due to the need to re-arrange the capturing architecture means that this approach was not chosen as a multiplexing system for this thesis, but it has been checked that it can be a valid option for further projects involving Ranger4 boards.

## B.3. FREQUENCY DIVISION MULTIPLE ACCESS IMPLEMENTATION

In FDMA, the transmitter is assigned a specific frequency band in the electromagnetic spectrum, and the receivers in the same anchor will be listening to that particular frequency band as well. The bandwidth of the transmitted pulses of the Ranger4 boards is of 500MHz. Therefore, the different frequency bands allocated should present a minimum value equivalent to the bandwidth.

As seen in the Ranger 4 User Manual[55], different center frequencies can be allocated to a Tx or Rx board. Therefore, it is decided that one anchor will operate at 6.5 GHz and the other will operate at 7.5 GHz to keep a guard band of 500MHz between them.

In Figures , the received radar data is presented for a breathing measurement captured using the defined multiplexing method.

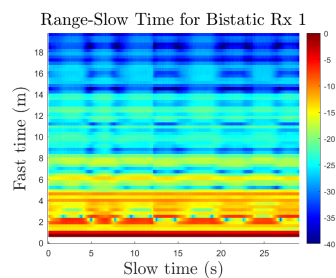
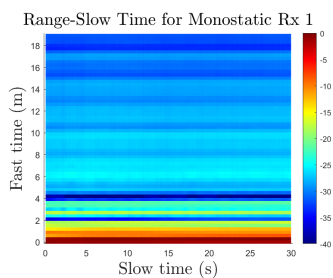


Figure B.2: Range-Slow Time Monostatic Rx 1 measure-Figure B.3: Range-Slow Time Bistatic Rx 1 measurement

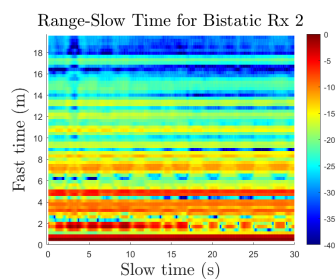
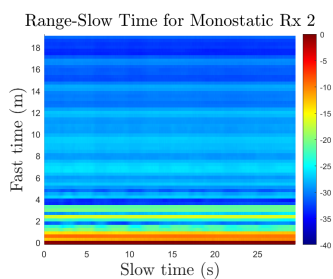


Figure B.4: Range-Slow Time Monostatic Rx 2 measure-Figure B.5: Range-Slow Time Bistatic Rx 2 measurement

As can be seen, there is no interference in the boards. Therefore, this is chosen as the multiplexing method for the UWB multistatic network designed.

# C

## MEASUREMENT PROCESSING RESULTS OF ANECHOIC CHAMBER

In the following Table C.1, the analysis of the results for a few of the measurements taken in the Anechoic Chamber with different subjects is presented.

The results have been analyzed in blocks. Firstly, the number of human detections and number of false alarms are detailed for every radar, together with the ranging error of the detected humans. Secondly, the final number of associated targets and their RMSE localization error is also presented.

For simplicity purposes, Rx boards are labeled 1-4 in the following order: Monostatic Rx 1, Bistatic Rx 1, Monostatic Rx 2, Bistatic Rx 2.

It should be noted that some measurements in the batch are not present because the capturing system failed and the received CIR data was not fit to be processed.

This fact reinforces the need to generate results and conclusions based on a simulated scenario.

Meas. num.	People	Pfa	Pfa	Det	Det	Det	Det	Error range	Error range	Error range	Error range	FA	FA	FA	FA	FA	Final n. targets	N miss	N ghost	RMSE localization error (cm)
3	B	0.021	0.006	1	1	1	1	0.5	23	7.7	22	0	0	2	1	2	0	0	1	23
4	A	0.015	0.011	1	1	0	1	6	22	-	15	0	0	1	0	1	0	0	0	15
5	A	0.015	0.011	1	1	1	1	2.4	27	12	12	2	1	2	1	2	0	0	0	6.7
7	B	0.015	0.011	0	0	1	1	-	-	7	16	2	1	1	1	1	1	1	1	89
8	AB	0.018	0.012	1	2	1	2	[6, -]	[7, 5]	[2.2, -]	[7, -]	3	1	1	2	2	1	0	0	[17, -]
9	AB	0.018	0.022	1	1	2	1	[-, 5]	[7, -]	[17, -]	[7, -]	1	0	1	0	2	1	1	1	[13, -]
10	AB	0.018	0.022	1	2	2	2	[-, 24]	[0.7, 15]	[17, 7]	[7, 28]	0	1	1	1	2	1	1	1	[9, 81]
11	AB	0.022	0.023	2	1	2	2	[24, 16]	[-, 3]	[13, 22]	[7, 1.2]	0	0	0	1	1	1	0	0	[-, 86]
12	AB	0.022	0.025	1	2	2	1	[-, 24]	[7.4, 0.3]	[2.5, 7.6]	[1.9, -]	0	1	1	0	2	1	1	1	[9.7, 87]
13	-	0.022	0.025	0	0	0	0	-	-	-	-	0	0	0	0	0	0	0	0	-

Table C.1: Evaluation of the results performed in the anechoic chamber of TU Delft using the proposed processing pipeline. The people column refers to the positions of the targets placed in a the environment following the coordinates defined in Table 5.2. The values for the parameter 2D-CFAR  $P_{fa}$  are noted. The evaluation metrics defined for the 2 processing blocks are evaluated. For detection, the number of detected humans in every measurement is noted, together with the number of false alarms and the range error for those targets detected. For association, the final number of targets located is written, together with the number of missed targets, ghost targets and localization RMSE for those targets which can be localized in the environment. The threshold for the Probability of Target has been set at 75%.

# D

## MEASUREMENT PROCESSING RESULTS OF IN-VEHICLE EXPERIMENTS

In the following Table [D.1](#), the analysis of the results for a few of the measurements taken in NXP's test car in the High Tech campus with different subjects is presented. The results have been analyzed in blocks. Firstly, the number of human detections and number of false alarms are detailed for every radar, together with the ranging error of the detected humans. Secondly, the final number of associated targets and their RMSE localization error is also presented.

For simplicity purposes, Rx boards are labeled 1-4 in the following order: Monostatic Rx 1, Bistatic Rx 1, Monostatic Rx 2, Bistatic Rx 2.

It should be noted that some measurements in the batch are not present because the capturing system failed and the received CIR data was not fit to be processed.

This fact reinforces the need to generate results and conclusions based on a simulated scenario.

Meas. num.	People	Pfa	Pfa	Det	Det	Det	Det	Error range	Error range	Error range	Error range	FA	FA	FA	FA	FA	Final n. targets	N miss	N ghost	RMSE localization error (cm)
27	A	0.004	0.003	0	1	1	1	-	6.8	8	11	1	0	2	1	2	0	0	1	16
28	A	0.007	0.003	0	1	1	1	-	23	7.7	9	1	0	1	0	1	0	0	0	60
30	A	0.006	0.004	1	1	1	1	18	23	24	23	1	0	1	1	1	0	0	0	29
31	B	0.008	0.006	1	1	0	0	39	32	-	-	1	0	2	1	1	0	0	0	38
34	B	0.007	0.010	0	1	1	1	-	28	6	0.3	1	0	3	2	2	1	1	2	-
35	B	0.010	0.018	0	1	0	1	-	28	-	3	1	0	3	2	1	0	0	0	29
40	AB	0.015	0.019	2	2	1	2	[25, 18]	[1, 22]	[5, -]	[11, 18]	2	2	2	1	4	1	3	[9, 52]	
41	AB	0.005	0.012	1	0	2	0	[-, -]	[-, -]	[8, 24]	[-, -]	1	2	0	1	1	2	1	[-, -]	
44	AB	0.005	0.009	1	1	2	1	[-, 19]	[-, 16]	[29, 54]	[-, 19]	1	1	1	1	3	0	1	[12, 16]	
47	AB	0.005	0.008	1	2	2	2	[18, -]	[9, 21]	[13, 6]	[32, 4]	2	0	1	0	2	0	0	[11, 44]	

Table D.1: Evaluation of the results performed in NXP's test car using the proposed processing pipeline. The people column refers to the positions of the targets placed in a the environment following the coordinates defined in Table 5.8. The values for the parameter 2D-CFAR  $P_{fa}$  are noted. The evaluation metrics defined for the 2 processing blocks are evaluated. For detection, the number of detected humans in every measurement is noted, together with the number of false alarms and the range error for those targets detected. For association, the final number of targets located is written, together with the number of missed targets, ghost targets and localization RMSE for those targets which can be localized in the environment. The threshold for the probability of target has been set at 75%